

30610



National Library of Canada

Bibliothèque nationale du Canada

CANADIAN THESES ON MICROFICHE

THÈSES CANADIENNES SUR MICROFICHE

NAME OF AUTHOR/NOM DE L'AUTEUR ALLAN CLIFFORD BATES

TITLE OF THESIS/TITRE DE LA THÈSE SLOWNESS - AZIMUTH MEASUREMENTS and P WAVE 'VELOCITY' DISTRIBUTIONS

UNIVERSITY/UNIVERSITÉ UNIVERSITY of ALBERTA

DEGREE FOR WHICH THESIS WAS PRESENTED/ GRADE POUR LEQUEL CETTE THÈSE FUT PRÉSENTÉE PH.D.

YEAR THIS DEGREE CONFERRED/ANNÉE D'OBTENTION DE CE GRADE 1976

NAME OF SUPERVISOR/NOM DU DIRECTEUR DE THÈSE DR. E. R. KANASEWICH

Permission is hereby granted to the NATIONAL LIBRARY OF CANADA to microfilm this thesis and to lend or sell copies of the film.

L'autorisation est, par la présente, accordée à la BIBLIOTHÈQUE NATIONALE DU CANADA de microfilmer cette thèse et de prêter ou de vendre des exemplaires du film.

The author reserves other publication rights, and neither the thesis nor extensive extracts from it may be printed or otherwise reproduced without the author's written permission.

L'auteur se réserve les autres droits de publication; ni la thèse ni de longs extraits de celle-ci ne doivent être imprimés ou autrement reproduits sans l'autorisation écrite de l'auteur.

DATED/DATE OCT. 24 / 1976 SIGNED/SIGNÉ Allan Bates

PERMANENT ADDRESS/RÉSIDENCE FIXE 405 11 AV. N.W.  
CALGARY  
ALBERTA

INFORMATION TO USERS

THIS DISSERTATION HAS BEEN  
MICROFILMED EXACTLY AS RECEIVED.

This copy was produced from a microfiche copy of the original document. The quality of the copy is heavily dependent upon the quality of the original thesis submitted for microfilming. Every effort has been made to ensure the highest quality of reproduction possible.

PLEASE NOTE: Some pages may have indistinct print. Filmed as received.

Canadian Theses Division  
Cataloguing Branch  
National Library of Canada  
Ottawa, Canada K1A 0N4

AVIS AUX USAGERS

LA THESE A ETE MICROFILMEE  
TELLE QUE NOUS L'AVONS RECUE

Cette copie a été faite à partir d'une microfiche du document original. La qualité de la copie dépend grandement de la qualité de la thèse soumise pour le microfilmage. Nous avons tout fait pour assurer une qualité supérieure de reproduction.

NOTA BENE: La qualité d'impression de certaines pages peut laisser à désirer. Microfilmée telle que nous l'avons reçue.

Division des thèses canadiennes  
Direction du catalogage  
Bibliothèque nationale du Canada  
Ottawa, Canada K1A 0N4

THE UNIVERSITY OF ALBERTA

SLOWNESS-AZIMUTH MEASUREMENTS AND P WAVE  
VELOCITY DISTRIBUTIONS

by



ALLAN CLIFFORD BATES

A THESIS

SUBMITTED TO THE FACULTY OF GRADUATE STUDIES AND RESEARCH  
IN PARTIAL FULFILLMENT OF THE REQUIREMENTS FOR THE DEGREE  
OF DOCTOR OF PHILOSOPHY

DEPARTMENT OF PHYSICS

EDMONTON, ALBERTA

FALL, 1976

THE UNIVERSITY OF ALBERTA

FACULTY OF GRADUATE STUDIES AND RESEARCH

The undersigned certify that they have read, and recommend to the Faculty of Graduate Studies and Research, for acceptance, a thesis entitled SLOWNESS-AZIMUTH MEASUREMENTS AND P WAVE VELOCITY DISTRIBUTIONS submitted by Allan Clifford Bates in partial fulfillment of the requirements for the degree of Doctor of Philosophy.

...*E. R. Kossow*...  
Supervisor

...*M. R. ...*...

...*...*...

...*D. J. Gough*...

...*...*...

...*Lane Johnson*...  
External Examiner

Date: 9/24/76

DEDICATION

This thesis is dedicated to my father and mother,  
Matthew and Pearl Bates, my wife, Joanne, and my son,  
Matthew.

## ABSTRACT

A study of slowness and azimuth measurements of seismic P wave phases, errors associated with these measurements, and implications as to the nature of the P wave velocity distribution within the earth is presented.

Errors in the arrival times of plane waves at seismic arrays result in errors in slowness and azimuth. It has been found that the stability of the inversion process is related to the condition number of the matrix inversion and that symmetric arrays yield the most stable estimates of slowness and azimuth in the presence of travel-time errors. If travel-time errors are given in the root mean square error sense then the least square error inversion results in maximum and most likely error ellipses in the slowness-azimuth error plane for any array. The error analysis is not restricted to cases for which travel-time errors are specified in the root mean square error manner. In particular if travel-time errors are bounded then errors in the slowness-azimuth error plane are bounded by multisided figures which reflect the array configuration. Several array configurations are used to illustrate that the most effective procedure for error improvement is to add additional stations along the periphery of an existing array instead of in the interior.

Slowness and azimuth observations of teleseismic P phases recorded by the 1974 Variable Aperture Seismic Array (VASA) indicate departures of the P wave velocity distribution within the earth from a spherically symmetrical model for which P wave travel times are in accordance with the Jeffreys-Bullen Seismological Tables. If lateral inhomogeneities within the crust and upper mantle under VASA are not severe, and preliminary indications are that this is the case, then the observations indicate the existence of anomalously high velocity-depth gradients at a depth of about 1900 km, velocity inhomogeneities near the core-mantle boundary under some areas of the Pacific Ocean, and anomalous conditions predominated by lateral velocity gradients between depths of about 1900 and 2600 km under a region close to the Caribbean. Also the slowness observations are consistent with an 'average' spherically symmetrical lower mantle for which the P wave velocity is slightly greater than the Jeffreys-Bullen designation.

The Tau method of seismic travel-time inversion is investigated. A method of estimating extremal values of the function  $\tau(p) = \frac{T(p)}{2} - p \frac{X(p)}{2}$  where  $p$  is the ray parameter,  $T$  the travel time, and  $X$  the epicentral distance is presented. For each branch of the travel-time curve,  $T$  observations are fitted to a family of second order polynomials in  $X$ . The families of curves are

then mapped into the  $\tau(p)$  plane. The Tau method is illustrated by inverting  $T(X)$  data recorded along the 'Yukon' line during Project Early Rise. A comparison of  $\tau(p)$  results from several other studies in North America reflects differences in crustal and upper mantle structure. Also the resolving power, as a function of separation of observation points of the Tau method is examined by inverting  $\tau(p)$  envelopes calculated from exact velocity-depth functions.



## ACKNOWLEDGEMENTS

This work would not have been accomplished without the guidance and encouragement I received from my supervisor, Dr. E.R. Kanasewich. I am grateful to him.

I would like to thank Mr. C. McCloughan since on many occasions his experience with computer software matters was of benefit to me.

I was fortunate to have had the opportunity of studying some aspects of numerical matrix analysis with Dr. S. Cabay while I received a Graduate Service Assistantship for one term. I wish to thank Dr. Cabay for sharing his knowledge and time with me.

I wish to express my gratitude to Dr. D.H. Hall, University of Manitoba, who originally interested me in Geophysics.

I wish to express my appreciation to the National Research Council of Canada and the University of Alberta since I received an N.R.C. Postgraduate Scholarship and later a U. of A. Dissertation Fellowship.

## TABLE OF CONTENTS

|   | <u>Page</u> |
|---|-------------|
| CHAPTER 1: SEISMIC ARRAY DESIGN AND BACKWARD ERROR ANALYSIS OF WAVE SLOWNESS AND AZIMUTH            | 1           |
| Introduction  | 1           |
| The Importance of Array Measurements of Slowness and Azimuth  | 2           |
| Backward Error Analysis   | 4           |
| Error Bounds for Arbitrary Array Configurations and Arbitrary Specifications of Arrival-Time Errors | 13          |
| Array Error Numbers and Average Error   | 16          |
| Examples  | 25          |
| Conclusions   | 39          |
| CHAPTER 2: TELESEISMIC SLOWNESS AND AZIMUTH MEASUREMENTS: THE 1974 VARIABLE APERTURE SEISMIC ARRAY  | 42          |
| Introduction  | 42          |
| The 1974 Variable Aperture Seismic Array  | 44          |
| Velocity Spectral Analysis and the Covespa Process  | 52          |
| The $\Delta(p)$ , Slowness-Azimuth, and $\tau(p)$ Planes; Results from 1974 VASA                    | 67          |
| The $\Delta(p)$ Plane   | 70          |
| The Slowness-Azimuth Plane  | 83          |
| The $\tau(p)$ Plane   | 104         |
| Conclusions   | 113         |

|  | <u>Page</u> |
|--|-------------|
| CHAPTER 3: INVERSION OF TRAVEL-TIME DATA<br>USING THE TAU METHOD | 116         |
| Introduction   | 116         |
| Mapping $\tau(p)$ Limits into Velocity-<br>Depth Limits          | 118         |
| Resolving Power as a Function of<br>Station Spacing              | 129         |
| Estimation of the Function $\tau(p)$<br>from Real Data           | 134         |
| Results from Project Early Rise                                  | 149         |
| Conclusions  | 171         |
| REFERENCES   | 173         |
| APPENDIX 1   | 185         |
| APPENDIX 2   | 187         |
| APPENDIX 3   | 189         |

## LIST OF TABLES

| <u>Table</u> |   | <u>Page</u> |
|--------------|---|-------------|
| 2.1          | 1974 VASA Station Locations             | 47          |
| 2.2          | Results from Major $\Lambda(p)$ Studies | 79          |

## LIST OF FIGURES

| <u>Figure</u> |   | <u>Page</u> |
|---------------|---|-------------|
| 1.1           | The Relationship Between Errors in Slowness and Azimuth       | 9           |
| 1.2           | L-Shaped Array Error Spaces                                   | 27          |
| 1.3           | Circular Array Error Spaces                                   | 29          |
| 1.4           | Double-Circular Array Error Spaces                            | 31          |
| 1.5           | Box Array Error Spaces  | 33          |
| 2.1           | 1974 VASA Location Map  | 45          |
| 2.2           | Reponse of the Recording System                               | 48          |
| 2.3           | Covespagram of Synthetic Events: Signal to Noise Ratio of 4:1 | 56          |
| 2.4           | Covespagram of Synthetic Events: Signal to Noise Ratio of 1:1 | 58          |
| 2.5           | Covespagram for Salta Province, Argentina Event               | 61          |
| 2.6           | Covespagram for Mongolia Event                                | 63          |
| 2.7           | Covespagram for Panama-Columbia Event                         | 65          |
| 2.8           | 1974 VASA2 Event Locations                                    | 68          |
| 2.9           | 1974 VASA $\Delta(p)$ Observations                            | 76          |
| 2.10          | Slowness-Azimuth Array Diagram for VASA1                      | 84          |
| 2.11          | Slowness-Azimuth Array Diagram for VASA2                      | 86          |
| 2.12          | Size of Slowness-Azimuth Departures                           | 93          |
| 2.13          | VASA2 Ray Midpoints   | 102         |
| 2.14          | 1974 VASA $\tau(p)$ Observations; J-B Empirical Curve         | 106         |

| <u>Figure</u> |  | <u>Page</u> |
|---------------|--|-------------|
| 2.15          | 1974 VASA $\tau(p)$ Observations: Hales<br>Empirical Curve     | 110         |
| 3.1           | Velocity-Depth Bounds from Tau<br>Inversion-Hypothetical Model | 132         |
| 3.2           | The Function $\tau(X,p)$ -Hypothetical<br>model                | 135         |
| 3.3           | Travel-Time Curve for First Branch<br>from Yukon Line          | 138         |
| 3.4           | The Function $\tau(X,p)$ for First Branch<br>from Yukon Line   | 140         |
| 3.5           | Typical Error Ellipse  | 146         |
| 3.6           | Travel-Times and $\tau(p)$ Envelope for<br>Yukon Line          | 150         |
| 3.7           | Velocity-Depth Bounds for Yukon Line                           | 154         |
| 3.8           | $\tau(p)$ Points from Other Early Rise Lines                   | 162         |
| 3.9           | $\tau(p)$ from North American Studies                          | 165         |

## CHAPTER 1

# SEISMIC ARRAY DESIGN AND BACKWARD ERROR ANALYSIS OF WAVE SLOWNESS AND AZIMUTH

### Introduction

Array measurements of the slowness and azimuth of seismic body wave phases have been used for the purpose of delineating earth velocity structure by many investigators within the last decade. In this study investigations of errors associated with such measurements and the relationship between the P wave velocity of the earth and slowness-azimuth observations are presented. In Chapter 1 errors in slowness and azimuth as determined by two dimensional seismic arrays are studied using powerful results from matrix iterative analysis. The 1974 Variable Aperture Seismic Array (VASA) slowness and azimuth observations and the implications regarding the nature of the P wave velocity distribution within the earth associated with them are discussed in Chapter 2. A study of the Tau method of travel-time inversion, which is applicable to spherically symmetrical velocity functions, is given in Chapter 3. A method for the determination of errors in the function  $\tau(p)$  is presented. The Tau method is illustrated by inverting travel-time data recorded by the University of Alberta on Project Early Rise. In all

chapters the contributions of past investigations will be cited within the text. It is felt that for this study such a procedure is more appropriate than a historical review.

The Importance of Array Measurements of Slowness and Azimuth

The two-dimensional seismic array is a major tool in the investigation of the velocity and structure of the earth's crust and mantle. In most experiments the elastic waves are observed in the far field at places where the radius of curvature of the wavefront is very much greater than the array size and the structural inhomogeneities to be studied. It is possible to assume that each phase traverses the array in the form of a plane wave with a given azimuthal orientation and slowness. If the array is situated on a Cartesian coordinate system, then the equation for the arrival time,  $t(x,y)$ , of a given phase at location  $(x,y)$  is,

$$t(x,y) = t_0 + p_x x + p_y y . \tag{1.1}$$

In (1.1), the kinematic properties of the plane wave are specified by  $t_0$ , the arrival time at the origin  $(x,y) = (0,0)$ , and  $p_x$  and  $p_y$ , the x and y components of slowness.

Small seismic arrays are used to advantage in exploration geophysics in both the reflection and



refraction method to determine mean and interval velocities and to discriminate against noise generated by multiple reflections. Medium and large aperture seismic arrays have found wide use in the investigation of possible departures in upper and lower mantle velocities from standard models. A large change in velocity gradient may correspond to a small change in velocity and have very little effect on the observed travel time. Thus a direct measurement of the vector ray parameter  $p$ , using a seismic array may delineate important anomalies. Birtill and Whiteway (1965) have discussed the frequency-wavenumber response characteristics of arrays in general. Otsuka (1966) gives the expressions for slowness and azimuth variance for given variance of travel-time error. The following analysis is a thorough treatment of the errors to be expected in determining the velocity and azimuth when a plane wave propagates across an array of detectors. The analysis is necessary in order to determine the array size and shape and the sampling time required for a particular significance level. The results may be used to determine which observations of anomalies in velocity or azimuth are significant and may be interpreted as inhomogeneities within the earth.

### Backward Error Analysis

With data from a seismic array, the solution for the vector ray parameter,  $\underline{p}$ , is given by

$$\underline{p}' = A^{-1} \underline{T} \quad (1.2)$$

where  $A$  is the 'array' matrix which depends upon the coordinates of the stations comprising the array and  $\underline{T}$  is the 'observation' vector which depends upon the observed arrival times and the station coordinates. It is common practice to determine the best fitting plane wave, in the least squares sense. For  $N$  stations situated at  $(X_i, Y_i)$ ,  $i = 1, N$  and reporting arrival times  $t_i$ ,  $i = 1, N$  and a best fit plane wave described by equation (1.1) we have that the root mean square error,  $E$ , in arrival time is,

$$E = \left( \sum_{i=1}^N \left\{ \frac{(t_i - t_0 - p_x X_i - p_y Y_i)^2}{N} \right\} \right)^{1/2}$$

Taking  $\partial E / \partial p_x = \partial E / \partial p_y = \partial E / \partial t_0 = 0$  we obtain

$$\underline{p} = A^{-1} \underline{T}$$

$$\underline{p} = (p_x, p_y)^T$$

$$A = \begin{pmatrix} \sum X_i^2 - \frac{(\sum X_i)^2}{N} & \sum X_i Y_i - \frac{\sum X_i \sum Y_i}{N} \\ \sum X_i Y_i - \frac{\sum X_i \sum Y_i}{N} & \sum Y_i^2 - \frac{(\sum Y_i)^2}{N} \end{pmatrix} \quad (1.3)$$

$$\underline{T} = \left( \Sigma t_i X_i - \frac{\Sigma t_i \Sigma X_i}{N}, \Sigma t_i Y_i - \frac{\Sigma t_i \Sigma Y_i}{N} \right)^T$$

The study of the effects of perturbations of the elements of the matrix  $A$  and the vector  $\underline{T}$  upon the elements of vector  $\underline{p}$  is referred to in numerical matrix analysis as 'backward error analysis' (Wilkinson, 1965). Seismologically this type of analysis is extremely important since we would like to know firstly the size of the errors in  $\underline{p}$  and secondly how to make errors in  $\underline{p}$  as small as possible. In Appendix 1 some definitions, concepts, and results from the numerical analysis of linear algebraic systems are introduced (Forsythe and Moler, 1967). The results will be applied to the problem of measuring the vector ray parameter  $\underline{p}$ .

In equation (1.2) it is assumed that the elements of the vector  $\underline{T}$  and possibly the matrix  $A$  are scientific measurements. For inversion the desired quantity is the vector  $\underline{p}$ . Obviously small measurement errors in the entries of  $A$  and  $\underline{T}$  result in errors in the vector  $\underline{p}$ . If  $\delta \underline{T}$  and  $\delta A^{-1}$  represent the errors in  $\underline{T}$  and  $A^{-1}$  respectively, then we actually measure the quantity  $\underline{p} + \delta \underline{p}$ ,

$$\underline{p} + \delta \underline{p} = A^{-1} \underline{T} + A^{-1} \delta \underline{T} + \delta A^{-1} \underline{T} + \delta A^{-1} \delta \underline{T} . \quad (1.4)$$

Thus the error in  $\underline{p}$  is given by,

$$\delta \underline{p} = A^{-1} \delta \underline{T} + \delta A^{-1} (\underline{T} + \delta \underline{T}) . \quad (1.5)$$

It is desirable to design an array in such a way that the measured vector  $\underline{p}$  responds in a stable manner, deviating from the true  $\underline{p}$  only slightly, upon small perturbations in  $\underline{T}$  and  $A$ . In order to obtain such a system it is necessary to consider upper bounds of the 'size', in the vector norm sense (see Appendix 1), of  $\delta \underline{p}$ . If, as is usually the case in seismology, we suppose that there are errors in  $\underline{T}$  (due to errors in arrival time) but no errors in  $A$ , then for any vector norm,

$$\frac{||\delta \underline{p}||}{||\underline{p}||} \leq \kappa(A) \frac{||\delta \underline{T}||}{||\underline{T}||} \quad (1.6)$$

The 'condition number',  $\kappa(A)$ , of a square non-singular matrix  $A$  is obtained from  $\kappa(A) = ||A|| ||A^{-1}||$ . In the inequality  $\kappa(A)$  is calculated using the matrix norm (see Appendix 1), which is induced by the vector norm used. Similarly if there are errors in both  $A$  and  $\underline{T}$  then for any vector norm (see Franklin (1968), page 177)

$$\frac{||\delta \underline{p}||}{||\underline{p}||} \leq \frac{\kappa(A)}{1 - \kappa(A) \frac{||\delta A||}{||A||}} \left( \frac{||\delta A||}{||A||} + \frac{||\delta \underline{T}||}{||\underline{T}||} \right) \quad (1.7)$$

The inequalities (1.6) and (1.7) show explicitly the importance of the condition number  $\kappa(A)$ . An optimal system results for a given norm when  $\kappa(A)$  is as small as possible with respect to that norm; the choice of a particular norm depends upon the interpretation and

scientific application of the vector  $\underline{p}$ .

Array Design

The results (1.6) and (1.7) can now be applied to the problem of the determination of slowness and azimuth of plane waves. In the slowness-azimuth equation (1.2), the elements of the system matrix, A, depend only upon the x and y coordinates of the stations. Thus the condition number,  $\kappa(A)$ , depends purely upon the locations of the stations. The obvious implication of this fact is that we can ensure a stable system, that is minimize  $\kappa(A)$ , by a corresponding correct choice of the geometrical pattern formed by the stations. We wish to minimize errors in the slowness,  $\underline{p}$ , and the azimuth,  $\theta$ . The slowness is simply the Euclidean vector norm,  $||\underline{p}||$ , of  $\underline{p}$ . The slowness error is given by  $||\underline{p} + \delta\underline{p}|| - ||\underline{p}||$ . Thus the maximum absolute value of the slowness error is  $||\delta\underline{p}||$ . From (1.6) or (1.7) the maximum slowness error is minimized when  $\kappa(A)$  calculated using the spectral norm is as small as possible. Also, the choice of spectral norm is indeed wise for the purpose of designing an array which minimizes errors in azimuth. This is true since if  $\delta p_{\max}$  is the maximum possible slowness error and  $|\delta\theta|_{\max}$  is the absolute value of the maximum azimuthal error, then

$$\begin{aligned}
 |\delta\theta|_{\max} &= \arctan(\delta p_{\max}/p), & \delta p_{\max} \leq p \\
 &= \pi, & \delta p_{\max} > p.
 \end{aligned}
 \tag{1.8}$$

Equation (1.8) is important for two reasons. Firstly it shows that a given array is an effective slowness discriminator if and only if it is an effective azimuth discriminator. Secondly equation (1.8) permits a calculation of maximum errors in azimuth for given maximum error  $\delta p$  for any seismic array. At this point it is worth noting that slowness and azimuth errors,  $\delta p$  and  $\delta\theta$ , cannot achieve their maximum values simultaneously. From figure 1.1 it is not difficult to see that

$$\delta\theta = \arctan \left\{ \frac{(\delta p_{\max}^2 - \delta p^2)^{1/2}}{p \pm \delta p} \right\}.
 \tag{1.9}$$

From (1.9) we see that  $\delta\theta$  attains its maximum value only when  $\delta p = 0$  and that  $\delta p$  attains its maximum value only when  $\delta\theta = 0$ .

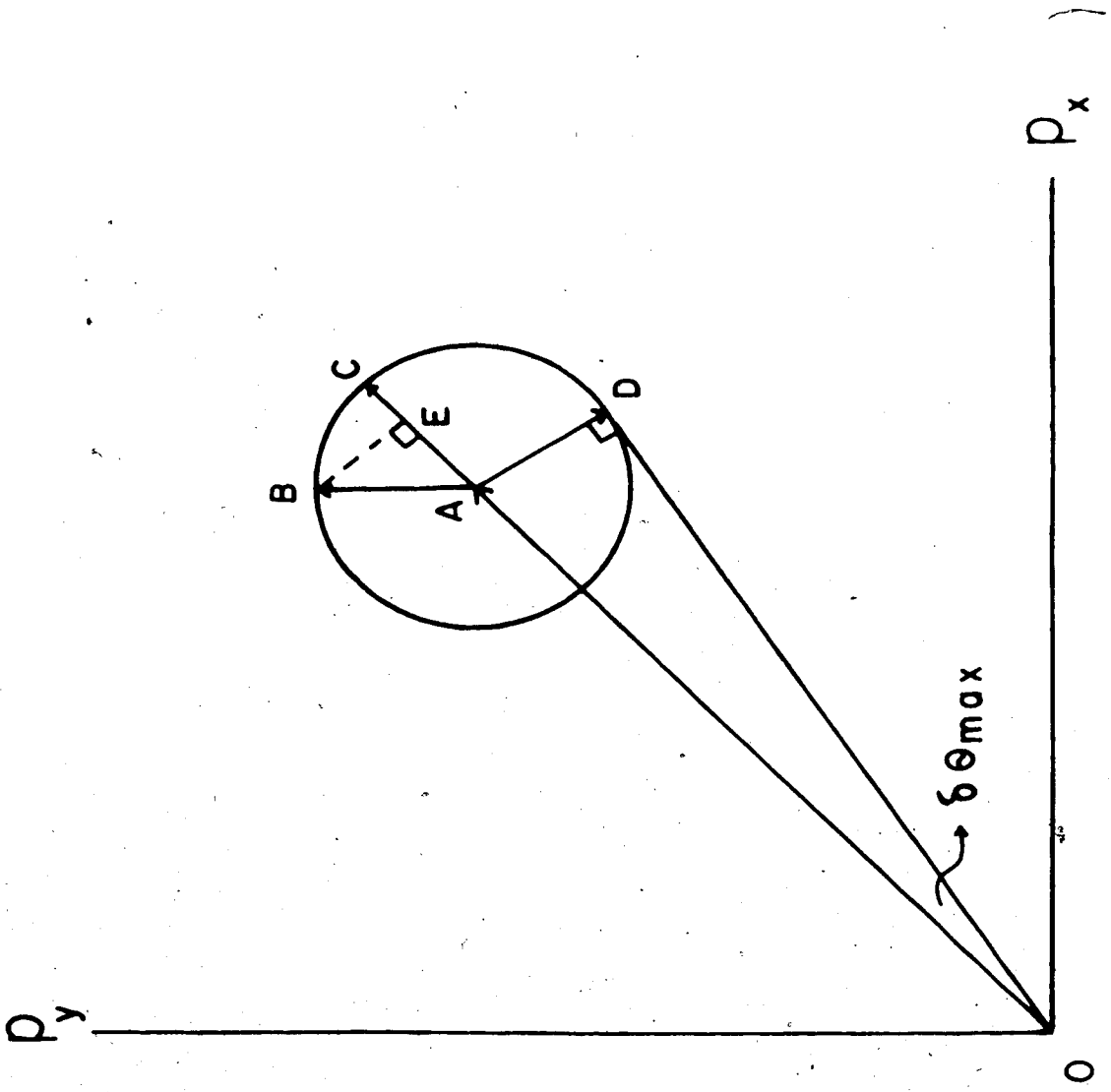
Now the inverse problem given by (1.2) will be the most stable when  $\kappa(A) = 1$ , where  $A$  is given by (1.3). By constructing  $AA^T$  and using the results of Appendix 1 it is possible to show that  $\kappa(A) = 1$  if and only if the following conditions are satisfied;

$$\begin{aligned}
 \sum X_i^2 &= \sum Y_i^2 \\
 \sum X_i Y_i &= 0 \\
 \sum X_i &= 0
 \end{aligned}
 \tag{1.10}$$

Figure 1.1

The relationship between errors in slowness and azimuth is shown here. The vector defined by segment  $\overline{OA}$  is the true slowness vector. The radius of the error circle is  $\delta p_{\max}$ . Three error vectors defined by segments  $\overline{AD}$ ,  $\overline{AC}$ , and  $\overline{AB}$  are shown. Vector  $\overline{AD}$  produces the maximum azimuthal deviation  $\delta\theta_{\max}$  and segment  $\overline{AC}$  results in the maximum slowness deviation  $\delta p_{\max}$ . The error vector  $\overline{AB}$  contains both slowness and azimuth error components; with the length  $AE \approx \delta p$  the relationship between the errors is given by equation (1.9).

3





$$\sum Y_i = 0.$$

The general proof of the above relations is rather lengthy.

The conditions require that the array be constructed in a symmetric manner. It is instructive to consider the derivation and results when there are  $N=3$  stations. In this case the matrix  $A$  in equation (1.3) yields,

$$AA^T = \frac{1}{9} \begin{pmatrix} a & c \\ c & b \end{pmatrix}$$

where

$$\begin{aligned} a &= (2X_2^2 + 2X_3^2 - 2X_2X_3)^2 + (2X_3Y_3 - X_2Y_3)^2 \\ b &= (2X_3Y_3 - X_2Y_3)^2 + 4Y_3^4 \\ c &= (2X_3Y_3 - X_2Y_3)(2X_2^2 + 2X_3^2 + 2Y_3^2 - 2X_2X_3). \end{aligned}$$

The eigenvalues  $\tau_{1,2}$  of  $AA^T$  are the roots of the characteristic equation  $\det(AA^T - \tau_{1,2}I) = 0$ . Thus they satisfy  $81\tau_{1,2}^2 - 9\tau_{1,2}(a+b) + (ab-c^2) = 0$ . For  $\kappa(A)$  to be unity, the eigenvalues  $\tau_{1,2}$  must have the same magnitude, and hence  $\kappa(A) = 1$ , if and only if  $c^2 = -(a-b)^2/4$  which implies  $a = b$  and  $c = 0$ . From the above expressions the condition  $c = 0$  requires that  $X_3 = X_2/2$ . This fact combined with the condition that  $a = b$  yields  $Y_3 = \pm\sqrt{3} X_3$ .

Notice now that the resultant array consists of three stations located at the vertices of an equilateral triangle. The array locations satisfy equations (1.10) and this is the only three station geometry for which  $\kappa(A) = 1$ .

In general arrays which satisfy (1.10) are symmetrical with respect to the (X,Y) axes. An example of an array which possesses this high degree of symmetry is LASA in Montana. Note further that each station of LASA is composed of several sensors with the 'sub-arrays' formed by them satisfying (1.10). Thus the entire array and each sub-array are capable of reporting stable large or small aperture array estimates respectively of slowness and azimuth.

It is worth commenting on the effect of array size. Suppose we have an array with system matrix  $A_1$  which satisfies (1.10). If we increase the size of this array by a magnification factor  $m > 1$  to form a new array with system matrix  $A_2$ , then  $\kappa(A_2) = 1$ . Errors for the second array,  $A_2$ , however, will be smaller since  $\|A\|$  and  $\|T\|$  will be larger.

For arbitrary  $N > 3$ , equations (1.10) do not dictate a unique geometrical pattern of stations; nevertheless from this discussion it is clear that it is advantageous to select a geometry which does satisfy the above requirements.

Error Bounds for Arbitrary Array Configurations and  
Arbitrary Specifications of Arrival-Time Errors

It is important to realize that the upper bounds given by (1.6) and (1.7) in general depend upon the azimuth of the incoming plane wave for a given slowness. Let us assume that there are no errors in the coordinates of the stations and focus our attention upon the upper bound (1.6). Also suppose for simplicity that we have a 3 station determination of  $\underline{p}$ . With the array coordinates given by  $(X_i, Y_i)$ ,  $i = 1, 3$  (and for convenience  $X_1 = Y_1 = 0$ ), the upper bound (1.6) can be written as follows;

$$\|\delta \underline{p}\| = \frac{v(A) \|\delta T\|}{f(X_i, Y_i, \theta_0)} \quad (1.11)$$

where

$$\theta_0 = \theta - \pi$$

and

$$f(X_i, Y_i, \theta) = \left\{ \cos^2 \theta_0 \left[ \frac{4}{9} (X_2^2 + X_3^2 - X_2 X_3)^2 + \frac{1}{9} (2X_2 Y_2 + 2X_3 Y_3 - X_2 Y_3 - X_3 Y_2)^2 \right] + \sin^2 \theta_0 \left[ \frac{4}{9} (Y_2^2 + Y_3^2 - Y_2 Y_3)^2 + \frac{1}{9} (2X_2 Y_2 + 2X_3 Y_3 - X_2 Y_3 - X_3 Y_2)^2 \right] + \sin \theta_0 \cos \theta_0 \left[ \frac{2}{9} (X_2^2 + X_3^2 - X_2 X_3 + Y_2^2 + Y_3^2 - Y_2 Y_3) \times (2X_2 Y_2 + 2X_3 Y_3 - X_2 Y_3 - X_3 Y_2) \right] \right\}.$$

The expression (1.11) shows explicitly that the upper bound given by (1.6) depends upon the azimuth for an arbitrary array. Nevertheless for appropriate choices of the directions of the vectors  $\underline{T}$  and  $\delta\underline{T}$  there can be equality in (1.6). Thus for arbitrary vectors  $\underline{T}$  and  $\delta\underline{T}$  there is no sharper bound for the relative error

$||\delta\underline{p}||/||\underline{p}||$  than that given by (1.6). It is for this reason that the criterion for array design was based upon (1.6).

In general the error space defined by vectors  $\delta\underline{p}$  for arbitrary arrays and arbitrary specification of travel-time errors  $\delta t_i$  is extremely complex. To see this consider a three station array with stations at  $(X_i, Y_i)$ ,  $i = 1, 2, 3$ , and arrival-time errors of  $\delta t_1$ ,  $\delta t_2$  and  $\delta t_3$ . If we take for simplicity  $X_1 = Y_1 = 0$  then we have, from (1.3) and (1.4),

$$\begin{pmatrix} \delta p_x \\ \delta p_y \end{pmatrix} = \frac{1}{(X_2 Y_3 - X_3 Y_2)} \begin{pmatrix} Y_3 (\delta t_2 - \delta t_1) - Y_2 (\delta t_3 - \delta t_1) \\ -X_3 (\delta t_2 - \delta t_1) + X_2 (\delta t_3 - \delta t_1) \end{pmatrix}$$

Thus the error space is composed of the space spanned by certain linear combinations of three generally linearly independent unit vectors  $\underline{v}_i$ ,  $i = 1, 2, 3$ . If  $\underline{i}$  and  $\underline{j}$  denote unit vectors along  $\delta p_x$  and  $\delta p_y$  axes respectively, then the  $\underline{v}_i$  are given by,

$$\begin{aligned}
 \underline{v}_1 &= ((Y_2 - Y_3)\underline{i} + (X_3 - X_2)\underline{j}) / ((Y_2 - Y_3)^2 + (X_3 - X_2)^2)^{1/2} \\
 \underline{v}_2 &= (Y_3\underline{i} - X_3\underline{j}) / (Y_3^2 + X_3^2)^{1/2} \\
 \underline{v}_3 &= (-Y_2\underline{i} + X_2\underline{j}) / (Y_2^2 + X_2^2)^{1/2}
 \end{aligned} \tag{1.12}$$

In general then  $\delta\underline{p}$  is a possible error vector if and only if it can be written in the form

$$\delta\underline{p} = \alpha_1\underline{v}_1 + \alpha_2\underline{v}_2 + \alpha_3\underline{v}_3 \tag{1.13}$$

where

$$\alpha_1 = \delta t_1 ((Y_3 - Y_2)^2 + (X_2 - X_3)^2)^{1/2} / (X_2 Y_3 - X_3 Y_2)$$

$$\alpha_2 = \delta t_2 (Y_3^2 + X_3^2)^{1/2} / (X_2 Y_3 - X_3 Y_2)$$

$$\alpha_3 = \delta t_3 (Y_2^2 + X_2^2)^{1/2} / (X_2 Y_3 - X_3 Y_2)$$

Thus from (1.12) and (1.13) the error space  $\delta\underline{p}$ , which depends upon the station locations and the nature of the time errors, is given explicitly. Similar expressions may be derived for  $N > 3$ .

Fortunately there is at least one case of travel-time error specification for which the error space of  $\delta\underline{p}$  vectors is extremely simple even for arbitrary array configurations. If there are  $N$  stations consider the  $N$  dimensional Euclidean vector space with the coordinates of the  $N$  axes given in terms of the travel-time errors

$\delta t_i$ ,  $i = 1, N$ . If the arrival-time error vector  $\delta \underline{t} = (\delta t_1, \delta t_2, \dots, \delta t_n)^T$  is confined to the hypersphere of radius  $\sqrt{N} \delta t$ , where  $\delta t$  is a nominal error, then the error space in the  $(\delta p_x, \delta p_y)$  plane will be a closed ellipse. Details of this case are given in the next section.

#### 'Array Error Numbers' and 'Average' Error

The diagonal matrix form under orthogonal equivalence (Appendix 2) leads to the simplest interpretation about the nature of a square matrix  $A$  as representing a linear transformation from one Euclidean  $n$  space into another such space. It also forms the basis for the calculation of errors  $\delta \underline{p}$  for arbitrary arrays when the travel-time error vector  $\delta \underline{t}$  is confined to the hypersphere of radius  $\sqrt{N} \delta t$ . The resulting error equations are extremely powerful for the purposes of firstly estimating errors for a given array and also for comparing the capacities of different arrays to yield stable estimates of slowness and azimuth.

The results of the preceding paragraph and Appendix 2 may now be applied to the determination of errors in  $\underline{p}$  for any arbitrary array configuration composed of any number of stations  $N \geq 3$  for which the travel-time error vector  $\delta \underline{t} = (\delta t_1, \delta t_2, \dots, \delta t_n)^T$  is

confined to the hypersphere of radius  $\sqrt{N} \delta t$  where  $\delta t$  is a nominal error in arrival time. Extremely useful concepts of 'array error numbers' and average error will be introduced.

The application is possible since we can write the error vector ray parameter equation for  $N \geq 3$  in the following form;

$$\delta \underline{p}_{\text{aug}} = B \delta \underline{t} \quad (1.14)$$

where  $\delta \underline{p}_{\text{aug}}$  is an 'augmented' ( $1 \times N$ ) error vector ray parameter with  $(N-2)$  zeroes given by,

$$\delta \underline{p}_{\text{aug}} = (\delta p_x, \delta p_y, 0, 0, \dots, 0)^T$$

and  $B$  is an 'augmented' array ( $N \times N$ ) matrix which has all zero entries in its  $(N-2)$ -th bottom most rows. The non-zero top two rows of  $B$  depend only upon the station coordinates. The matrix  $B$  has two and only two non-zero singular values  $\mu_1 > \mu_2$ ; hence  $B$  maps hyperspheres in  $\delta \underline{t}$  space into two dimensional ellipses in  $\delta \underline{p}_{\text{aug}}$  space. The diagonal orthogonal equivalent of  $B$ , namely  $D$  say, is of the form  $D = (\mu_{ij}, i, j = 1, \dots, N)$  where  $\mu_{11} = \mu_1$ ,  $\mu_{22} = \mu_2$  and all other  $\mu_{ij} = 0$ . The orthogonal transformation  $V$  (Appendix 2) merely 'rotates' the  $\delta \underline{t}$  space leaving any hypersphere of radius  $\sqrt{N} \delta t$  containing the same elements as before. Also, it is not difficult to show that the orthogonal matrix  $U$  (Appendix 2)

operates on the  $\delta p_{\text{aug}}$  space in such a manner that it only rotates the space in the  $(\delta p_x, \delta p_y)$  plane. Thus, if we make an observation  $p$  for which the root mean square error in arrival time is  $\delta t$  then the error vector  $\delta p$  will be contained within an ellipse in  $(\delta p_x, \delta p_y)$  space which has semi-major and semi-minor axes,  $\delta p_1$  and  $\delta p_2$  respectively given by,

$$\delta p_1 = \mu_1 \sqrt{N} \delta t \quad (1.15)$$

$$\delta p_2 = \mu_2 \sqrt{N} \delta t .$$

The quantities  $\delta p_1$  and  $\delta p_2$  may aptly be referred to as 'array error numbers'. They represent maximum possible errors for a given root mean square error,  $\delta t$ , in arrival time. Among the vectors  $\delta \underline{t}$  of length  $\sqrt{N} \delta t$  in  $\delta \underline{t}$  space there will be one direction for which  $\delta \underline{t}$  and  $-\delta \underline{t}$  map onto the two extremities of the semi-major axes of the  $\delta p$  error ellipse; there will be a direction orthogonal to this one for which  $\delta \underline{t}$  and  $-\delta \underline{t}$  map onto the extremities of the semi-minor axes of the ellipse. The other  $(N-2)$  mutually orthogonal directions are mapped into  $\delta p = 0$  for any length  $||\delta \underline{t}||$ . The quantities  $\delta p_1$  and  $\delta p_2$  are useful since they do give the maximum errors, that is the extremities of the ellipse. For the purpose of comparing errors admitted by two different arrays with the same number of stations one



could compare the areas,  $\pi \delta p_1 \delta p_2$ , of the associated maximum error ellipses of the two arrays.

Points on the maximum error ellipse described above are image points of vectors  $\delta \underline{t}$  of length  $\sqrt{N} \delta t$  which lie entirely within one distinct hyperplane in the  $\delta \underline{t}$  error space. As the number of stations increase the dimension of the  $\delta \underline{t}$  error space increases and hence the probability that  $\delta \underline{t}$  lies entirely within any one hyperplane decreases. Thus the 'effective' errors not only depend upon the maximum errors  $\delta p_1$  and  $\delta p_2$  but also upon the number of stations. In order to study the effect of the number of stations let the  $\delta \underline{t}$  error space be orientated such that it is spanned by unit vectors  $\delta \underline{t}_i$ ,  $i = 1, \dots, N$  and

$$B(\sqrt{N} \delta t \delta \underline{t}_1) = (\delta p_1, 0, \dots, 0)^T$$

$$B(\sqrt{N} \delta t \delta \underline{t}_2) = (0, \delta p_2, 0, \dots, 0)^T$$

and

$$B \delta \underline{t}_i = 0 \quad \text{for } i \geq 3.$$

Now let  $\delta \underline{t}$ , an error vector of length  $\sqrt{N} \delta t$ , be represented by

$$\delta \underline{t} = \beta_1 \delta \underline{t}_1 + \beta_2 \delta \underline{t}_2 + \beta_3 \delta \underline{t}_3 + \dots + \beta_n \delta \underline{t}_n$$

where

$$\sum \beta_i^2 = N \delta t^2.$$

For this vector  $\delta \underline{t}$ , the length of  $\delta \underline{p} = B \delta \underline{t}$  depends upon the component of  $\delta \underline{t}$  in the  $(\delta t_1, \delta t_2)$  plane which is  $(\beta_1^2 + \beta_2^2)^{1/2}$ . If the quantities  $\beta_i$ ,  $i = 1, \dots, N$  are equally likely random variables subject to the constraint that  $\sum \beta_i^2 = N \delta t^2$ , then the most likely value of  $\beta_1^2 + \beta_2^2$  will be  $2 \delta t^2$ . Also, since the direction of the projection of  $\delta \underline{t}$  in the  $(\delta t_1, \delta t_2)$  plane is random, the effective or average error space of vectors  $\delta \underline{p}$  will be defined by the image of a circle in the  $(\delta t_1, \delta t_2)$  plane of radius  $(\beta_1^2 + \beta_2^2)^{1/2} = \sqrt{2} \delta t$  under the transformation B. This image will simply be an ellipse in the  $(\delta p_x, \delta p_y)$  plane with semi-major and semi-minor axes lengths given by  $(2/N)^{1/2} \delta p_1$  and  $(2/N)^{1/2} \delta p_2$  respectively. Notice that this 'average' ellipse is simply a reduced version of the ellipse describing maximum errors. A realistic quantity which reflects an array's capacity to discriminate against random errors is certainly the area of the above 'average' ellipse which is  $(2\pi \delta p_1 \delta p_2)/N$ . Alternatively one could consider the radius of the circle which has the same area as the given ellipse, namely,

$$\delta p_A = \{(2\delta p_1 \delta p_2)/N\}^{1/2}. \quad (1.16)$$

The value  $\delta p_A$  can be referred to as an 'average error' since it takes into account the number of stations and the random nature of the true errors and it is an average over the skewness (elliptical shape) of the error space.

The values  $\delta p_1$ ,  $\delta p_2$ , and  $\delta p_A$  depend only upon the station coordinates. The singular values  $\mu_1$  and  $\mu_2$  of  $B$  are the positive square roots of the two (necessarily positive) non-zero eigenvalues of the matrix  $C = BB^T$ . In general  $C$  will be of the form  $C = \{c_{ij}, i, j = 1, \dots, N\}$  where  $c_{ij} = 0$  if  $i \geq 3$  or  $j \geq 3$ . The generally non-zero quantities  $c_{11}$ ,  $c_{22}$ , and  $c_{12} = c_{21}$  depend only upon the station coordinates. The quantities  $\mu_1$  and  $\mu_2$  are given by:

$$\mu_1 = \{(c_{11} + c_{22} + [(c_{11} + c_{22})^2 - 4(c_{11}c_{22} - c_{12}^2)]^{1/2})/2\}^{1/2} \quad (1.17)$$

$$\mu_2 = \{(c_{11} + c_{22} - [(c_{11} + c_{22})^2 - 4(c_{11}c_{22} - c_{12}^2)]^{1/2})/2\}^{1/2}$$

Thus by (1.15) and (1.17), the array error numbers  $\delta p_1$  and  $\delta p_2$  are given. The average error  $\delta p_A$  is then given by (1.16).

It is not difficult to find the 'tilt' of the error ellipse in the  $(\delta p_x, \delta p_y)$  plane (Golub and Kahan (1964)). Recalling the results of Appendix 2 we have that  $(\delta p_x, \delta p_y, 0, \dots, 0)^T = U(\delta p'_x, \delta p'_y, 0, \dots, 0)^T$ . Now the columns of the orthogonal matrix  $U$  are simply the eigenvectors of the matrix  $C$ ; this fact permits the calculation of  $U$  and hence the angle of rotation in the  $(\delta p_x, \delta p_y)$  plane. Note also that Golub and Kahan (1964) have devised a computational procedure for determining the singular values of general matrices; the procedure,

which is extremely complex analytically, was introduced since in general the calculation of  $BB^T$  for arbitrary matrices  $B$ , using floating point arithmetic does serious violence to the smaller singular values as well as the corresponding eigenvectors which appear in the matrices  $U$  and  $V$  of Appendix 2. It is felt, however, that for this analysis the treatment of Golub and Kahan (1964) is not necessary since the matrices involved are extremely simple (for example,  $B$  contains only two non-zero rows).

Now we need to determine expressions for the augmented array matrix  $B$ , the quantities  $\delta p_1, \delta p_2$  and hence  $\delta p_A$ . Manipulation of equations (1.3) yield  $B$ . If we let  $B = \{b_{k\ell}\}$ ,  $k, \ell = 1, \dots, N$ , then

$$b_{1\ell} = \frac{(\sum Y_i^2 - (\sum Y_i)^2)(\sum X_\ell - \sum X_i) + (\sum X_i \sum Y_i - \sum X_i Y_i)(\sum Y_\ell - \sum Y_i)}{(\sum X_i^2 - (\sum X_i)^2)(\sum Y_i^2 - (\sum Y_i)^2) - (\sum X_i Y_i - \sum X_i \sum Y_i)^2}$$

$$b_{2\ell} = \frac{(\sum X_i^2 - (\sum X_i)^2)(\sum Y_\ell - \sum Y_i) + (\sum X_i \sum Y_i - \sum X_i Y_i)(\sum X_\ell - \sum X_i)}{(\sum X_i^2 - (\sum X_i)^2)(\sum Y_i^2 - (\sum Y_i)^2) - (\sum X_i Y_i - \sum X_i \sum Y_i)^2}$$

$$b_{k\ell} = 0 \quad \text{for } k \geq 3 \quad (1.18)$$

In the above expressions the summations are taken over  $i = 1, \dots, N$ . A calculation of  $C$  yields,

$$c_{11} = N^2 \{ N^2 \Sigma Y_i^2 (\Sigma Y_i^2 \Sigma X_i^2 - (\Sigma X_i Y_i)^2) + N \Sigma Y_i^2 (-\Sigma Y_i^2 (\Sigma X_i)^2) \\ + 2 \Sigma X_i \Sigma Y_i \Sigma X_i Y_i - 2 \Sigma X_i^2 (\Sigma Y_i)^2 + N (\Sigma X_i Y_i)^2 (\Sigma Y_i)^2 \\ + (\Sigma Y_i)^4 \Sigma X_i^2 + (\Sigma X_i)^2 (\Sigma Y_i)^2 \Sigma Y_i^2 - 2 (\Sigma Y_i)^3 \Sigma X_i \Sigma X_i \Sigma Y_i \} / \\ \{ (N \Sigma X_i^2 - (\Sigma X_i)^2) (N \Sigma Y_i^2 - (\Sigma Y_i)^2) - (N \Sigma X_i Y_i - \Sigma X_i \Sigma Y_i)^2 \}^2$$

$$c_{12} = N^2 \{ N^2 \Sigma X_i Y_i ((\Sigma X_i Y_i)^2 - \Sigma X_i^2 \Sigma Y_i^2) + N \Sigma X_i Y_i (-3 \Sigma X_i Y_i \Sigma X_i \Sigma Y_i \\ + (\Sigma Y_i)^2 \Sigma X_i^2 + (\Sigma X_i)^2 \Sigma Y_i^2) + N \Sigma X_i \Sigma Y_i \Sigma X_i^2 \Sigma Y_i^2 \\ + 2 \Sigma X_i Y_i (\Sigma X_i)^2 (\Sigma Y_i)^2 - (\Sigma X_i)^3 \Sigma Y_i \Sigma Y_i^2 \\ - (\Sigma Y_i)^3 \Sigma X_i \Sigma X_i^2 \} / \{ (N \Sigma X_i^2 - (\Sigma X_i)^2) (N \Sigma Y_i^2 - (\Sigma Y_i)^2) \\ - (N \Sigma X_i Y_i - \Sigma X_i \Sigma Y_i)^2 \}^2$$

and

$$c_{22} = N^2 \{ N^2 \Sigma X_i^2 (\Sigma X_i^2 \Sigma Y_i^2 - (\Sigma X_i Y_i)^2) + N \Sigma X_i^2 (-\Sigma X_i^2 (\Sigma Y_i)^2) \\ + 2 \Sigma X_i \Sigma Y_i \Sigma X_i Y_i - 2 \Sigma Y_i^2 (\Sigma X_i)^2 + N (\Sigma X_i Y_i)^2 (\Sigma X_i)^2 \\ + (\Sigma X_i)^4 \Sigma Y_i^2 + (\Sigma Y_i)^2 (\Sigma X_i)^2 \Sigma X_i^2 - 2 (\Sigma X_i)^3 \Sigma Y_i \Sigma X_i Y_i \} / \\ \{ (N \Sigma X_i^2 - (\Sigma X_i)^2) (N \Sigma Y_i^2 - (\Sigma Y_i)^2) - (N \Sigma X_i Y_i - \Sigma X_i \Sigma Y_i)^2 \}^2$$

The values  $\delta p_1$ ,  $\delta p_2$  and  $\delta p_A$  are given by (1.15), (1.16) and (1.17). It is important to realize that these quantities do not depend upon the location in the (X,Y) plane from which the  $X_i$  and  $Y_i$  are measured.

In a previous section it was stressed that the most stable estimates of  $\underline{p}$  result when equations (1.10)

are satisfied. It is not difficult to show that if (1.10) are satisfied then the  $\delta \underline{p}$  error space becomes a circle with  $\delta p_1 = \delta p_2$  and  $\delta p_A = (2/N)^{1/2} \delta p_1$ .

It has been shown that if travel-time errors combine to give a root mean square error of  $\sqrt{N} \delta t$  then the resulting maximum errors in  $\underline{p}$  will be such that  $\delta \underline{p}$  has its tip anywhere on the circumference of an ellipse centered at the origin in the  $(\delta p_x, \delta p_y)$  plane. Also there will be another ellipse, with semi-major and semi-minor axes lengths dependent upon the number of stations, which defines 'most likely' errors  $\delta \underline{p}$ . Examples of the maximum and most likely error ellipses for several array configurations will be given in the next section. It is also interesting to consider resultant maximum errors in the  $(\delta p_x, \delta p_y)$  plane when travel-time errors are not described in the root mean square error sense but in the 'norm-infinity' sense. If we have an error vector  $\delta \underline{t}$  then the vector norm infinity is defined by  $||\delta \underline{t}||_\infty = \max_{1 \leq i \leq N} |\delta t_i|$ . For an  $N \times N$  matrix A, the matrix norm infinity is defined by  $||A||_\infty = \max_{1 \leq i \leq N} \sum_{j=1}^N |a_{i,j}|$  where the  $a_{i,j}$  are the entries of the matrix. Thus if  $||\delta \underline{t}||_\infty$  is given one could determine the quantity  $||\delta \underline{p}||_\infty = \max\{|\delta p_x|, |\delta p_y|\}$  using  $||\delta \underline{p}||_\infty \leq ||B||_\infty ||\delta \underline{t}||_\infty$  and equations (1.18). Instead of considering this maximum,  $||\delta \underline{p}||_\infty$ , it is much more interesting and instructive to determine the

'boundary' in the  $(\delta p_x, \delta p_y)$  plane when it is assumed that  $-\delta t \leq \delta t_i \leq \delta t$  for all  $\delta t_i$  where  $\delta t > 0$  is a nominal travel-time error. Notice that this travel-time error specification is quite different than the root mean square error case. Using equations (1.14) and (1.18) it is possible to determine this boundary. In general the boundary in the  $(\delta p_x, \delta p_y)$  plane is a multisided figure which has a degree of symmetry dependent upon the degree of symmetry of the array. This maximum 'norm-infinity' boundary will also be shown in the following examples.

#### Examples

Much emphasis has been placed upon the concepts of condition number, maximum and most likely error ellipses, and the average error  $\delta p_A$ . The following examples illustrate the importance of these concepts and also show the relationship between spectral or root mean square errors and norm-infinity errors. In order to compare the capacities of different arrays to discriminate against travel-time errors it is necessary to ensure that the sizes, in some sense, of the arrays are comparable. To this end the 'mean' aperture of all of the following arrays are equal. The horizontal extent of an array depends upon the azimuth from which the array is viewed; if  $a_l$  and  $a_s$  are the largest and

smallest apertures of the array then the geometric mean aperture,  $a_m$ , is defined to be  $a_m = \sqrt{a_l a_s}$ . Figures 1.2, 1.3, 1.4 and 1.5 show various array configurations together with their corresponding spectral and norm-infinity error spaces. The distance scale factor  $\Delta L$  and slowness scale factor  $\delta p$  are such that when  $\Delta L = 200$  km and the nominal travel-time error  $\delta t = 0.1$  sec, then  $\delta p = 0.1$  sec/100 km and all of the arrays have a mean aperture of 200 km. The errors for any travel-time error and array size can thus be determined by using the relation  $\delta p \propto \delta t / \Delta L$ .

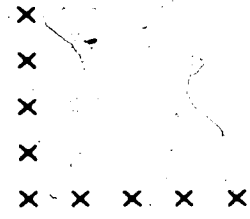
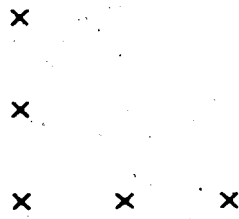
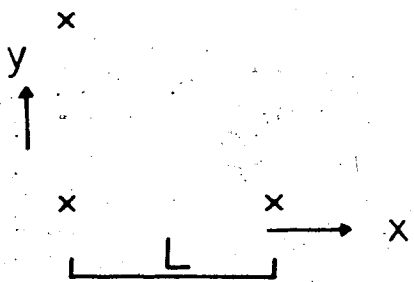
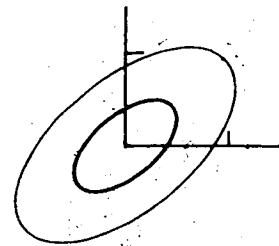
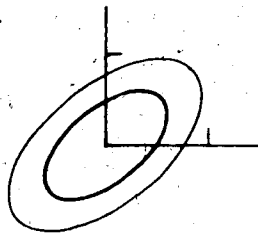
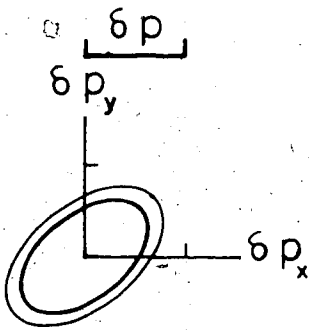
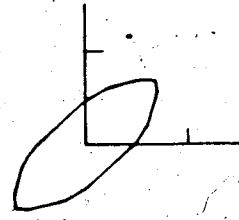
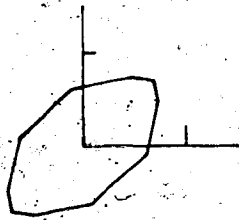
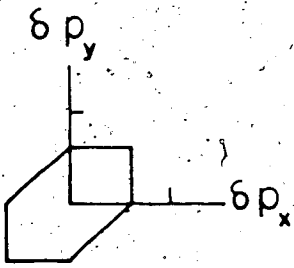
Three, five, and nine station L-shaped arrays are shown in figures 1.2a, 1.2b, and 1.2c; they will be referred to as arrays 2a, 2b, and 2c. The feature that all three of these arrays have in common is that they are asymmetric; accordingly for all three arrays the spectral error space is elliptical, not circular, and  $\kappa(A) > 1$ . The tilt of the ellipses (the semi-major axis is inclined at an angle of  $45^\circ$  counterclockwise from the  $\delta p_x$  axis) reflects the asymmetry of the arrays. Notice that as we proceed from three to five to nine stations the following take place;

- (i) the condition numbers increase (from 2.5 to 2.9 to 3.1)
- (ii) the spectral error spaces become more elliptical (error ellipses acquire larger eccentricities).



Figure 1.2

Three, five, and nine station L-shaped arrays are shown in parts a, b, and c respectively. Immediately above each array the maximum spectral error ellipse (light boundary) and most likely spectral error ellipse (dark boundary) are shown. The scale factors shown are such that when  $L = 100$  km, and  $\delta t = 0.2$  sec then  $\delta p = 4.0 \times 10^{-3}$  sec/km. In this case the values of  $\delta p_A$  (in the order a, b, and c) are  $\delta p_A = 4.6 \times 10^{-3}$  sec/km,  $4.3 \times 10^{-3}$  sec/km, and  $3.6 \times 10^{-3}$  sec/km. If  $L = 100$  m and  $\delta t = 2$  ms, then  $\delta p = 4.0 \times 10^{-2}$  sec/km and (in the order a, b, c)  $\delta p_A$  becomes  $4.6 \times 10^{-2}$  sec/km,  $4.2 \times 10^{-2}$  sec/km, and  $3.6 \times 10^{-2}$  sec/km. Immediately above the spectral error space diagrams the maximum norm-infinity error boundary is shown for all three arrays. The hash marks on the slowness axes of all slowness error diagrams are  $\delta p$  from the origin.



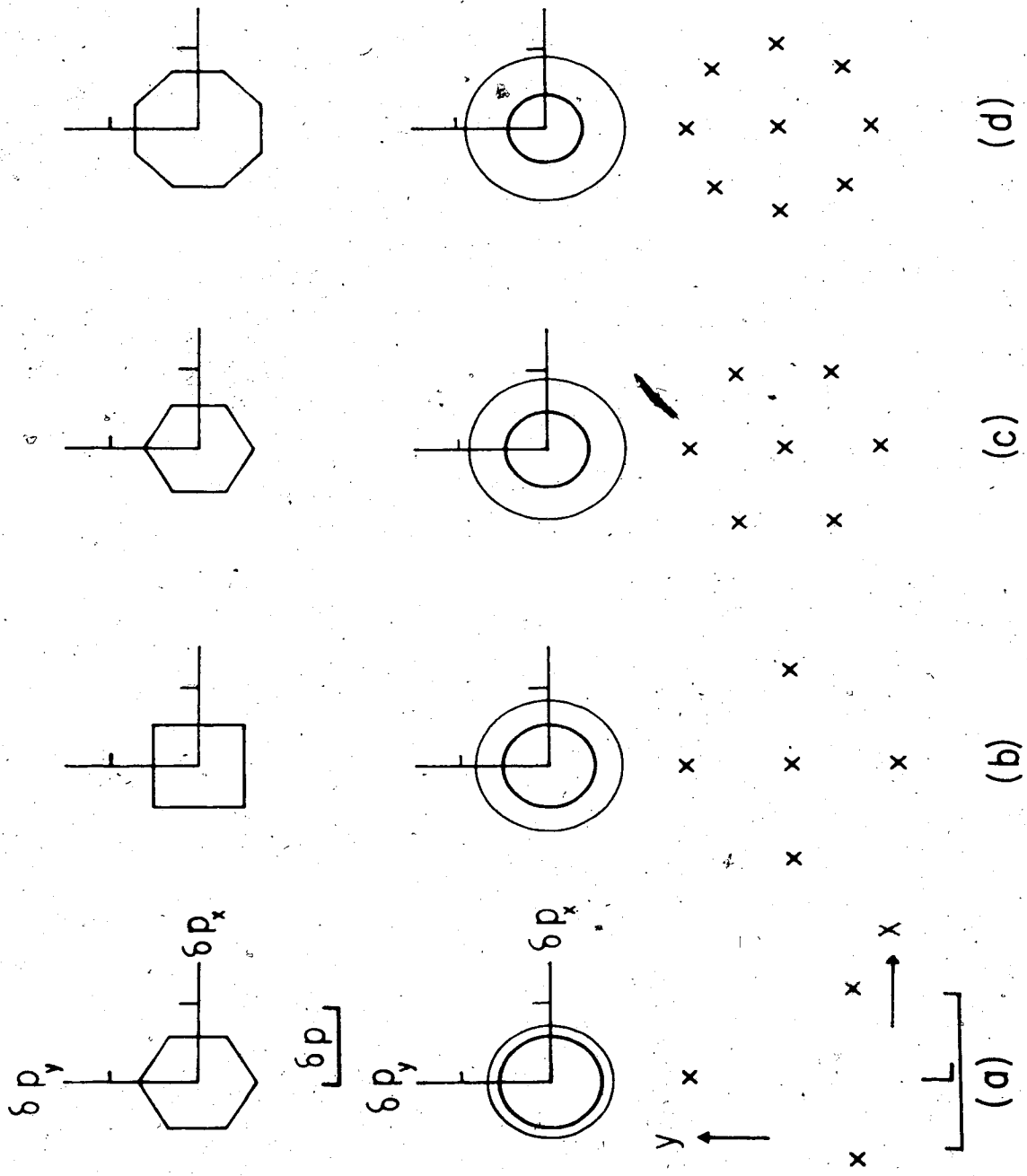
(a)

(b)

(c)

Figure 1.3

Three, five, seven, and nine station "circular" arrays are shown in parts a, b, c, and d respectively. The corresponding maximum spectral error circle (light boundary) and most likely spectral error circle (dark boundary) are shown immediately above each array. The scale factors shown are such that when  $L = 100$  km, and  $\delta t = 0.2$  sec, then  $\delta p = 4.0 \times 10^{-3}$  sec/km. In this case the values of  $\delta p_A$  (in the order a, b, c, and d) are  $4.6 \times 10^{-3}$  sec/km,  $4.2 \times 10^{-3}$  sec/km,  $3.8 \times 10^{-3}$  sec/km, and  $3.4 \times 10^{-3}$  sec/km. If  $L = 100$  m and  $\delta t = 2$  ms, then  $\delta p = 4.0 \times 10^{-2}$  sec/km and (in the order a, b, c)  $\delta p_A$  is  $4.6 \times 10^{-2}$  sec/km,  $4.2 \times 10^{-2}$  sec/km,  $3.8 \times 10^{-2}$  sec/km, and  $3.4 \times 10^{-2}$  sec/km. Immediately above the spectral error diagrams the maximum norm-infinity error space is shown for all four arrays. The hash marks on all slowness error diagrams are at  $\delta p$  from the origin.



(d)

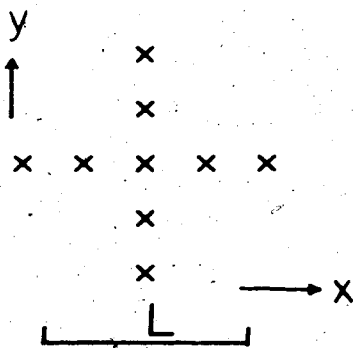
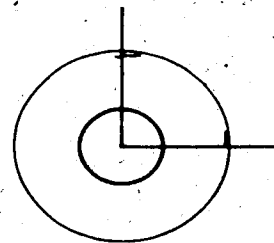
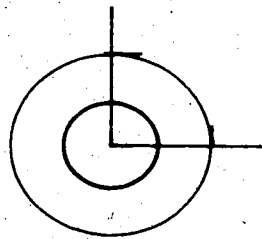
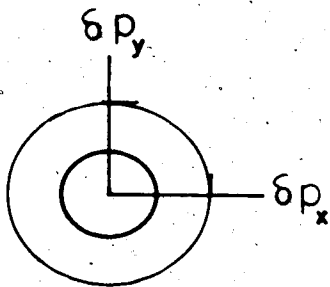
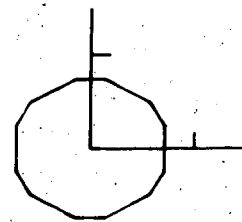
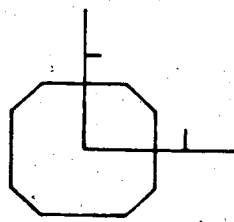
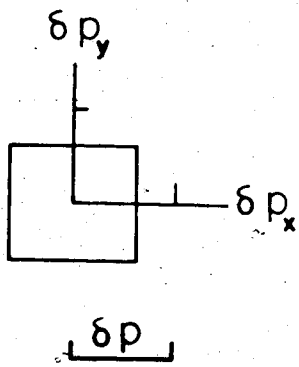
(c)

(b)

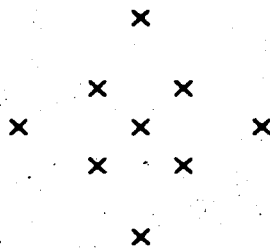
(a)

Figure 1.4

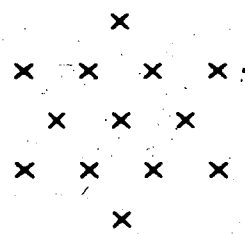
Two nine station and a thirteen station "double circle" arrays appear in parts a, b, and c respectively. The corresponding maximum spectral error circle (light boundary) and most likely spectral error circle (dark boundary) are shown immediately above each array. The scale factors shown are such that when  $L = 100$  km and  $\delta t = 0.2$  sec, then  $\delta p = 4.0 \times 10^{-3}$  sec/km. In this case the values of  $\delta p_A$  (in the order a, b, and c) are  $\delta p_A = 3.7 \times 10^{-3}$  sec/km,  $3.7 \times 10^{-3}$  sec/km, and  $3.2 \times 10^{-3}$  sec/km. If  $L = 100$  m and  $\delta t = 2$  ms, then  $\delta p = 4.0 \times 10^{-2}$  sec/km and (in the order a, b, c)  $\delta p_A$  is  $3.7 \times 10^{-2}$  sec/km,  $3.7 \times 10^{-2}$  sec/km, and  $3.2 \times 10^{-2}$  sec/km. Immediately above the spectral error diagrams the maximum norm-infinity error space is shown for each array. The hash marks on all slowness error diagrams are at  $\delta p$  from the origin.



(a)



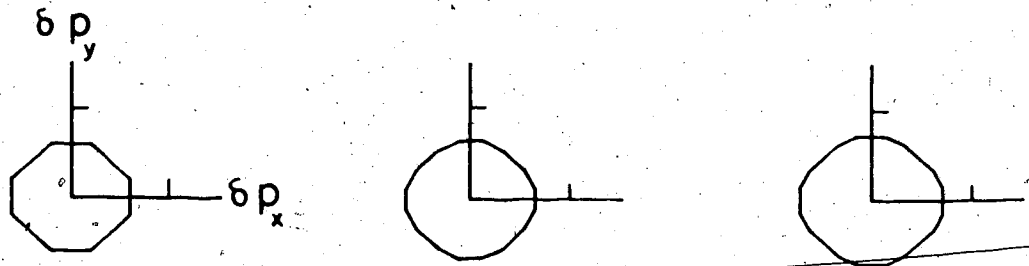
(b)



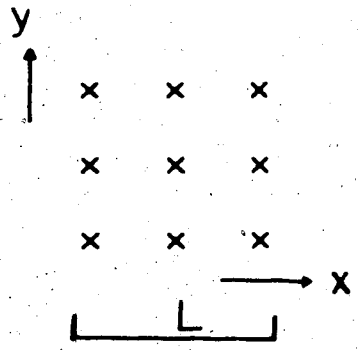
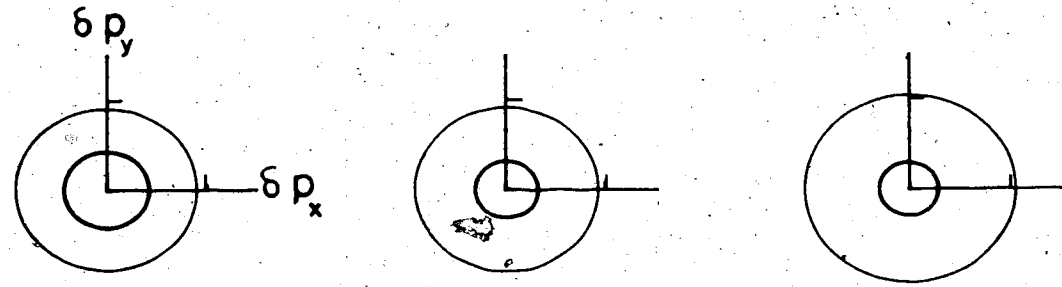
(c)

Figure 1.5

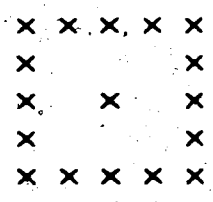
Nine, seventeen, and twenty-five station "box" arrays appear in parts a, b, and c respectively. The corresponding maximum spectral error circle (light boundary) and most likely spectral error circle (dark boundary) are shown immediately above each array. The scale factors shown are such that when  $L = 100$  km, and  $\delta t = 0.2$  sec, then  $\delta p = 4.0 \times 10^{-3}$  sec/km. In this case the values of  $\delta p_A$  (in the order a, b, and c) are  $\delta p_A = 3.4 \times 10^{-3}$  sec/km,  $2.5 \times 10^{-3}$  sec/km, and  $2.4 \times 10^{-3}$  sec/km. If  $L = 100$  m and  $\delta t = 2$  ms, then  $\delta p = 4.0 \times 10^{-2}$  sec/km and (in the order a, b, c)  $\delta p_A$  is  $3.4 \times 10^{-2}$  sec/km,  $2.5 \times 10^{-2}$  sec/km, and  $2.4 \times 10^{-2}$  sec/km. Immediately above the spectral error diagrams the maximum norm-infinity error space is shown for each array. The hash marks on all slowness error diagrams are at  $\delta p$  from the origin.



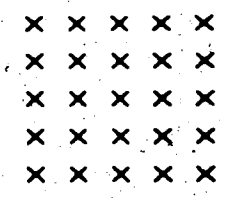
$\delta p$



(a)



(b)



(c)



(iii) the arrays become more and more asymmetric with the L-shape being more well defined.

The above features are related. In general larger condition numbers are associated with more asymmetric arrays and more eccentric error spaces. One might suspect that the ratio  $a_s/a_l$  is equal to the ratio of the semi-minor to the semi-major axes of the ellipse. This is not the case however; for example using array 2a we get  $a_s/a_l = 0.5$  and the ratio of the ellipse axes is approximately 0.57. The reason for this is that the analysis not only takes into account the extreme apertures of an array but also the spatial distribution of stations along the directions of the extreme apertures. Notice also that as the number of stations is increased the maximum error ellipse becomes larger. This is a result of the fact that the addition of stations is performed in a manner such that the station spacing is reduced. On the other hand, the most likely error ellipse diminishes in extent as the number of stations is increased. Starting with array 2a the improvement obtained by the addition of 2 stations (array 2b) is such that  $\delta p_A$  decreases by approximately 7%. Four additional stations (2c) improve errors by 16% when compared to array 2b. Also shown is the maximum norm-infinity error space; the boundary is generally multi-sided and its orientation again reflects the asymmetry of the array. As the number of stations increase the

boundary acquires more facets approaching the elliptical shape of the spectral error space. The boundary of the norm-infinity error space falls between the maximum and most likely spectral error ellipses in all cases.

Figure 1.3 shows 3, 5, 7 and 9 station circular arrays and their error spaces. All of these arrays have station locations which satisfy equation (1.10) and hence  $\kappa(A) = 1$  and the spectral error spaces are circular. The radius of the maximum error circle increases as the number of stations increase. The radius of the most likely error circle, as expected, decreases as the number of stations increase. In fact  $\delta p_A$  decreases almost linearly as the number of stations increase;  $\delta p_A$  diminishes by approximately  $\delta t/5\Delta L$  with the addition of every two stations. The norm-infinity error spaces are multisided figures with a higher degree of symmetry than those for the L-shaped arrays. The norm-infinity boundary for the nine station array 3d is the most 'circular'. Again the norm-infinity error boundary lies between the maximum and most likely spectral error circles. It is interesting to compare the effectiveness of these circular arrays and the previously discussed L-shaped arrays. Comparing arrays with the same number of stations it is seen that the circular arrays are more favourable in all cases with the improvement in corresponding  $\delta p_A$  being the largest for the nine station arrays. The disparity

in  $\delta p_A$  is not extreme with the ratio of  $\delta p_A$  for array 3d to  $\delta p_A$  for array 2c being approximately 0.94. A comparison of maximum errors allowed by the two array configurations again shows that the circular arrays are more favourable in all cases and the improvement is again most pronounced for the nine station arrays. The disparity in maximum errors is much more pronounced than the improvement in  $\delta p_A$ ; for example the ratio of the maximum error allowed by array 3d to that of array 2c is approximately 0.67. The superiority of the circular arrays is related to the fact that their corresponding condition numbers are equal to unity; the L-shaped arrays have  $\kappa(A) > 1$ .

Figure 1.4 shows the double circular arrays 4a, 4b, and 4c. Notice that the spectral error spaces of the nine station arrays 4a and 4b are identical. This 'rotational symmetry' is a feature common to arrays for which  $\kappa(A) = 1$ . Notice however that the maximum norm-infinity errors of 4a and 4b do not coincide. A comparison of the value  $\delta p_A$  for arrays 4a and 4b with the value of  $\delta p_A$  for the nine station array 3d shows that the single circle arrangement is preferable;  $\delta p_A$  is smaller by about 10 percent. The thirteen station array 4c shown has a configuration which contains many equilateral triangle components which are themselves capable of smaller aperture estimates of slowness and azimuth.

Its maximum norm-infinity boundary is multisided and closely approximates a circle.

The nine, seventeen, and twenty-five station box arrays are shown in figures 1.5a, 1.5b, and 1.5c respectively; all have circular spectral error spaces. The maximum norm-infinity error space becomes more 'circular' and larger as the number of stations is increased.. A comparison of the effectiveness of these arrays is very interesting. The addition of 8 extra stations to the 'periphery' of array 5a results in array 5b; the error improvement is such that  $\delta p_A$  decreases by about 26 percent. If an additional 8 stations are added, this time to the interior of the box, the result is array 5c. This last step results in an improvement of only about 7 percent. This situation again shows that an array is most effectively upgraded by the addition of stations if the new stations are placed along the periphery of the existing array and not added to the interior.

A general feature of spectral errors is that the size of spectral error spaces is directly proportional to the nominal travel-time error  $\delta t$  and inversely proportional to array size. The travel-time error dependence is clearly seen and the nature of the array size dependence can be explicitly stated as follows; if an array defined by  $(X_i, Y_i)$ ,  $i = 1, \dots, N$  has errors  $\delta p_1, \delta p_2$ , and  $\delta p_A$  then the array defined by  $(cX_i, cY_i)$ ,  $i = 1, \dots, N$

where  $c > 0$  has errors  $p_1/c$ ,  $p_2/c$ , and  $p_A/c$ . Now let us consider a 21 element L-shaped array for which each leg of the L is 25 km and accordingly the station spacing along each leg is 2.5 km. If  $\delta t = 0.1$  sec, then  $\delta p_1 = 2.3 \times 10^{-2}$  sec/km,  $\delta p_2 = 1.2 \times 10^{-2}$  sec/km, and  $\delta p_A = 0.5 \times 10^{-2}$  sec/km. If this array is now magnified by a factor  $c = 8$  such that the legs of the L become 200 km and the station spacing along each leg is 20 km, then the errors are (for  $\delta t = 0.1$  sec)  $\delta p_1 = 2.9 \times 10^{-3}$  sec/km,  $\delta p_2 = 1.4 \times 10^{-3}$  sec/km, and  $\delta p_A = 0.6 \times 10^{-3}$  sec/km. Now an important travel-time error results from miscorrelation of phases from one record to another; in general the accuracy of correlation increases as station spacing becomes smaller. Thus if phase identification is the only source of error, then the smaller L-shaped array described above will be as effective as the larger array if the smaller station spacing decreases the phase identification error by a factor of 8.

### Conclusions

Errors in slowness and azimuth measurements from two dimensional seismic arrays depend upon array geometry, array size, and the nature of travel-time errors. For travel-time errors defined in the root mean square

error sense it has been shown that the maximum errors in slowness and azimuth are defined by a spectral error ellipse in the slowness-azimuth error diagram for any array. Values of expected errors are then defined by a reduced version of the maximum spectral error ellipse. In general the stability of the inverse problem is related to the condition number associated with an array. Symmetric arrays have associated condition numbers equal to unity and circular spectral error spaces in the slowness-azimuth error plane. As array asymmetry becomes more pronounced, condition numbers increase and spectral error spaces become more elliptical. Comparisons between symmetric and asymmetric arrays with the same number of stations and equal mean apertures reveal that symmetric arrays are more favourable in terms of stable measurements of slowness and azimuth. The equations developed show that slowness and azimuth error analysis need not be restricted to the case of spectral errors. In particular if it assumed that travel-time errors at each station are bounded, then it is possible to construct the 'norm-infinity' error boundary in the slowness-azimuth error plane. The norm-infinity error space boundaries are generally multisided figures with a degree of symmetry dependent upon the degree of symmetry of the array and the travel-time error bounds.

The analysis shows that the most effective procedure for error improvement is to add additional stations along the periphery of an existing array and to make the array as symmetric as possible. The size and station spacing of the array should, of course, be as large as possible but must be limited by the spectral character of the noise, the degree of correlation between signals at widely spaced stations, and the validity of the plane wave approximation. A large number of stations may be necessary for enhancement of weak signals in the presence of strong random noise but if the signal to noise ratio is adequate and the errors are due to terrestrial inhomogeneities it is probably better to use several adjacent arrays with a modest number of detectors (5 to 9) instead of a single array with many detectors.

## CHAPTER 2

### TELESEISMIC SLOWNESS AND AZIMUTH MEASUREMENTS: THE 1974 VARIABLE APERTURE SEISMIC ARRAY

#### Introduction

Medium and large aperture seismic arrays have been widely used in past for the determination of the apparent slowness and azimuth of various teleseismic phases. In this chapter a study of the slowness and azimuth of P phases, for which the rays bottom in the lower mantle, as recorded by the 1974 Variable Aperture Seismic Array, (VASA), will be presented. Usually results are compared to values predicted by some standard earth model such as that given by Jeffreys and Bullen. The Jeffreys-Bullen velocity depth profile is spherically symmetric and is consistent with an earth that is chemically homogeneous within the lower mantle. A departure of the velocity gradient at a given depth from that given by the Jeffreys-Bullen model points to an 'inhomogeneity' in the lower mantle. Changes in the ray parameter,  $p$ , as a function of distance are extremely sensitive to anomalous velocity gradients. On the other hand, a large change in velocity gradient which corresponds to a small change in velocity has very little effect on the observed travel time between about 30 and 100 degrees epicentral distance. Thus array measurements of  $\sigma = dT/d\Delta$



for the P phase are extremely important. In early studies it was assumed that departures of the velocities within the lower mantle from the Jeffreys-Bullen model were radial in nature. Thus, initially it was assumed that the azimuth of the incoming plane wave was the great circle azimuth between the array and the location of the seismic event as given by the world-wide seismic network determination; calculations of  $p$  were made with this azimuthal constraint. In later studies Gopalakrishnan (1969) for example, calculations of both slowness and azimuth were made but only information about the ray parameter  $p$  was retained; any event for which the calculated azimuth deviated from the expected great circle azimuth by more than about 4 degrees was discarded on the basis that the measurement was grossly in error. Still later it was thought that the lower mantle could possibly be laterally as well as radially homogeneous. Thus both slowness and azimuth information were retained. Davies and Sheppard (1972), for example, plotted slowness and azimuthal deviations on the 'array diagram'. Thus both slowness and azimuth measurements are important. In accordance with this, results from VASA 1974 will be presented in the standard  $\Delta(p)$  plane and in the slowness-azimuth 'array diagram'. Also in view of the importance of the function  $\tau(p)$  (Bessonova et al (1974) and Bessonova et al (1976)) in crustal, upper mantle, and

lower mantle studies, results will also be presented in the  $\tau(p)$  plane. Before these results are presented, details of the 1974 variable aperture seismic array, the method of data acquisition and reduction, and the 'COVESPA' process (used to determine slowness and azimuth) will be given.

### The 1974 Variable Aperture Seismic Array

The portable 1974 VASA consists of the six most southerly stations shown in figure 2.1. Notice that this arrangement of stations is highly symmetrical, an important feature in view of the results of Chapter 1. In order to increase its capacity, the array was extended to include the permanent station EDM. For the purpose of calculating  $dT/d\Delta$  and azimuth of teleseismic P waves, this extended array was divided into two sub-arrays, VASA1 and VASA2. The sub-array, VASA1, consists of the stations EAT, FOR, HAN, MAP, SES, and VUL, and VASA2 consists of the stations EAT, HAN, SES, VUL, and EDM. Thus the arrays VASA1 and VASA2 are large aperture type seismic arrays and are therefore capable of yielding stable estimates of  $dT/d\Delta$  and azimuth. For reference, the locations and elevations of the stations are given in Table 2.1.

Figure 2.1

Array location map. The 1974 Variable Aperture Seismic Array, VASA, consists of the six most southerly stations Eatonia (EAT), Foremost (FOR), Hanna (HAN), Mape Creek (MAP), Suffield (SES), and Vulcan (VUL). The permanent station Edmonton (EDM) augments the 1974 VASA.

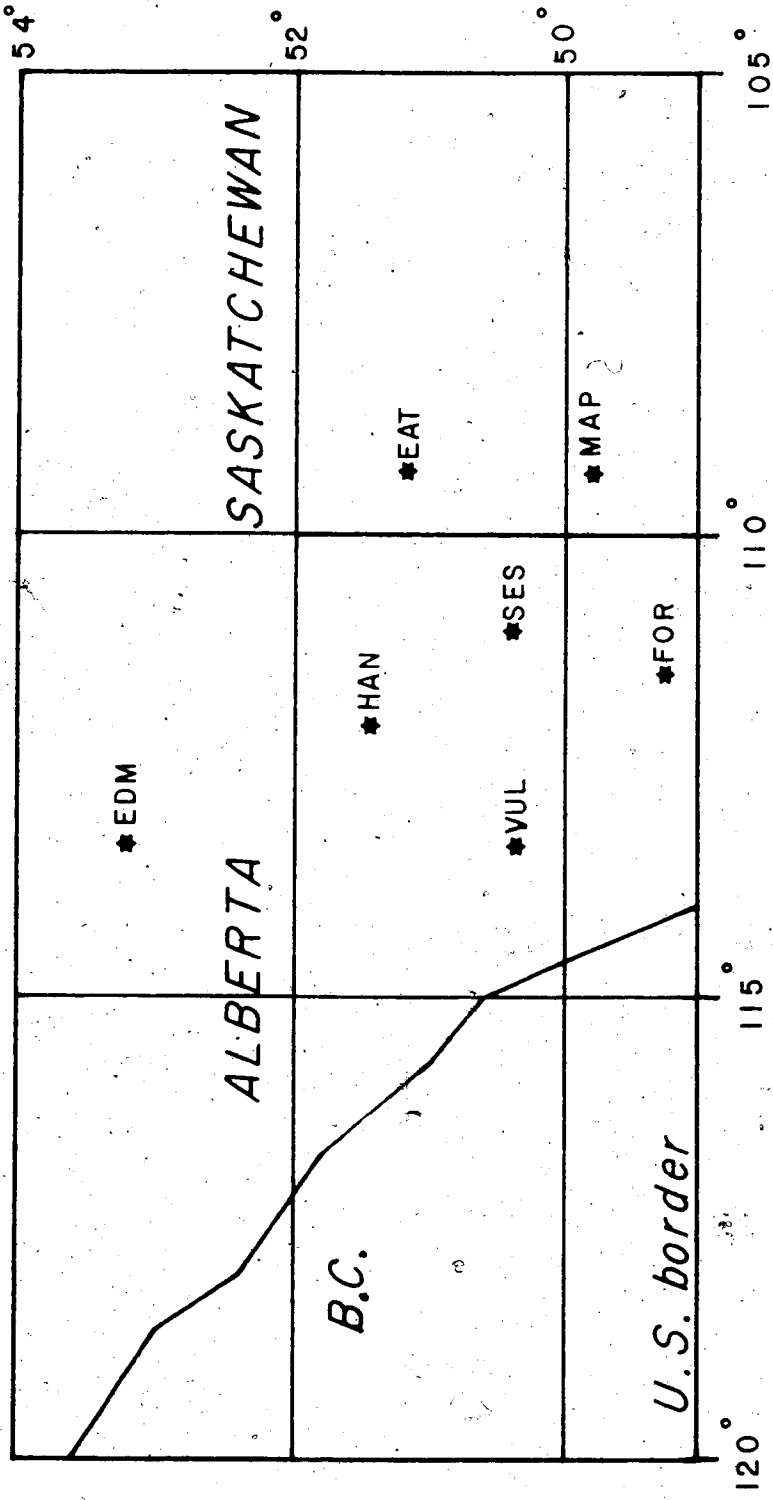


Table 2.1  
1974 VASA Station Locations

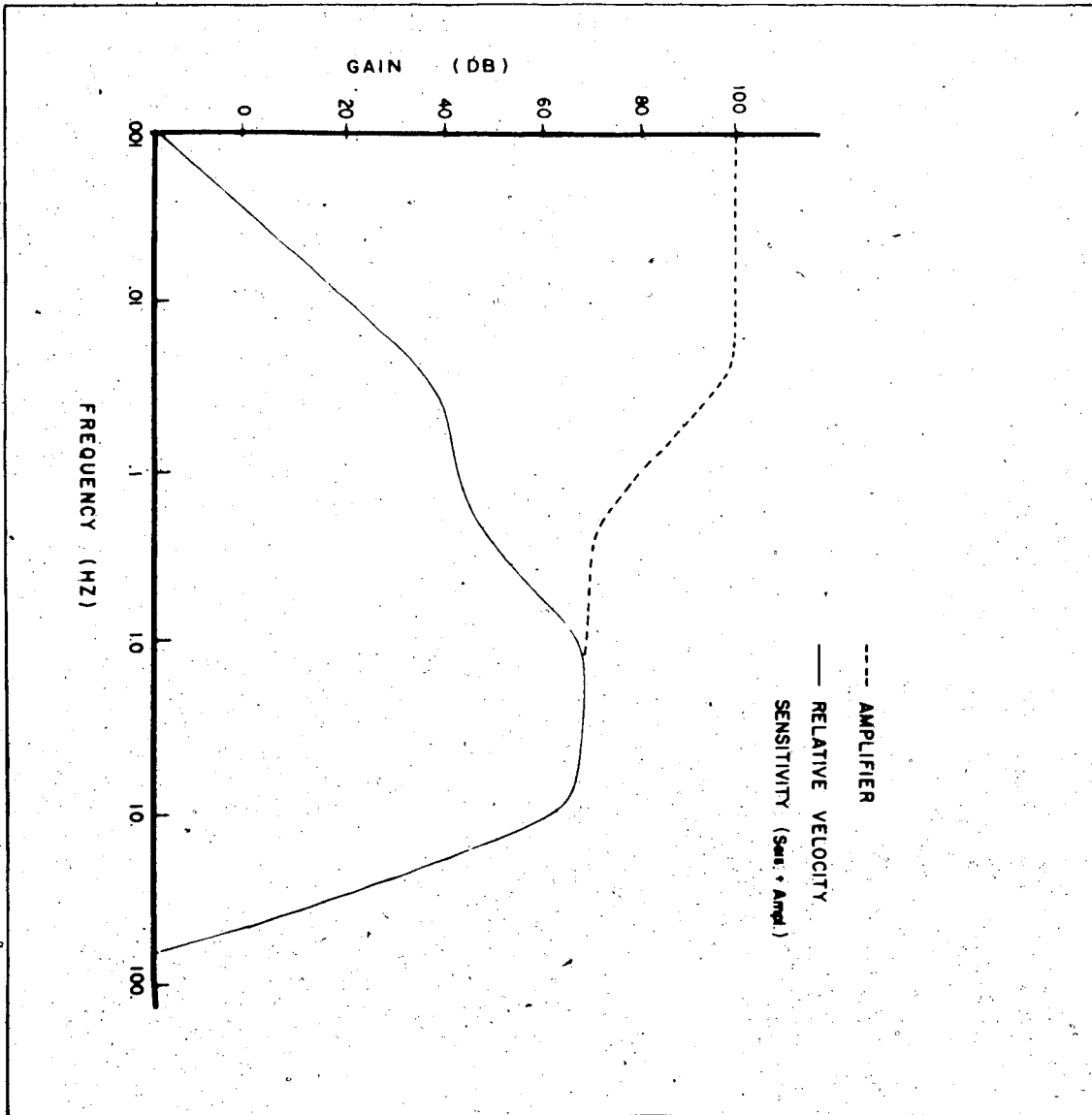
| Station                   | Code Name | Latitude   | Longitude   | Elevation (km) |
|---------------------------|-----------|------------|-------------|----------------|
| Eatonia, Saskatchewan     | EAT       | 51° 11.11' | 109° 18.93' | 0.70           |
| Foremost, Alberta         | FOR       | 49° 15.34' | 111° 30.33' | 0.97           |
| Hanna, Alberta            | HAN       | 51° 27.05' | 112° 3.73'  | 0.93           |
| Maple Creek, Saskatchewan | MAP       | 49° 47.73' | 109° 20.52' | 0.95           |
| Suffield, Alberta         | SES       | 50° 23.75' | 111° 2.50'  | 0.77           |
| Vulcan, Alberta           | VUL       | 50° 22.03' | 113° 21.82' | 1.07           |
| Edmonton, Alberta         | EDM       | 53° 13.37' | 113° 20.90' | 0.73           |

Each station consists of three Willmore Mark II seismometers (one vertical and two horizontal measuring north-south and east-west motion), a WWVB receiver, amplifiers, a multiplexer, and an analog to digital converter. Kanasewich et al (1974) discuss the essential features of the tripartite digital recording gain ranging system. The response of the amplifier and a Willmore Mark II seismometer is shown in figure 2.2. The desirable feature of the response is that it is flat over the frequency range of teleseismic P waves (about 0.7 to 1.8 Hz).

The procedure for editing raw seismic data recorded by the portable field system has become routine at the

Figure 2.2

Amplifier gain of the tripartite system and the combined response of the amplifier and a Wilmore Mark II seismometer.



University of Alberta. Data selected from the 7-track magnetic field tapes are transferred to 9-track tape by means of a PDP 11 computer. In general the sampling rate is variable but data used in this experiment were sampled at 12.5 samples/sec per channel (except for a few at SES which were sampled at  $6\frac{1}{4}$  samples/sec per channel). Information from each seismic event, for each station, is contained in two files on final master tapes. The first file contains the statistics of the event; that is the location of the epicenter, the magnitude, the focal depth, the origin time, the distance and azimuth from the station, the Jeffreys-Bullen arrival time of the P phase at the station, and the ellipticity and elevation corrections. The second file contains the seismic data - the vertical, radial, and transverse traces and the WWVB signal (radial and transverse traces are obtained assuming a great circle path from the epicenter to the station). All four channels are stored in (four byte) integer format with the data file composed of blocks of 8192 bytes. With a sampling rate of 12.5 samples/sec per channel this means that there are approximately 163.84 seconds of seismic information per block. The data on the final master tapes is written in cyclical fashion with respect to the channels; thus the first four words are the first entries of the vertical, radial and transverse traces and the WWVB



signal respectively, with the fifth word being the second entry of the vertical channel. For a sampling rate of 12.5 samples/sec per channel, there is a time shift between successive channels of 20 milliseconds on the original field tapes. On the final master tapes the first three channels are time shifted, by means of a simple linear interpolation scheme, so that all three are synchronous with the WWVB channel. Accurate time resolution is accomplished by cross correlating the actual WWVB signal with a synthetic WWVB time signal in binary pulse code format 96 sec long. A visual determination of the actual WWVB signal ensures that both signals contain the same minute mark. The maximum cross-correlation then corresponds to the coincidence of the two minute marks and the fraction of the sampling interval (80 ms) for which the maximum occurs is determined by a three point fit to the correlation values. It has been pointed out by Gutowski (1974) that for good signal to noise characteristics the precision of such a time determination is to within  $1/4$  of a sampling interval which is 20 ms for a sampling rate of 12.5 samples/sec per channel. Verification of this result has been performed by decoding separated portions of the actual WWVB signal. With accurate timing available the master tapes have been arranged such that the time corresponding to the beginning of the first block is two minutes before

the JB arrival time of the P phase. Data on the master tapes are written with all stations recording an event following one another. Events are arranged chronologically according to their time of occurrence. For this experiment the data from the station EDM required special handling. The EDM data is transmitted via a data link to the seismic laboratory at the University of Alberta with a sampling rate of 18 samples/sec per channel. The EDM data has been modified so that it is present on the master tapes in the standard form. As in past (Gutowski (1974)) the organizational scheme described above has proved to be convenient for the study of teleseismic P phases. Also, it is expected that such an arrangement will prove useful for future seismic studies.

#### Velocity Spectral Analysis and the Covespa Process

Velocity filtering techniques have been widely used for the determination of the apparent velocities of wavefronts which traverse seismic arrays. The design of many velocity filters is based upon the assumptions that the frequency spectra of signal and noise are disjoint or that the noise, unlike the signal, is incoherent across the array. An exhaustive treatment of the time delay - summation process (stacking) and cross correlation techniques, in conjunction with one and two

dimensional arrays, is given by Birtill and Whiteway (1965). In the oil industry, the examination of contour plots of cross correlation values or 'coherency' in the apparent velocity-time plane has long been standard practise for the purposes of the identification of primary and multiple reflections and the determination of interval velocities (Schneider and Backus (1968) and Taner and Koehler (1969), for example). Davies et al (1971) used the summation process to determine the velocity spectra, 'Vespa', of teleseismic wavefronts traversing LASA; the azimuth of the wavefronts was assumed to be that given by the great circle path between the event and the array and results were illustrated by the 'Vespagram'. Later, Doornbos and Husebye (1972) used the method of Davies et al (1971) and cross correlation techniques in order to study the apparent velocity of core phases. Wiechert et al (1967) determined the velocity and azimuth of teleseismic waves arriving at the Yellowknife seismic array by examining the square summation of traces. A complete treatment of velocity filtering in general is given by Kanasevich (1975).

The 'Covespa' technique (Gutowski (1974)) is an extremely powerful spectral method for determining slowness and azimuth and has been employed in this study. For a given azimuth,  $\theta$ , slowness,  $p$ , and time,  $t$ , the coherency,  $CC$ , is given by,

$$CC(\theta, p, t) = \frac{2}{M(M-1) \cdot T} \sum_t \sum_k \sum_i \frac{f_{i,t}(\theta, p) \cdot f_{i+k,t}(\theta, p)}{\left\{ \sum_t f_{i,t}^2 \cdot \sum_t f_{i+k,t}^2 \right\}^{1/2}} \quad (2.1)$$

where  $M$  is the number of sensors,  $k$  is an incremental integer on channel  $i$  ( $i \neq k$ ),  $T$  is the length of the time window (1 second for this study), and  $f_{i,t}$  is the amplitude of the  $i^{\text{th}}$  channel at time  $t$ . The traces from the  $M$  sensors are shifted in time by the amounts determined by the particular choices of  $p$  and  $\theta$ . For each time along the records the zero lag cross correlations of all combinations of two stations are computed, normalized to unity and summed. Thus  $CC = 1$  at a given time, slowness, and azimuth if the phases and waveforms of the signal within the window are the same at all sensors. For this study the Covespa technique has been applied to the vertical traces with a time window of 1 second.

A contour plot of coherency in the slowness-time plane is known as a 'Covespagram'. The range of acceptable coherencies is set at  $0.5 \leq CC \leq 1.0$  to ensure meaningful interpretation of Covespagrams. Gutowski (1974) has shown that the Covespagram pattern remains stable upon variation of relative amplitudes of waveforms across an array and that an increase in wave train duration merely results in an extended Covespa pattern.

An example of the resolving capacity of the Covespa process when applied to coherent signals embedded in 'random' noise is here shown in figures 2.3 and 2.4 for signal to noise amplitude ratios of 4:1 and 1:1 respectively. The signals are six synthetic two cycle duration sinusoidal phases of frequency 0.75 Hz traversing the VASAL array with slowness of 5.0, 4.8, 4.6, 4.4, 4.2, and 4.0 sec/deg at an azimuth of 140 degrees. In order of decreasing slowness the phases arrive at Eatonia at 5, 15, 25, 35, 45, and 55 seconds. Each of figures 2.3 and 2.4 shows the input signal at Eatonia and the simple stack or 'beam' for a slowness of 4.6 sec/deg beneath the Covespagram. The random noise was synthesized by generating a 'random' pulse of the form  $Ae^{-\alpha t} \cos \omega t$  where  $A$  and  $\omega$  are random Gaussian variables and  $\alpha > 0$  is a fixed decay constant, at each digital point. The resultant noise was taken to be the sum of such random pulses. The Covespa patterns in figures 2.3 and 2.4 consist of contours of isolated 'hills'; the contour value at the base of each hill is 0.5 and the contour interval is 0.1. From figures 2.3 and 2.4, we see that the Covespa process has successfully extracted the signals at the required slownesses and times; the 'brightness' of the phases in the Covespagrams diminishes as the signal to noise ratio decreases. The superiority of Covespa as a

Figure 2.3

Covespagram for six synthetic events traversing the 1974 VASA. Signal to noise amplitude ratio is 4:1. The vertical trace immediately below the Covespagram is the synthetic seismogram at Eatonia. The coherent pulses at 5.0, 15.0, 25.0, 35.0, 45.0, and 55.0 sec cross the array at slowness values of 5.0, 4.8, 4.6, 4.4, 4.2, and 4.0 sec/deg respectively as can be seen from the Covespagram. Below the Eatonia seismogram the 'beam' or resultant trace from all six stations stacked at  $p = 4.6$  sec/deg is shown.

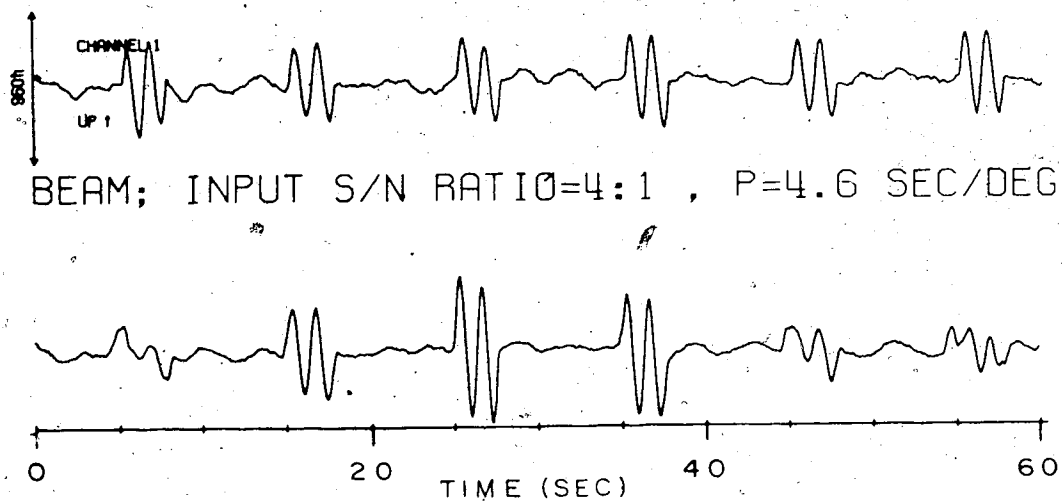
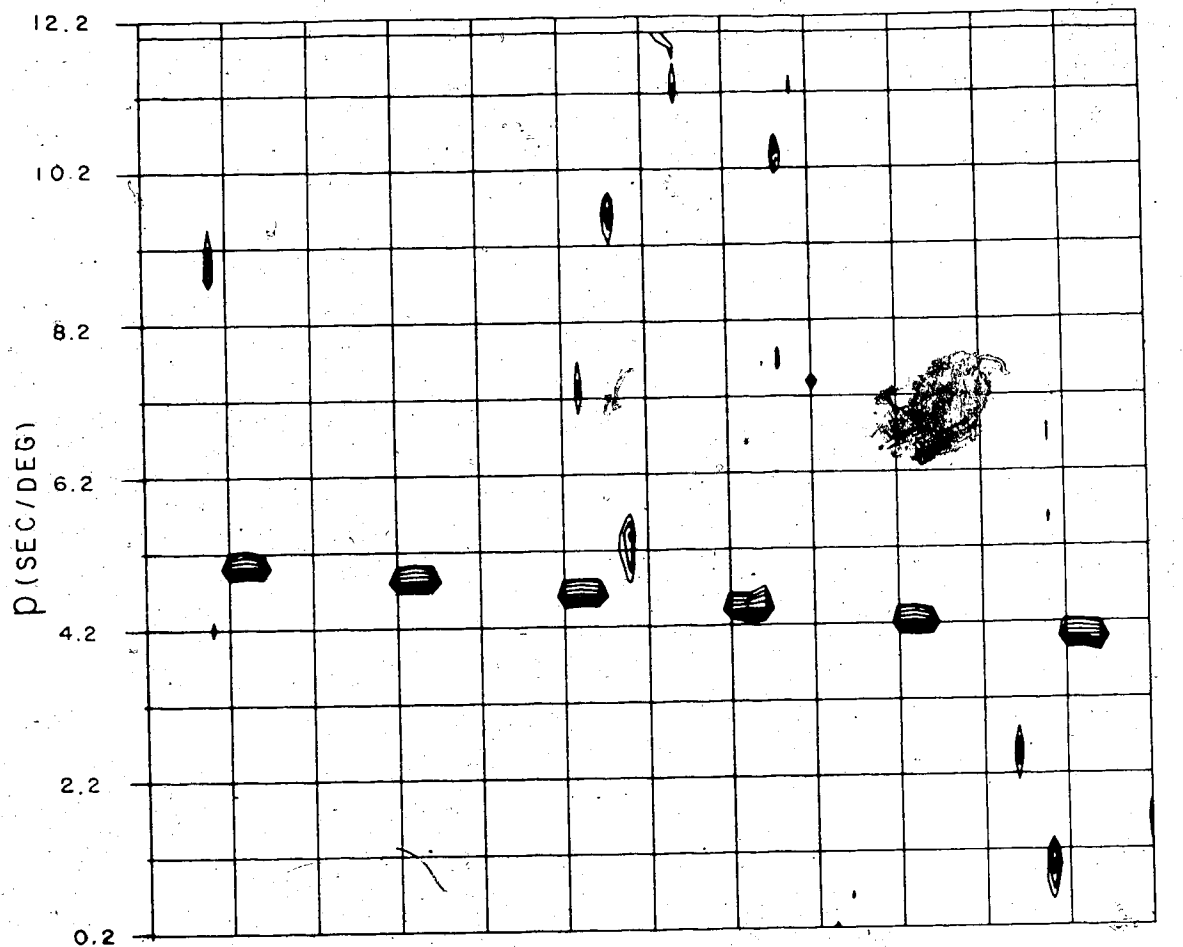
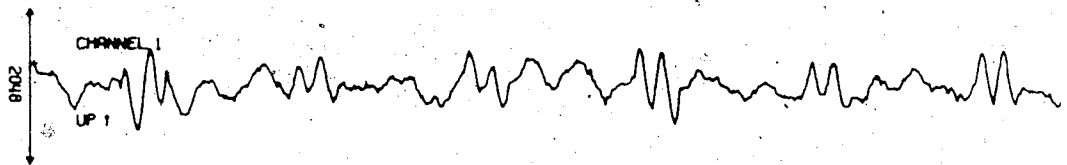
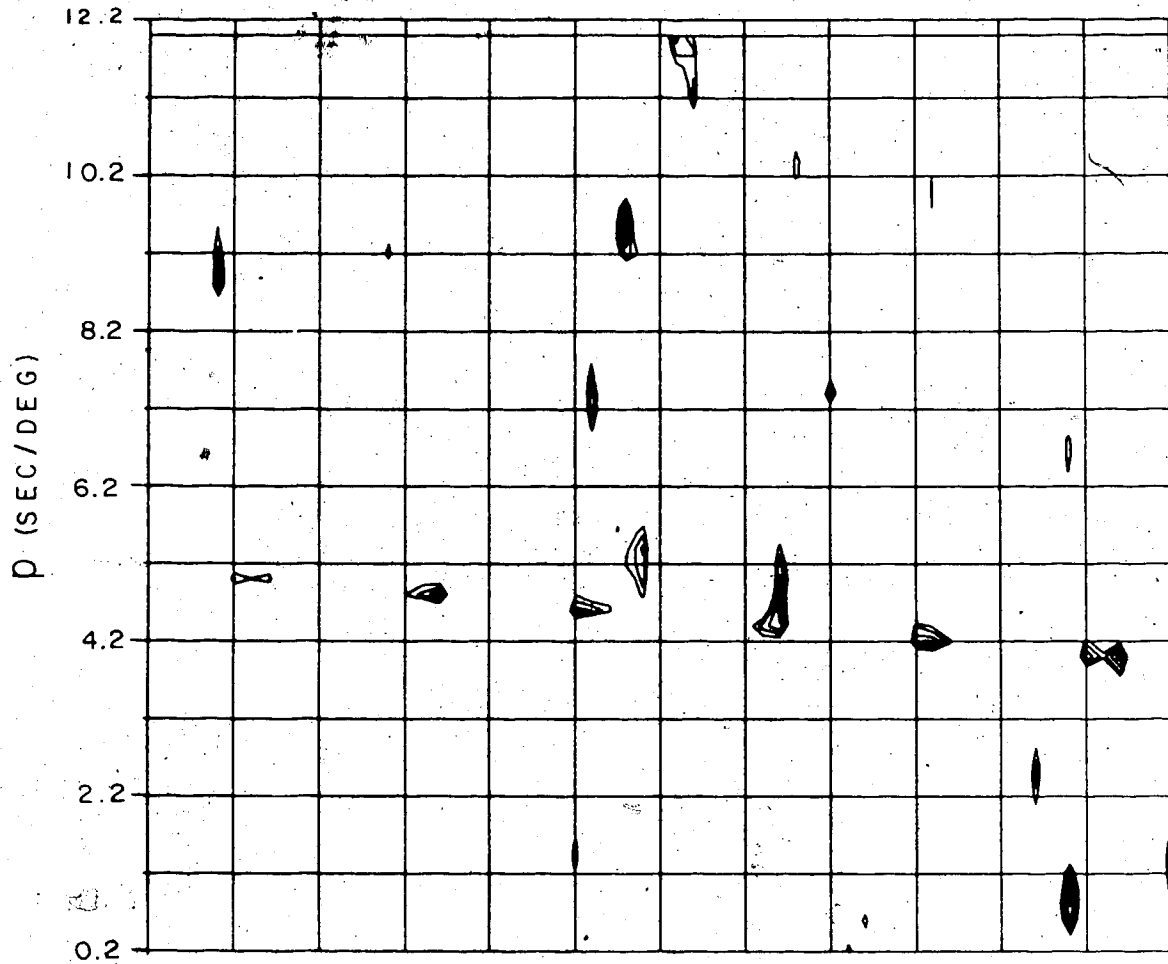


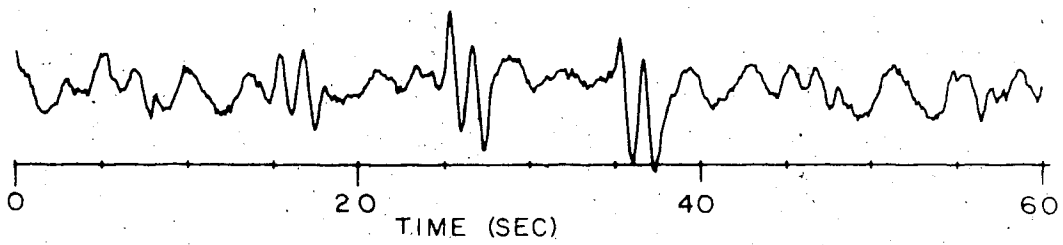
Figure 2.4

Covespagram for six synthetic events traversing the 1974 VASA. Signal to noise amplitude ratio is 1:1. The vertical trace below the Covespagram is the synthetic seismogram at Eatonia. The coherent pulses at 5.0, 15.0, 25.0, 35.0, 45.0, and 55.0 seconds cross the array at slowness values of 5.0, 4.8, 4.6, 4.4, 4.2, and 4.0 sec/deg respectively. Below the Eatonia seismogram the 'beam' or resultant trace from all six stations stacked at  $p = 4.6$  sec/deg is shown.





BEAM; INPUT S/N RATIO=1:1 , P=4.6 SEC/DEG



resolving tool over simple stacking is clearly illustrated in these two diagrams; sole examination of the 'beam' in these figures would lead one to the incorrect conclusion that there is considerable energy arriving at a slowness of 4.6 sec/deg at times other than the true time of 25 seconds. The Covespagrams in figures 2.3 and 2.4 have been calculated assuming the true azimuth of the incoming synthetic waves. Calculations assuming other azimuths reveal that coherency values, for a signal to noise ratio of 4:1 for example, drop from above 0.9 to below 0.5 for the coherent signals when the azimuth deviates from the true azimuth by 2 degrees.

Figures 2.5, 2.6 and 2.7 show the Covespagrams for three events recorded by the 1974 VASA; the vertical traces of various stations have been used as input to the Covespa process. The Covespagram for a Salta Province, Argentina event (figure 2.5) exposes a P wave coda of over 60 seconds duration; similar P wave coda Covespa patterns have been observed by Gutowski (1974). The extended pattern can be interpreted as being the result of a finite time length source pulse convolved with source and receiver structure. Figure 2.6 shows the Covespagram from a Mongolian event as recorded at Eaton, Maple Creek, and Suffield. Notice that the burst at about 9 seconds on the vertical traces is prominent on all stations. The onset of the event however is only clear on the Suffield record at about

Figure 2.5

Covespagram for Salta Province, Argentina event  
( $\Delta = 83^\circ$ , focal depth = 13 km, and magnitude = 5.5)  
as recorded at stations EAT, HAN, and SES. The vertical  
motion seismograms are shown below the Covespagram.

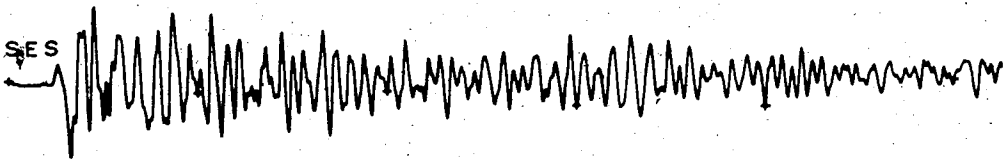
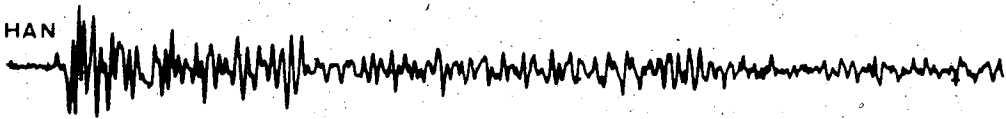
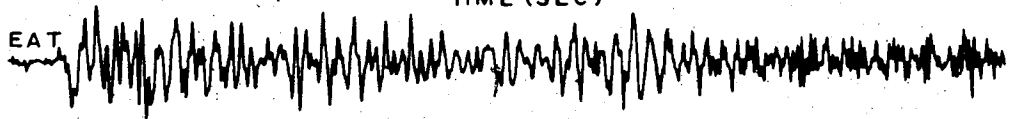
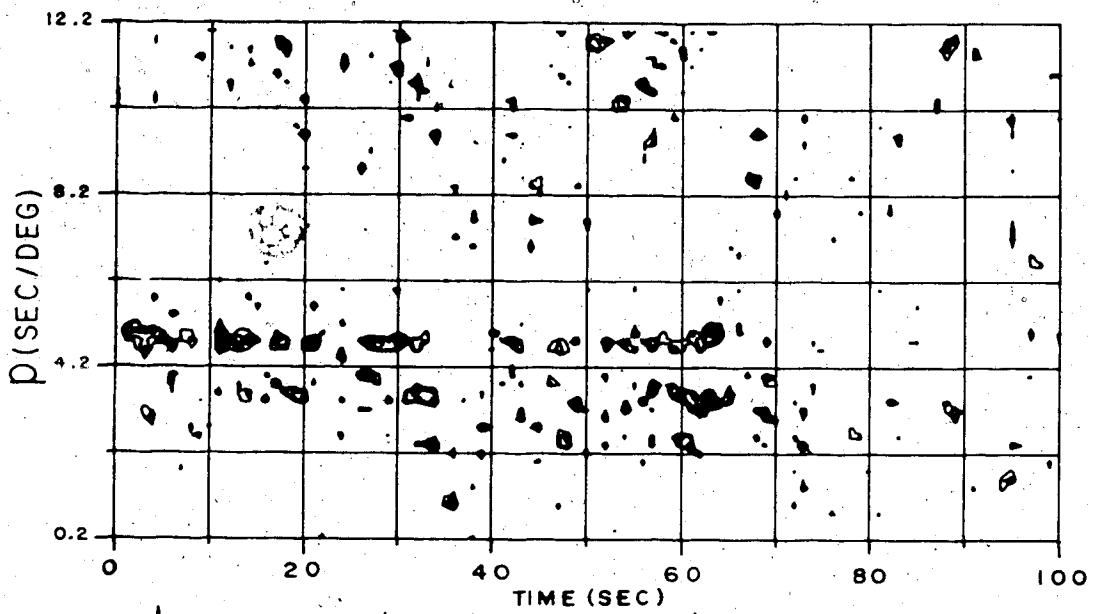


Figure 2.6

Covespagram of event from Mongolia ( $\Delta = 83^\circ$ , focal depth = 33 km, and magnitude = 6.1) as recorded at EAT, MAP, and SES. The vertical motion seismograms are shown below the Covespagram.

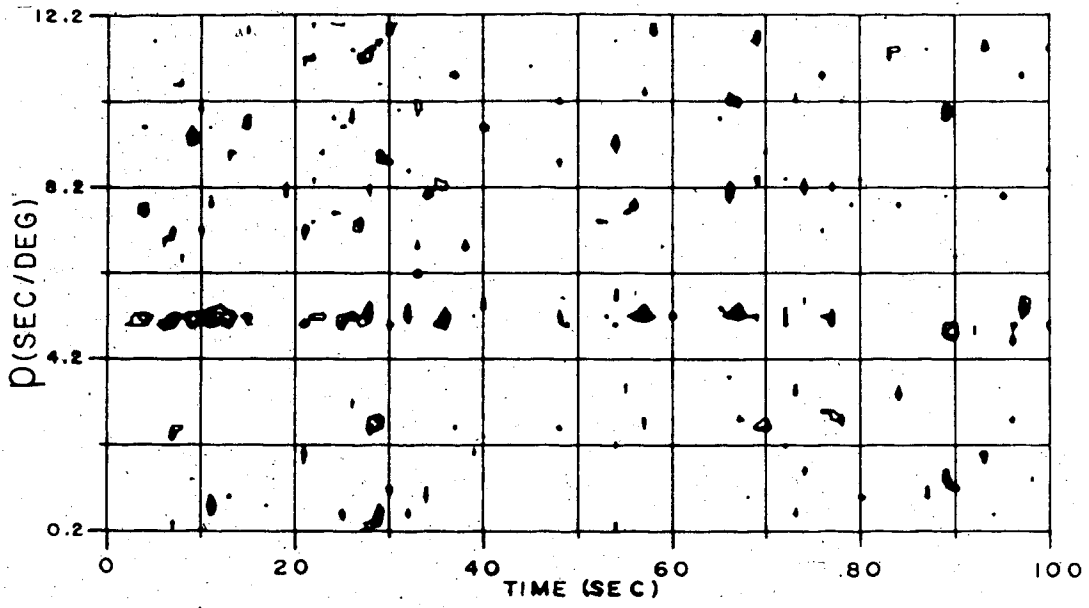
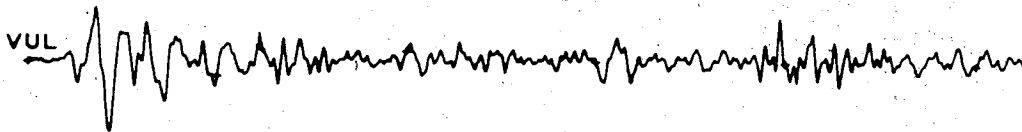
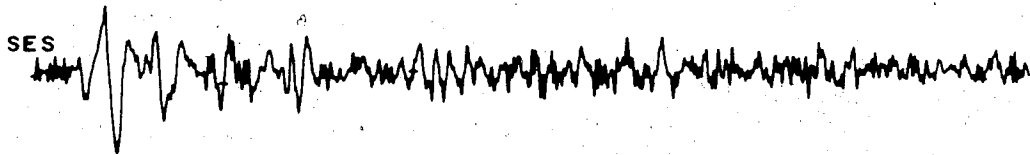
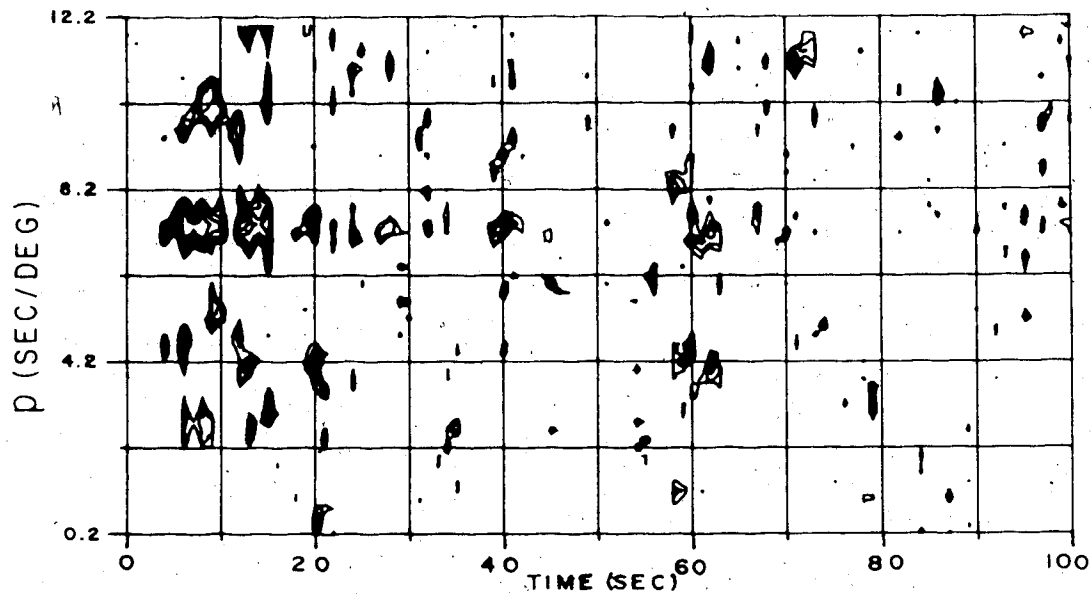


Figure 2.7

Covespagram of event from the Panama-Columbia border ( $\Delta = 51^\circ$ , focal depth = 5 km, and magnitude = 5.4) as recorded at HAN, SES, and VUL. The vertical motion seismograms are shown below the Covespagram.





3 seconds. Nevertheless the Covespa technique does extract the onset as can be seen on the Covespagram. Again the P coda Covespa pattern is extended. The effect of a greater period pulse upon the Covespagram can be seen in figure 2.7 for an event from the Panama-Columbia border. The resulting Covespagram pattern becomes more bulbous as compared to the patterns of the previous examples. It is hoped that these Covespa examples together with those of Gutowski (1974) prove useful to future investigators employing the Covespa technique.

The  $\Delta(p)$ , Slowness-Azimuth and  $\tau(p)$  Planes; Results from 1974 VASA

The 1974 version of VASA recorded teleseismic events (epicentral distance range of  $30^\circ < \Delta < 100^\circ$ ) during June, July, and August 1974. The individual stations were operative during various overlapping periods within these three months. Forty-seven measurements of  $dT/d\Delta$  and azimuth for the P phase were made using various elements of the VASA1 subarray. The various stations of the VASA2 subarray yielded sixty-eight measurements of  $dT/d\Delta$  and azimuth for the P phase. Earth ellipticity and station elevation effects have been removed. Figure 2.8 shows the epicenters of events for which VASA observations of  $dT/d\Delta$  and azimuth were made; almost all




Figure 2.8

The earthquakes for which VASA2 observations of  $dT/d\Delta$  and azimuth were made. The equidistant-azimuthal projection is centered at Hanna. The dashed circles are separated by  $30^\circ$  epicentral distance.



of the epicenters for VASAL observations are included on this figure. The results will be displayed here in the  $\Delta(p)$ , slowness-azimuth and  $\tau(p)$  planes. In all cases the observations will be compared to predictions based upon the assumption that the earth's lower mantle is spherically symmetrical with a velocity depth profile given by the Jeffreys-Bullen standard model.

#### The $\Delta(p)$ plane

The  $\Delta(p)$  plane is of utmost importance in investigations of the earth's lower mantle velocity structure. Depth ranges in the lower mantle for which velocity increases moderately and smoothly with depth are associated with corresponding  $p$  ranges for which  $\Delta$  increases smoothly with decrease in  $p$ . Rapid increases in velocity result in triplications in the  $\Delta(p)$  plane and low velocity zones with sufficient magnitude are reflected by excursions of the  $\Delta(p)$  curve for which  $\Delta \rightarrow \infty$  if the velocity reversal is smooth and for which  $\Delta$  exhibits a finite jump increase if the velocity reversal is sharp. Now the Jeffreys-Bullen velocity model is such that velocity increases moderately and smoothly throughout the entire lower mantle; it is consistent with a chemically homogeneous lower mantle. Departures in the lower mantle velocity profile from that given by Jeffreys and Bullen will have associated  $\Delta(p)$  departures; the relationship

between  $\Delta(p)$  and  $V(z)$  (Gerver and Markushevitch (1967)) will then permit a refinement of the velocity-depth profile. This refinement in turn results in increased resolution of the lower mantle density, pressure, and temperature profiles via equations of state such as the Adams-Williamson relation. These considerations have been of prime importance in many studies. The following studies have revealed anomalous conditions in the lower mantle; in all cases the 'anomalies' are manifested by the presence of large velocity gradients or discontinuities at various depths within the lower mantle. The large gradients are associated with 'offsets' of the  $\Delta(p)$  curve (rapid decreases in  $p$  over small  $\Delta$  ranges) at various epicentral distances.

Gutenberg (1958) suggested regions of depth 900-1000 km and 1400-1500 km as being anomalous from amplitude studies. On measuring P and SH amplitude ratios, Vvedenskaya and Balakina (1959) concluded that there were anomalies at  $\Delta = 38-42^\circ$ ,  $51-53^\circ$ , and  $70^\circ$ . Bugayevskii (1964) pointed to discontinuities in the travel-time distance curve at  $\Delta = 36^\circ-37^\circ$ ,  $51^\circ-53^\circ$ , and  $70^\circ-73^\circ$ . Carder (1964) reported that the travel-time distance curve could be represented as eight near straight line segments for the distance range  $3^\circ < \Delta < 102^\circ$ . He states that the resultant lower mantle step model, with some modification and smoothing, would represent

conditions in the lower mantle more closely than the smooth Bullen model. Similarly Kanamori (1967) fitted the travel-time distance with three straight lines for the distance range  $5^\circ < \Delta < 55^\circ$ . His velocity model has rapid velocity increases at depths of about 150 km and 375 km. Chinnery and Toksoz (1967) studied the  $\Delta(p)$  curve in the distance range  $27^\circ < \Delta < 90^\circ$  using data from Lasa and noticed offsets in the  $\Delta(p)$  curve at  $\Delta = 35^\circ, 53^\circ,$  and  $70^\circ$  which could be correlated with velocity discontinuities at depths of about 800, 1300, and 2000 km. Lasa recordings of  $\Delta(p)$  revealed anomalously high velocity gradients at depths of about 700, 1200, and 1900 km ( $\Delta = 35^\circ, 52^\circ,$  and  $70^\circ$ ) in the study of Toksoz et al (1967); Rayleigh and Love wave dispersion curves yielded shear wave velocity profiles with discontinuities at 350 and 700 km. Hales et al (1968), on the other hand, upon analyzing travel times to North American stations for  $20^\circ < \Delta < 96^\circ$  conclude that there is a discontinuity in the travel time curve at  $\Delta = 24^\circ$  and that there are no other major discontinuities up to  $\Delta = 96^\circ$ . Gopalakrishnan (1969) used  $\Delta(p)$  data for  $25^\circ < \Delta < 95^\circ$  from the Gauribidancer (United Kingdom type) Seismic Array and compared his results with the Jeffreys-Bullen model; he found that his velocity model varied more slowly around  $Z = 750$  km ( $\Delta = 30^\circ$ ) and more rapidly around  $Z = 1200$  km ( $\Delta = 49^\circ$ ). Using measured p.

values from 400 events recorded at LaSa, Chinnery (1969) found regions of anomalous velocity change near 700, 1150, and 2000 km depth associated with anomalous portions in the  $\Delta(p)$  for  $\Delta = 32^\circ-37^\circ$ ,  $\Delta = 46^\circ-48^\circ$ , and  $\Delta = 65^\circ-75^\circ$ . On the basis of spectral amplitudes and travel times Archambeau et al (1969) found that P phases arriving at Western continental U.S. stations were affected by high velocity gradients at depths of 150, 400, 650 and possibly 1000 km. The analysis of Johnson (1969), who used the Tonto Forest array, revealed anomalous  $\Delta(p)$  at  $34.5^\circ$ ,  $40.5^\circ$ ,  $49.5^\circ$ ,  $59.5^\circ$ ,  $70.5^\circ$ , and  $81.5^\circ$  corresponding to increased velocity gradients near depths of 830, 1000, 1230, 1540, 1910, and 2370 km. Wright (1970) using the Warramunga array found regions of anomalously high gradients and also anomalously low gradient regions. Data from the four United Kingdom type arrays were combined by Corbishley (1970) who pointed to anomalous  $dT/d\Delta$  features at  $35-36^\circ$ ,  $48-49^\circ$ ,  $60^\circ$ ,  $68-70^\circ$ , and  $84-85^\circ$  corresponding to possible variations in P-wave velocity gradient near depths of 850-900, 1200, 1550, 1880-1900, and 2500 km respectively. Wu and Allen (1972), using stations of Wesson Observatory, noticed discontinuities in the  $\Delta(p)$  curve at  $52^\circ$ ,  $62^\circ$ , and  $78^\circ$  but they stated that it would be difficult to conclude that these features were related to anomalous velocity gradients at the deepest portions of the ray paths.

Measurements of  $dT/d\Delta$  from the Warramunga array (Wright and Cleary (1972)) revealed fairly low gradients at depths of 800 to 850 km, 1070 to 1110 km, 1260 to 1330 km, 1750 to 1850 km, and 2460 to 2600 km; high velocity gradients were found at depths of 1160 to 1220 km, 2180 to 2370 km, and possibly 2700-2750 km. Vinnik et al (1972) studied  $dT/d\Delta$  measurements at several arrays in the U.S.S.R. and found layers of high P wave velocity gradient near depths of 900, 1300, 1700, 2000, and 2500 km. Hales and Herrin (1972) summarized the results of Chinnery (1969), Kanamori (1967), Johnson (1969), and Corbishley (1970) and emphasized the features which these studies have in common. Wiggins et al (1973) used the  $\Delta(p)$  data of Johnson (1967, 1969) and Wolfe (1969) in conjunction with an extremal type Herglotz-Wiebert inversion; their resulting velocity envelope reveals no fine structure in the mantle below about 600 km depth. Kulhánek and Brown (1974) inferred from UPSAS array data that the velocity distribution shows anomalous variations at depths of 750, 1500, 1800, 2300, and 2500 km.

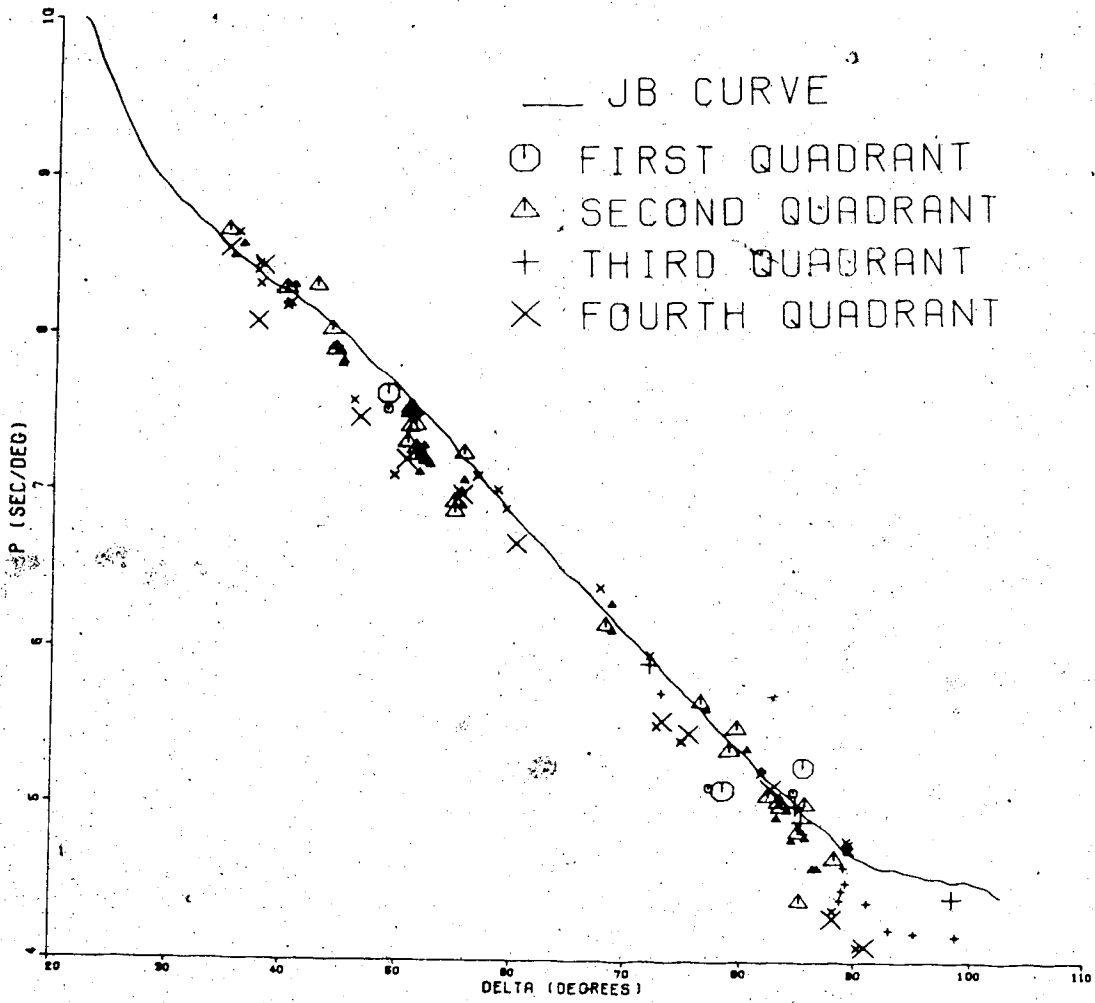
Thus there is much evidence that the P wave velocity profile of the lower mantle does deviate slightly from the smooth Jeffreys-Bullen model. Associated with these small velocity excursions are anomalous perturbations of the  $\Delta(p)$  curve. Also these perturbations are of a global nature since they have been reported



by various authors using different arrays on the surface of the earth. Figure 2.9 shows the  $\Delta(p)$  results from the 1974 VASA. With event locations given by the PDE listings of the USGGS, all observations have been adjusted to a surface focus using the P wave velocity model of Haddon and Bullen (1969); it is felt that their model is ideal for the purpose of focal depth corrections since it is based upon free oscillation data and as such represents a global average. The distance coordinate of each point has been taken to be the distance from the equivalent surface focus to the center of the combination of stations used for the calculation. The empirical solid curve is based upon numerical differentiation of the Jeffreys-Bullen travel-time table for a surface focus; a cubic-spline fit was made to a five average smoothed version of the tables using Fortran subroutine 'ICSICE' which is available in the International Mathematical and Statistical Libraries. In figure 2.9 the small and large symbols correspond to VASA2 and VASA1 subarray observations respectively and the various symbols denote event azimuthal groups as indicated by the legend. Note that simultaneous calculations of slowness and azimuth were made and that the observed slowness is plotted in figure 2.9 even if the measured azimuth may differ from the expected value; nevertheless such a  $\Delta(p)$  plot should reveal 'radial'

Figure 2.9

The 1974 VASA  $\Delta(p)$  observations. The different symbols define 4 azimuthal groups; larger and smaller symbols refer to VASA1 and VASA2 observations respectively. All results have been reduced to surface focus; the solid curve is empirical and based upon numerical differentiation of the Jeffreys-Bullen travel-time tables.



velocity anomalies if they exist. Notice that there is no particular  $\Delta(p)$  signature characteristic of events from any azimuthal group or of determinations from either subarray.

Now it is interesting to compare the 1974 VASA observations with the J-B curve and also with results reported by the various authors mentioned above. In particular let us focus our attention upon the major  $\Delta(p)$  studies (those for which there were many observations over the entire teleseismic range of  $30^\circ < \Delta < 100^\circ$ ). These are the studies of Johnson (1969), Chinnery (1970), Wright (1970), and Corbishley (1970), which collectively cover a global distribution of observations in view of the various arrays used. These studies have exposed anomalously high velocity gradients at various depths and associated offsets in the  $\Delta(p)$  at various epicentral distances; the results are summarized in Table 2.2. The most prominent offsets (those reported by the most authors) occur at distances of about  $\Delta \approx 49^\circ$ ,  $\Delta \approx 60^\circ$ , and  $\Delta \approx 70^\circ$  and correspond to high velocity gradients near depths of about 1200 km, 1550 km, and 1900 km. Now the important question is - do the 1974 VASA  $\Delta(p)$  observations exhibit offsets at the distances agreed upon by most of the authors cited in Table 2.2 (namely at  $\Delta \approx 49^\circ$ ,  $60^\circ$ , and  $70^\circ$ ) and if not, why? Firstly, figure 2.9 reveals anomalously low p values (as compared

Table 2.2

Regions of High Velocity Gradient in the Lower Mantle and Corresponding  
 Epicentral Distances of  $\Delta(p)$  Offsets

| Author            | Array  | Number of Events used   | Depths of High Velocity Gradient (km)                  | Epicentral Distances of $\Delta(p)$ Offsets (degrees)  |
|-------------------|--|-------------------------|--|--|
| Chinnery (1970)   | LASA   | 400                     | 700, 1150, 2000  | 32 to 37,<br>46 to 48,<br>65 to 75                     |
| Johnson (1969)    | Tonto Forest   | 212                     | 830, 1000, 1230,<br>1540, 1910,<br>2370                | 34.5, 40.5, 49.5,<br>59.5, 70.5, 81.5                  |
| Wright (1970)     | Warramunga (WRA)   | 192                     | 1150 to 1260,<br>1540 to 1660,<br>2150 to 2450         | 46 to 49.5,<br>59 to 62,<br>77 to 83                   |
| Corbishley (1970) | Edkdemuir (EKA)<br>Yellowknife (YKA)<br>Gauribidanur (GBA)<br>Warramunga (WRA) | 61<br>145<br>129<br>143 | 850 to 900,<br>1200,<br>1550,<br>1880 to 1900,<br>2500 | 35 to 36,<br>48 to 49,<br>60,<br>68 to 70,<br>84 to 85 |

to the J-B curve) between about  $46^\circ$  and  $55^\circ$  and a sharp decrease in  $p$  values near about  $50^\circ$ . These features are similar to those associated with the  $49^\circ$  offset described by Johnson (1969), Chinnery (1970), Wright (1970), and Corbishley (1970). Hence, anomalously high velocity gradients near about 1200 km depth have possibly been detected by the 1974 VASA. Secondly, no statement can be made regarding possible anomalous conditions near 1550 km depth in view of the absence of data points between  $60^\circ$  and  $68^\circ$ . Thirdly, it is inviting to associate the low  $p$  values in the distance range of about  $72^\circ \leq \Delta \leq 76^\circ$  with a  $p$  offset near  $70^\circ$  caused by anomalously high velocity gradients near 1900 km depth but the low density of observations in this distance range renders conclusions based upon the correlation rather weak.

The 1974 VASA  $\Delta(p)$  points describe a region of anomalously low  $p$  values in the distance range of about  $85^\circ \leq \Delta \leq 99^\circ$  where observed slownesses are as low as 4.1 sec/deg. The J-B curve tapers off to a [redacted] of about 4.4 sec/deg beyond  $90^\circ$  and observations of the four authors mentioned above are in accordance with the J-B model. Thus if the anomalously low  $p$  values observed here in fact reflect anomalous velocity changes near the maximum depth of penetration of the associated rays (from a depth of about 2600 km to the core-mantle

boundary) then the anomalous velocities are certainly not a global phenomenon. Slowness values below 4.4 sec/deg have also been observed by Kanasewich et al (1973) for rays which have their turning points in the vicinity of the core under Hawaii, by Hales et al (1968), and also by Davies and Sheppard (1972). The low  $p$  values observed here are associated with rays that bottom near the core under Hawaii and also near the core under other locations in the Pacific Ocean (these locations will be shown in the next section). The low  $p$  values for  $\Delta > 85^\circ$  could be produced by anomalously high velocities near the core mantle boundary; the increase in velocity needed to account for the  $\Delta(p)$  observations depends upon the lateral extent of the anomaly (Green (1975)). It should be pointed out however that both Kanasewich and Gutowski (1975) and Green (1975) report that low  $p$  values for  $\Delta > 85^\circ$  associated with near core rays arriving at such arrays as VASA and LASA from the west could be produced by anomalous Rocky Mountain upper mantle velocity distributions. Note also that Johnson (1969) has pointed out that the effect of the core should be considered when measurements of  $dT/d\Delta$  are made for the P phase for  $\Delta > 90^\circ$ . This core effect only becomes significant when the difference between arrival times of the P and  $P_c$  phases is small compared to the period of the P phase energy.

The observed period of the 1974 VASA events for the distance range in question is about 1 sec and the J-B travel-time tables predict P-P<sub>c</sub>P travel-time differences greater than 0.8 sec for distances as great as 94°; hence few points will be effected by the core. Also since the core correction when applied to the data of Johnson (1969) never exceeded about 0.08 sec/deg, it is felt that such a core correction would not significantly alter the 1974 VASA  $\Delta(p)$  observations.

A final question regarding the four major  $\Delta(p)$  studies cited and the  $\Delta(p)$  observations presented here remains. Although there is some agreement as to the location and nature of anomalies in the  $\Delta(p)$  plane, why is there not total agreement? The answer to this question is multifold. The entire teleseismic distance range is not well sampled - the density of observations as a function of epicentral distance varies from study to study. The degree of scatter of  $\Delta(p)$  points about some average line is not the same for all studies and it is expected that purely radial velocity anomalies would be defined better by  $\Delta(p)$  data sets with small scatter. The final and most important reason for the disparity is that a spherically symmetric velocity distribution is not an adequate description of actual conditions within the earth's mantle. Thus the results from each study are applicable to distinct regions within the earth defined



by the paths of rays between event epicenters and the array used and are not necessarily indicative of global conditions. Furthermore rays may suffer lateral displacements due to anomalous lateral velocity gradients in the course of their journey from source to receiver. In accordance later array studies of the 1970's included measurements of azimuth as well as slowness. The following section highlights the major results of these studies and includes a presentation and interpretation of the 1974 VASA observations in the slowness-azimuth plane. Still it is hoped that the radial velocity anomalies revealed by the  $\Delta(p)$  analyses mentioned are not viewed with extreme pessimism since they have been reported by many authors who collectively have studied a large portion of the earth.

#### The Slowness-Azimuth Plane

Figures 2.10 and 2.11 show the slowness-azimuth results for the 1974 VASA1 and VASA2 subarrays respectively. In these figures there is one arrow for each seismic event with the tail of each arrow representing the slowness and azimuth predicted by the J-B tables for a ray originating at the USCGS location and arriving at Suffield (for the VASA1 observations) and Hanna (for the VASA2 observations). The head of each arrow represents the observed slowness and azimuth. The

Figure 2.10

Slowness-azimuth 'array diagram' for the 1974 VASA1 observations. The solid circles represent constant slowness values as indicated. The inner dashed circle represents the lowest possible J-B slowness for the P phase (4.4 sec/deg). Each arrow represents one seismic event with the tail and head being at the expected and observed locations respectively. The projection is centered at the Suffield station.

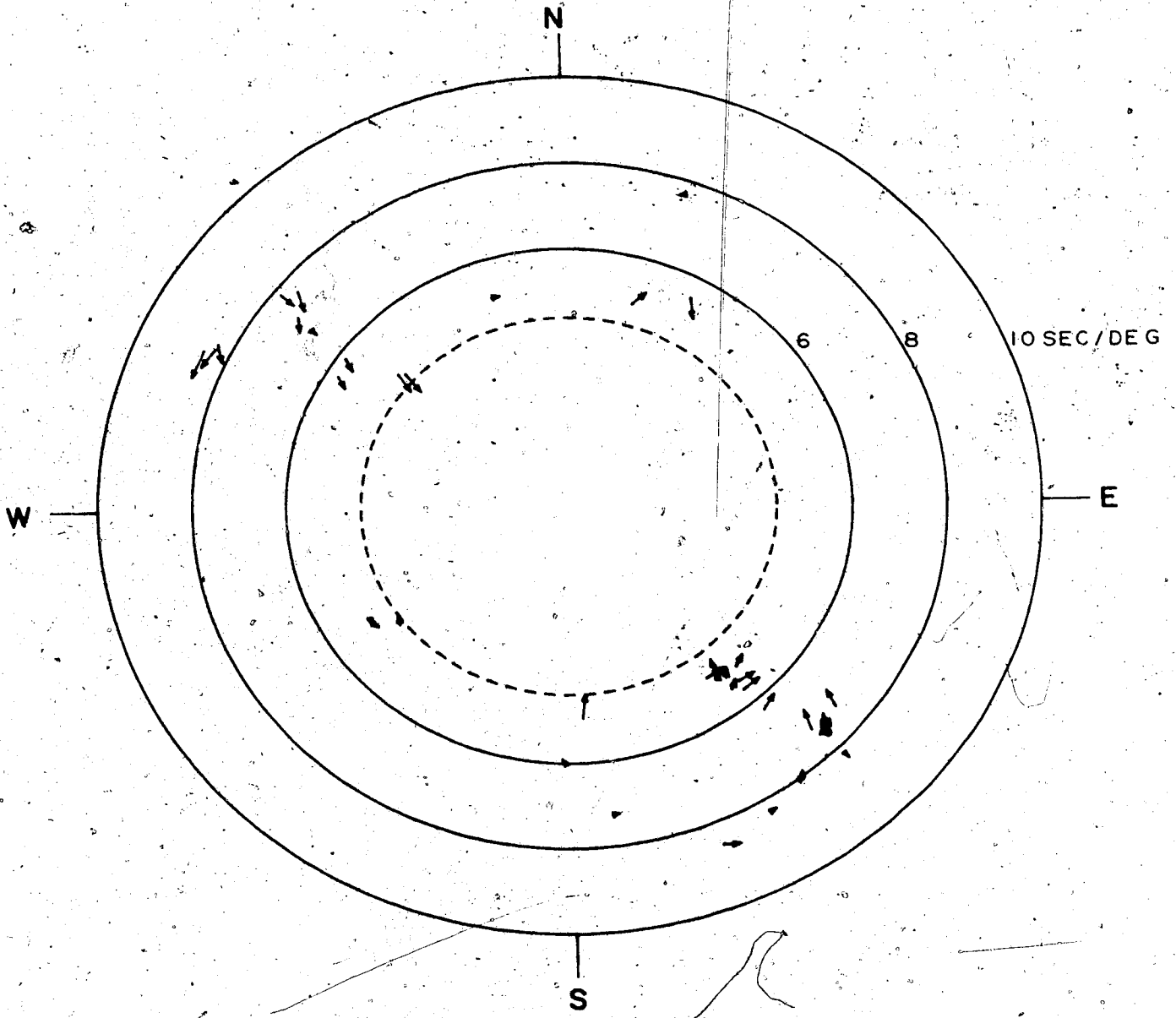
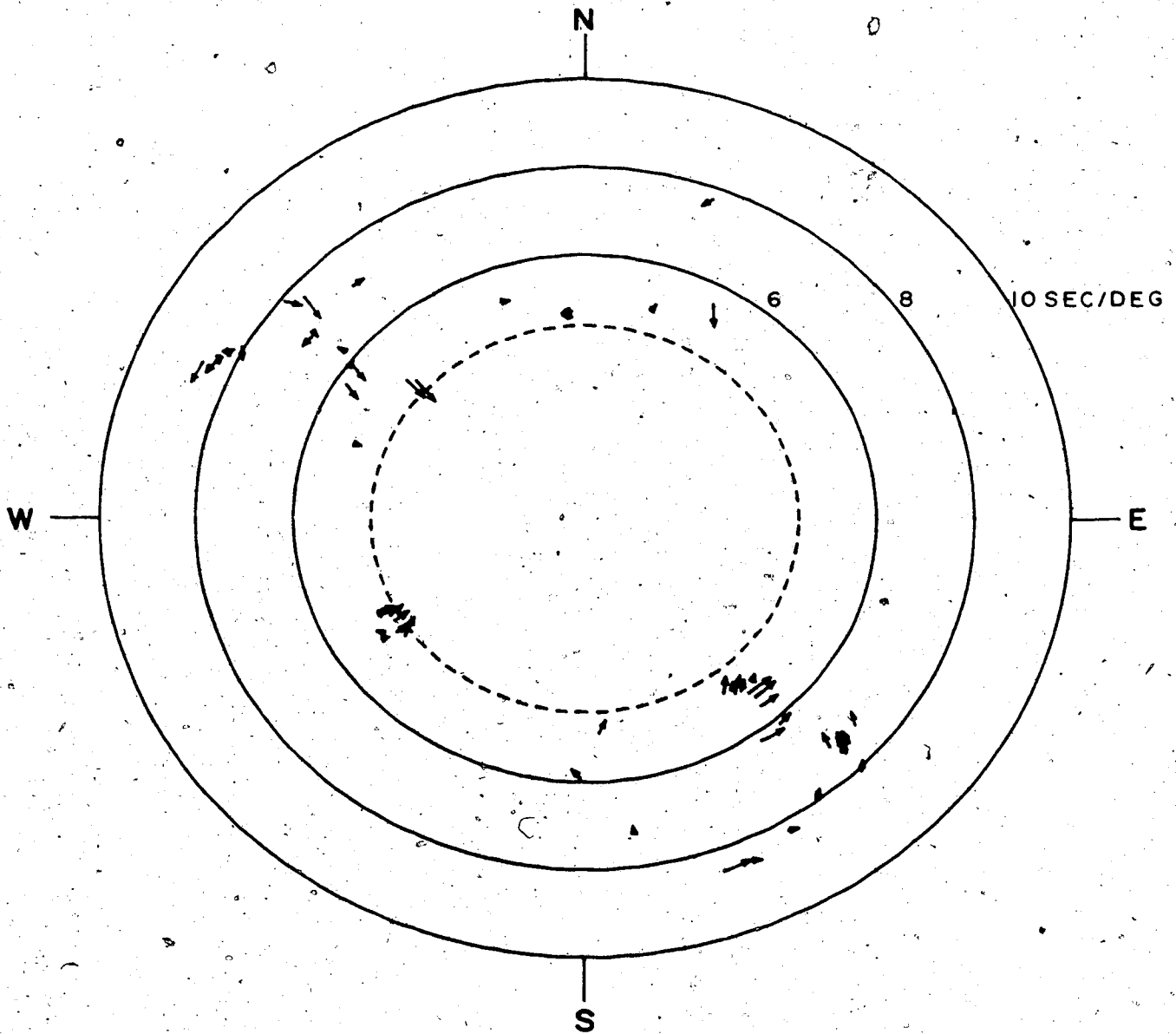


Figure 2.11

Slowness-azimuth 'array diagram' for the 1974 VASA2 observations. The solid circles represent constant slowness values as indicated. The inner dashed circle represents the lowest possible J-B slowness for the P phase (4.4 sec/deg). Each arrow represents one seismic event with the tail and head being at the expected and observed locations respectively. The projection is centered at the Hanna station.



length of the arrows are quite substantial (the average length for the VASAL subarray is about 0.31 sec/deg) and hence the immediate problem which arises is the identification of sources of the mislocations. The path of a P ray may be perturbed by anomalous velocity conditions near the source, the deepest portions of the ray path, and near the crustal and upper mantle region beneath the array. Generally it is accepted that the source region is the least likely cause of slowness and azimuth perturbations since the cone of rays which crosses an array, when traced back to a teleseismic source, is very narrow. Note however that source effects cannot be entirely ruled out (Davies and Sheppard (1972), for example). Past investigations of similar data have led to divided opinions as to the location of velocity anomalies which cause unexpected observed values of the vector ray parameter  $p$  (recall from Chapter 1 that a slowness and azimuth calculation is equivalent to a measurement of a 2 element vector ray parameter). Authors who have associated deep anomaly sources with teleseismic  $p$  deviations recorded at various arrays include Manchee and Weichert (1968) - Yellowknife array (YKA), Davies and Sheppard (1972) - LASA, Weichert (1972) - YKA, Kanasevich et al (1973) - VASA, Powell (1975) - Hanford array, and Wright and Lyons (1975) - YKA. On the other hand, vector ray parameter mislocations have been

attributed mostly to lateral inhomogeneities in the crust and upper mantle beneath arrays by Otsuka (1966a) - California array, Iyer (1971) - LASA, Naponen (1974) - Norsar, Hagfors, and Helsinki arrays, Wright et al (1974) - Warramunga array (WRA), Capon (1974) - LASA, Okal and Kuster (1975) - Tahiti and Rangiroa arrays, and Berteussen (1976) - NORSAR. Brown (1973) attributed  $p$  dislocations shown by the Uppsala array to both receiver and deep mantle effects. Also Engdahl and Felix (1971) and Aki et al (1976) have attributed anomalies in absolute travel time of various body wave phases arriving at LASA from teleseismic events to lateral inhomogeneities in the crust and upper mantle under Montana. Julian and Sengupta (1973) and Sengupta and Toksoz (1976) studied body wave phase times on a world-wide basis and concluded that unexpected results could be attributed to lateral inhomogeneities within the top 500 km and also within a region extending from a depth of about 2600 km to the core-mantle boundary.

Thus from the above results it can be seen that caution should be exercised in the interpretation of 'array' diagrams such as those shown in figures 2.10 and 2.11. There are features other than the effects of velocity structure which give rise to unexpected values of  $p$ . Otsuka (1966) shows that the assumption of a plane wavefront with constant velocity introduces maximum

'errors' in time of about 0.2 sec for the case of actual teleseismic P phases impinging upon a  $2^\circ$  aperture array. Similarly it can be shown that the above assumptions introduce an error  $\delta p$  such that  $||\delta p|| \approx 0.1$  sec/deg for this experiment. Next it can be assumed that the errors in epicentral location given by the USCGS can be ignored (see Otsuka (1966) and Davies and Sheppard (1972) for example). Similarly the assumption that the Suffield and Hanna sites identify the 'center' of the array for VASA1 and VASA2 ~~observed~~ respectively introduces a negligible error. Also, as has been mentioned, earth ellipticity and elevation corrections have been applied. The sampling interval of the vertical motion is 80 ms and it has been pointed out that a cross correlation technique provides time resolution of about 20 ms. A generous estimate of the combined effects of the finite sampling rate and the Covespa process is about 0.03 sec/deg for the combinations of stations used in this study. The value 0.1 sec/deg represents a maximum constant velocity-plane wave error and generally the error is substantially less than this; thus considering the intrinsic time resolution and calculation factors, it can be concluded that a realistic estimate of errors due to non-structural sources is  $||\delta p|| = 0.1$  sec.

Now let  $p_E$  be the expected vector ray parameter,  $p_{obs}$  the observed value, and define  $\delta p_{obs}$  by  $\delta p_{obs} =$



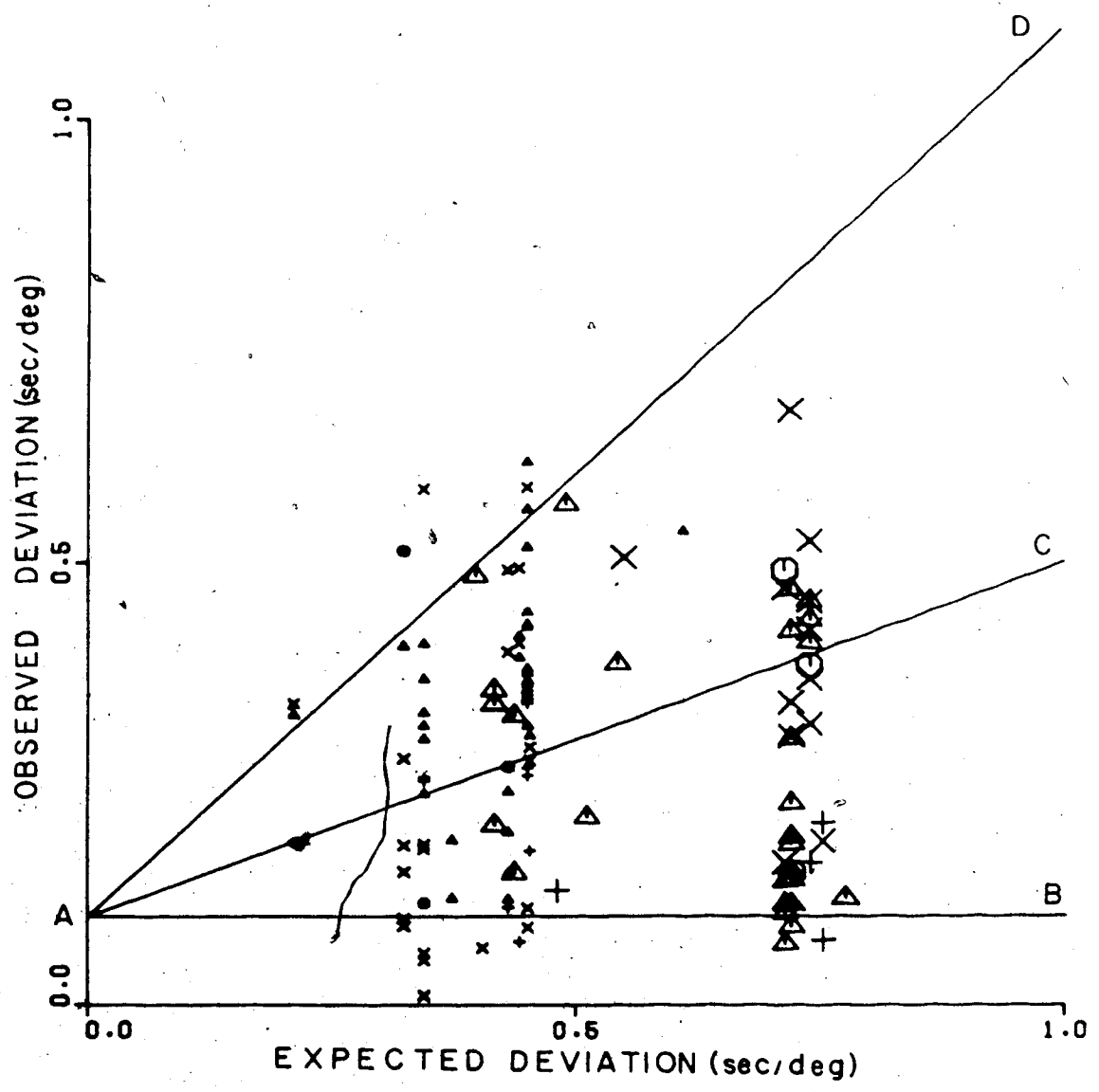
$p_E - p_{obs}$ . As can be seen from figures 2.10 and 2.11 the value  $||\delta p_{obs}||$  is very often substantially greater than 0.1 sec/deg; thus anomalous velocity structures have affected the 1974 VASA observations. In an attempt to delineate the velocity deviations responsible for the large values of  $||\delta p_{obs}||$  it is necessary to consider the possibility of a 'deterministic' near receiver effect. The effect of dipping interfaces under an array upon slowness and azimuth calculations has been discussed by Niazi (1966), Manchee and Weichert (1968), and Zengeni (1970). Basically a displacement,  $\delta p_{crust}$  which is approximately constant, is introduced; thus all observations of  $p$  would contain a common component  $\delta p_{crust}$  if a series of dipping interfaces defined the crustal structure under an array. In particular if there is only one dipping interface, such as the Moho say, the vector  $\delta p_{crust}$  is simply related to the strike and dip of the marker (Manchee and Weichert (1968)). Accordingly Capon (1974) has averaged the individual orthogonal components (North-South and East-West) of  $p$  observations recorded at LASA to determine the quantity  $\delta p_{crust}$ ; he then attributes this constant component to near receiver deterministic structure and bases further interpretations of velocity anomalies upon a new  $p$  data set from which the bias has been removed. Such a calculation shows that  $\delta p_{crust}$  has magnitudes of 0.08 sec/deg and 0.15 sec/deg

for the VASAL and VASA2 observations respectively. If a dipping Moho under VASA is responsible, then if the average crustal velocity is taken to be 6.5 km/sec and the Moho velocity is 8 km/sec the discontinuity has about 1° and 2° of dip under the VASAL and VASA2 subarrays respectively. In both cases the direction of dip is to the north-east. It is felt however that the 1974 VASA p data set does not constitute a sufficient azimuthal sampling for such an analysis to be reliable and thus the observed 'bias' has not been removed. Results are given above to facilitate comparison with future studies.

It is reasonable to describe the lengths and directions of the arrows in figures 2.10 and 2.11 as being random in nature (casual inspection will verify this). For each event deviations of the travel time,  $\delta t$ , at each station from the expected value give rise to the finite length arrows. The departures in travel time are in turn due to deviations of the velocity distribution from the standard spherically symmetrical J-B model. Now the slowness and azimuth of each event were determined using a particular combination of stations. Thus, in accordance with the results of Chapter 1, for each p calculation there will be associated expected deviations  $\delta p$  which depend upon the size of the travel-time perturbations,  $\delta t$ , and the combination of stations used. Figure 2.12 illustrates this relationship; the abscissa is scaled such that

Figure 2.12

Diagram showing the 'size' of the departures of 1974 VASA slowness-azimuth measurements from quantities which would be predicted from the listed location and a J-B earth model. Each symbol represents one seismic event with the various symbols defining azimuthal groups and large and small symbols referring to VASA1 and VASA2 observations respectively (see figure 2.9). The observed deviation is given by the arrow lengths in figures 2.10 and 2.11. The expected deviation is the average 'error'  $\delta p_A$  (see Chapter 1) for random travel-time errors of 0.5 sec. Dislocations attributable to only non-structural sources have associated points which fall below line AB. Lines AC and AD define expected deviations associated with random travel-time deviations due to structural effects of 0.2 and 0.5 sec respectively with allowance for non-structural effects.



it refers to the 'average' or expected error  $\delta p_A$  (see Chapter 1) for random deviations in travel time of 0.5 sec, the ordinate gives the lengths of the arrows in figures 2.10 and 2.11 (that is the value  $||\delta p_{\text{obs}}||$ ), and the points are plotted with the same convention as that for figure 2.9 (the various symbols refer to different azimuths of ray approach and large and small symbols refer to VASA1 and VASA2 observations respectively). The line AB is drawn (parallel to the expected deviation axis and intersecting the observed deviation axis at 0.1 sec/deg) to represent the upper limit of contributions due to non-structural sources. Thus, the deviation depicted by any point in figure 2.12 which falls below the line AB cannot be attributed to anomalous velocity conditions. The line AC is drawn such that departures depicted by points which fall within the region between lines AB and AC can be attributed to random travel-time deviations of about 0.2 sec arising from anomalous velocity structure. Similarly the line AD is an upper bound for deviations due to structurally related travel-time departures of about 0.5 sec. The bounds given by lines AC and AD and the values of 0.2 sec and 0.5 sec associated with them are not intended to be 'sharp'; if an observation involving N stations has associated unexpected travel-time departures due to velocity structure at the stations given by  $\delta t_i$ ,  $i = 1, \dots, N$ , then if

$(\Sigma \delta t_i^2 / N)^{1/2} = 0.2$  sec the ordinate of the line AC depicts the expected departure  $\delta p_A$  (see Chapter 1), which then depends upon the configuration of stations used, plus the constant maximum non-structural factor of  $0.1 \text{ sec} \chi / \text{deg}$ .

Similarly if  $(\Sigma \delta t_i^2 / N)^{1/2} = 0.5$  sec then the ordinate of the line AD depicts  $\delta p_A$  plus the constant factor  $0.1 \text{ sec/deg}$ .

Recall from Chapter 1 that observational deviations given by the form  $(\Sigma \delta t_i^2 / N)^{1/2}$  generally result in departures  $\delta p$  which describe ellipses. The average quantity  $\delta p_A$  is considered here since the combinations of stations used were 'nearly' symmetrical and there was no one combination employed a sufficient number of times such that an 'elliptical' analysis would be much more appropriate. Notice also that figure 2.12 is based upon a least-squares type computation of slowness and azimuth whereas the 1974 VASA observations result from Covespa computations. This computational disparity is not serious since a 'Covespa plane wave' will closely approximate a best fit least squares plane wave. It is felt that the presentation of figure 2.12 is a reliable and useful interpretational aid.

Now let us consider the effect that near receiver structure can have upon the results shown in figures 2.10, 2.11, and 2.12. If we take some typical P wave crustal and upper mantle model, that of Massé (1973) say, then it is possible to determine the perturbation of

near vertical P wave travel times resulting from lateral changes in velocity beneath an array (the significance of the Massé (1972) model here is no more than that it is typical of models associated with stable continental regions and if any other model were chosen then very similar results would be obtained). Ten km undulations of the Conrad, Moho, top and bottom of the asthenospheric low velocity zone, and the 430 Km discontinuities produce travel-time deviations of about 0.20, 0.17, 0.02, 0.07, and 0.10 sec respectively. Alternatively one could express lateral structural changes in terms of percent deviations. Thus, again using the Massé (1973) model as a basis, a 3% change in P wave velocity from the surface to a depth of 150 km produces travel-time changes of about 0.55 sec. If the magnitude of lateral velocity changes under VASA is as described above then from figure 2.12 it can be seen that the 1974 VASA p observations would be a poor indication of possible deep anomalies. It is unlikely however that near receiver structure is completely responsible for all of the observed anomalies. Firstly from figures 2.10 and 2.11 it can be seen that the pattern of anomalies given by the distribution of arrows for the VASA1 and VASA2 sub-arrays are strikingly similar - if near receiver structure was responsible for this pattern then the inhomogeneities underlying VASA1 and VASA2 would have to be nearly

identical and this is highly unlikely. Secondly there are regions in the slowness-azimuth diagrams where the arrow directions and magnitudes change rapidly for small changes in epicentral location - this phenomenon is associated with velocity anomalies at deep portions of ray paths (Davies and Sheppard (1972)). Thirdly the extended Covespagram patterns shown in the previous section are typical of the 1974 VASA data and indicate that the velocity structure beneath individual stations is relatively uniform.

A generous assignment of travel-time deviations due to near receiver structure would be about 0.2 sec. In this case the points in figure 2.12 which lie above line AC are caused by deep anomalous conditions. Generally the slowness and azimuth of a given ray are most sensitive to anomalous velocity gradients, both lateral and vertical, near the deepest point of penetration. If we assume that observations for which values of  $||\delta p_{\text{Obs}}||$  fall above line AC reflect conditions near the associated ray bottoming points then several interesting statements can be made. The 'deep anomalies' then are associated with four major categories of  $\delta p_{\text{Obs}}$ :

(i) Low slowness observations near an epicentral distance of about  $50^\circ$ . Here  $\delta p_{\text{Obs}}$  is largely radial in nature and points 'inward' on the array diagrams; the arrows associated with these anomalies shown in figures



2.10 and 2.11 have their tails between about 7.5 and 7.8 sec/deg. This category has been discussed in the previous section where it was stated that the low slowness values could be associated with rapid increases in velocity gradient near about 1200 km depth.

(ii) Low slowness values for some particular rays which bottom near the core-mantle boundary. In figure 2.10 (VASA1) the arrows associated with these rays have their tails at slowness values less than 4.8 sec/deg at azimuths of about 177° and 310°. In figure 2.11 (VASA2) the arrows have their tails at slowness values less than 4.8 sec/deg at azimuths of about 177°, 310°, and 240°. Again the anomalous arrows are mostly radial in nature and point inward. Notice that the group of VASA2 arrows at an azimuth of about 240° and between slownesses of about 4.4 to 5.0 sec/deg do not all conform; that is, some point radially inward while others depict near normal conditions. The bottoming points for the associated rays have surface projections near Hawaii and Kanasewich and Gutowski (1974) have noticed a similar complex anomalous pattern associated with this region. It has been pointed out that one cannot conclude that these types of  $\delta p_{\text{Obs}}$  observations prove the existence of lateral inhomogeneities near the core-mantle boundary, especially when they are based upon rays arriving at VASA from the west. Notice, however, that this phenomenon

is also observed for rays approaching VASA at an azimuth of about  $177^\circ$ .

(iii) A complex pattern of rapidly changing vectors  $\delta p_{\text{Obs}}$  with a dominance of  $\delta p_{\text{Obs}}$  vectors showing large azimuthal anomalies is the state which describes a series of observations centered at an azimuth of about  $138^\circ$  and between slowness values of about 4.9 to 6.2 sec/deg. This pattern which is similar for VASA1 and VASA2 can be seen in figures 2.10 and 2.11. The rays associated with this group bottom in a region between depths of about 1900 to 2600 km which has a surface projection near the Caribbean. It is interesting that in a study of seismic body wave phases recorded by the Yellowknife array, Wright and Lyons (1975) noticed rapidly changing azimuthal anomalies (from  $-4.3^\circ$  to  $+1.4^\circ$ ) associated with rays bottoming below a depth of 2600 km under the Caribbean - they postulated the existence of strong lateral velocity gradients in the deep mantle under the Caribbean. Also, on the basis of travel-time residuals, Jordan and Lynn (1974) showed that anomalously high velocities exist in at least part of the depth range between 600 and 1400 km (and possibly deeper) under the Caribbean. The regions in question sampled by Wright and Lyons (1975), Jordan and Lynn (1974), and this study are all mutually disjoint but the results do suggest that the entire lower mantle below

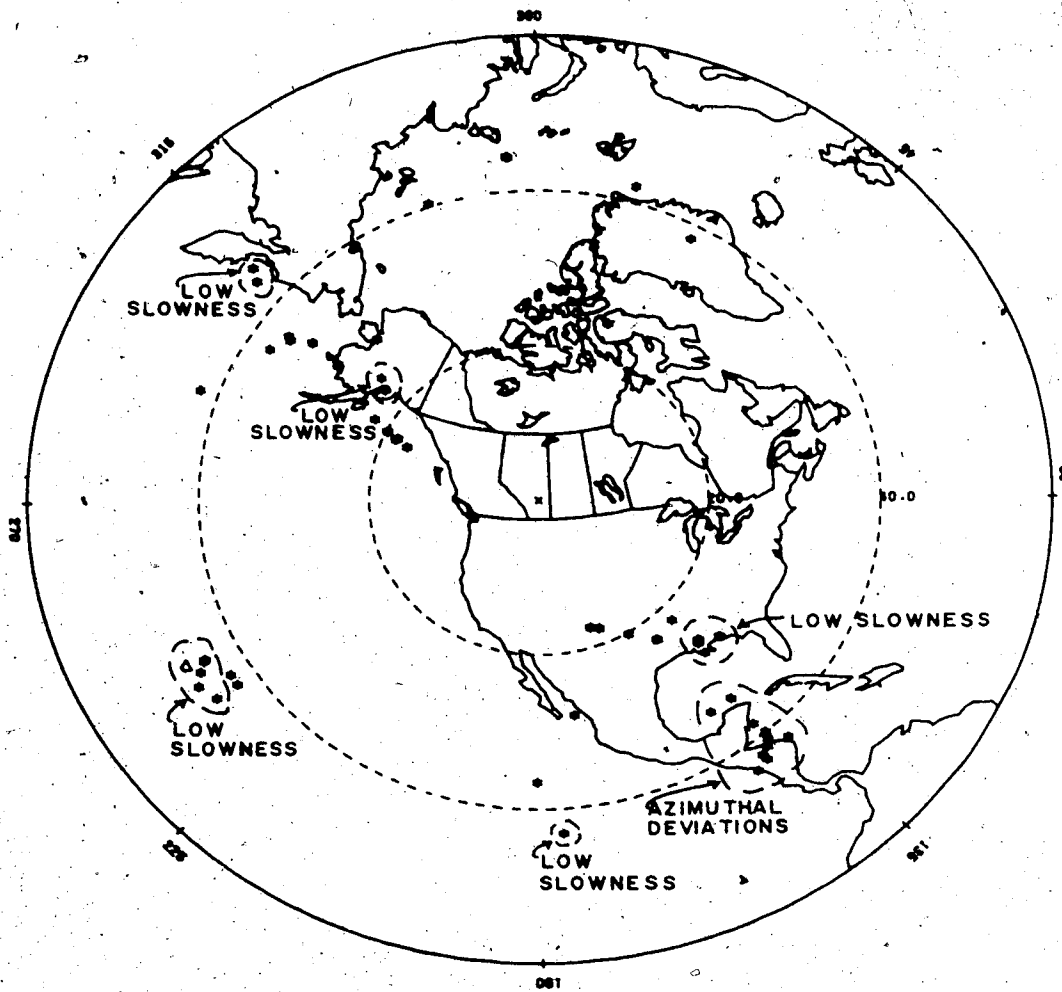
the Caribbean and adjacent areas is in an anomalous state.

(iv) Other spurious  $\delta p_{\text{obs}}$  observations. This category includes the observations for which  $||\delta p_{\text{obs}}||$  falls above line AC in figure 2.12 other than those which fall in the above categories (i), (ii), and (iii). In general these observations constitute a low density sampling for any one region and they are scattered in the array diagrams. It is difficult to make comparisons of these 'anomalies' with those revealed by other studies because of their spurious nature.

Figure 2.13 is an azimuthal great circle projection centered at the Hanna station; the symbols in this figure depict the surface projection of the points of deepest penetration of rays for which VASA2 determinations of  $p$  were made. The general descriptions of  $\delta p_{\text{obs}}$  refer to rays associated with bottoming points enclosed by the nearby boundaries and are based upon the observations of categories (i), (ii) and (iii) above. VASA2 mid-points are shown but the comments apply to the total array. Note that it is not necessarily intended that the anomalous observations are due to velocity structure near these points since, as has been mentioned, if near receiver lateral inhomogeneities are severe then no such claim can be made. Nevertheless, in view of the

Figure 2.13

Equidistant-azimuthal projection centered at Hanna showing the surface projections of the bottoming points of rays for which VASA2 slowness and azimuth measurements were made. The comments describe the nature of slowness-azimuth deviations associated with these rays and are based upon the VASA1 and VASA2 observations taken collectively.



fact that the interpretation of slowness and azimuth anomalies in terms of deep velocity structure is in accordance with results from many other studies it is felt that it should be considered as a serious possibility. The VASA array is still in the infant stages compared to other arrays (LASA for example) and it is hoped that possible future VASA studies will provide detailed information regarding the near receiver structure thereby rendering the results presented here more meaningful. Techniques described by Aki et al (1976) and Capon (1974) and the inherent mobility of VASA are encouraging indications that this goal can be attained.

#### The $\tau(p)$ Plane

It has been stated that an exact interpretation of the  $p$  observations shown in figures 2.10 and 2.11 is not possible at this stage. Still it is worthwhile to consider the 1974 VASA observations in yet another plane - the  $\tau(p)$  vs  $p$  plane. Recently the importance of the function  $\tau(p) = \frac{T(p)}{2} - p \frac{\Delta(p)}{2}$ , where  $T$  is travel time, and its relationship to spherically symmetrical velocity depth profiles have been demonstrated by Bessonova et al (1974), Kennet (1976), and Bessonova et al (1976). By introducing the parameter of absolute time,  $T(p)$ , into the previously discussed 1974 VASA  $p$  observations a new

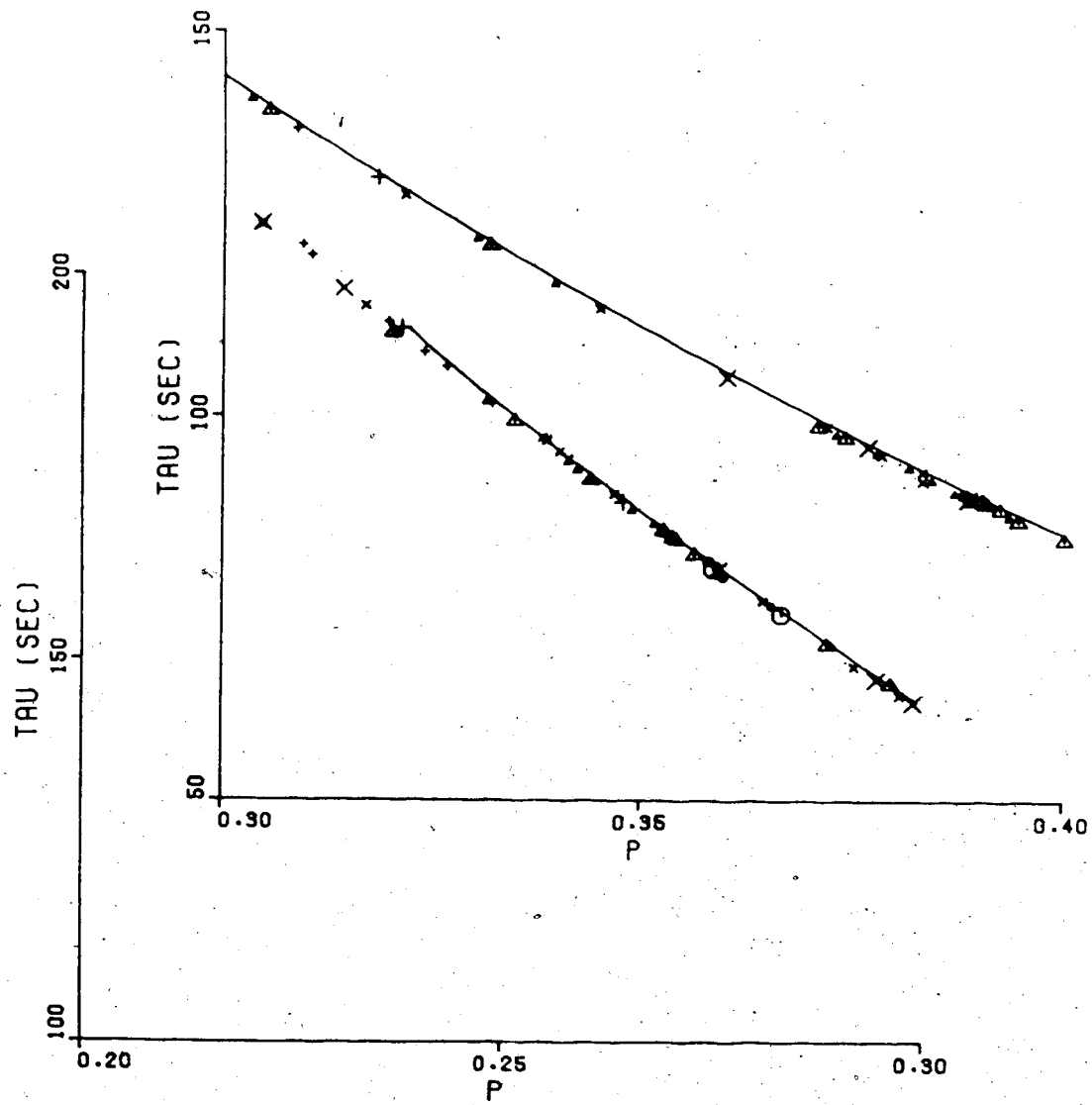
set of data  $\tau_{\text{obs}}(p_{\text{obs}})$  may be acquired where  $p_{\text{obs}}$  is the observed slowness and  $\tau_{\text{obs}}(p_{\text{obs}})$  is the observed value of  $\tau$ . This data set is representative of the earth's 'average' spherically symmetric properties and as was the case for the discussion of  $\Delta(p)$ , azimuthal information has been discarded. Figures 2.14 a and b show the  $\tau(p)$  observations for the 1974 VASA; the  $p$  axis has been normalized such that a value  $p = 1$  corresponds to a 'horizontal' ray and an earth surface velocity of 6 km/sec. The actual slowness in sec/deg may be recovered by the relation  $p_{\text{actual}} = (p \times 6371 \times 2\pi) / (360 \times 6)$ . As in past diagrams large and small symbols refer to VASA1 and VASA2 calculations respectively and the various symbols identify event azimuth (see figure 2.9).  $T(p)$  has been taken to be the average of the observed travel times for the combination of stations used corrected to surface focus and  $\Delta(p)$  has been taken to be the distance between the event epicenter and the center of the combination of stations used, again corrected to surface focus. As was the case for the  $\Delta(p)$  study the Haddon-Bullen (1969) P wave velocity model was used for surface focus corrections. The empirical line in figure 2.14 is based upon numerical differentiation of the J-B P wave tables for a surface focus. The technique of differentiation has been described in the section concerning the  $\Delta(p)$  plane. Notice that the

Figure 2.14 a and b

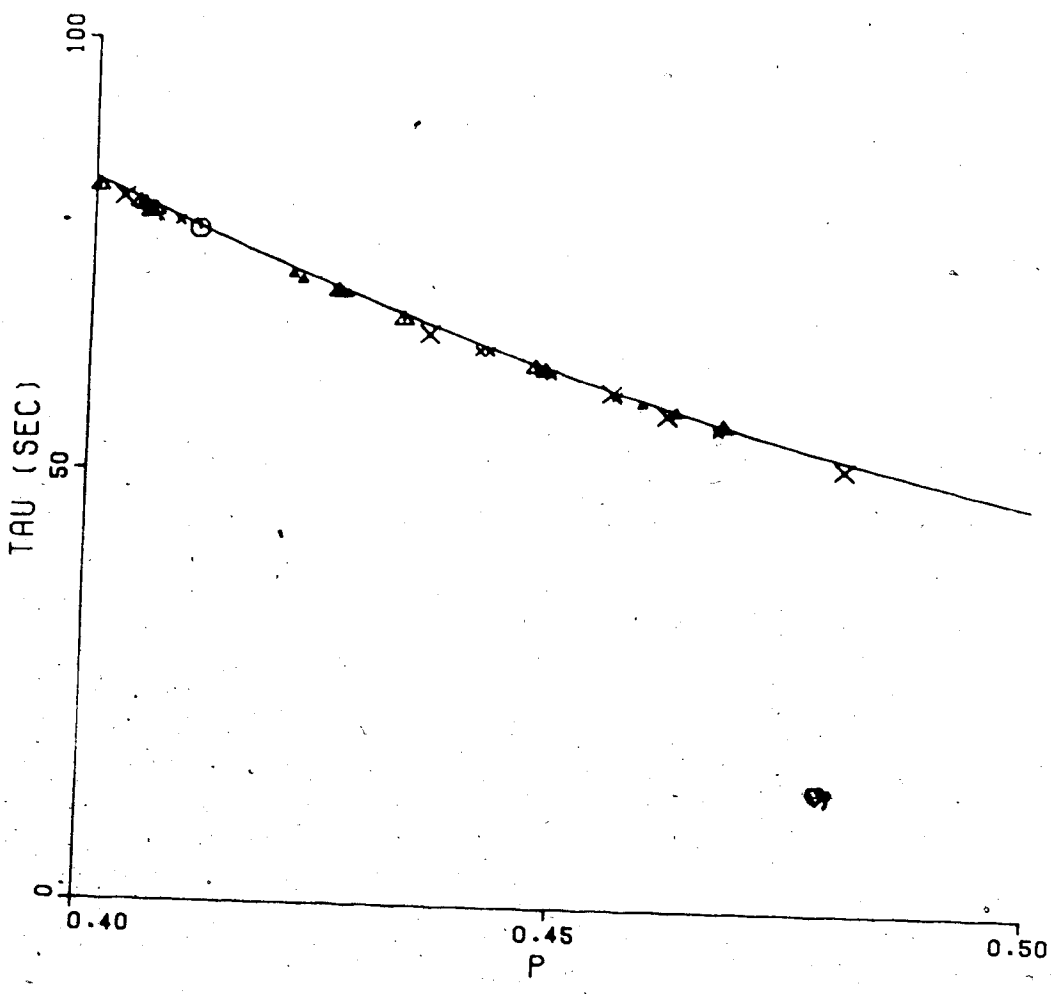
The 1974 VASA  $\tau(p)$  observations. The various symbols refer to azimuthal groups with larger and smaller symbols associated with VASA1 and VASA2 observations respectively (see figure 2.9). The empirical solid curve is based upon numerical differentiation of the Jeffreys - Bullen travel-time tables of P waves for surface focus. The slowness axis,  $p$ , has been normalized assuming a surface velocity of 6 km/sec. Actual slowness values in sec/deg may be recovered using the relation  $p_{\text{actual}} = (p \times 6371 \times 2\pi) / (360 \times 6)$ .

The set of axes applicable to the data shown are in accordance with the inequality  $d\tau/dp < 0$ .





(a)



(b)

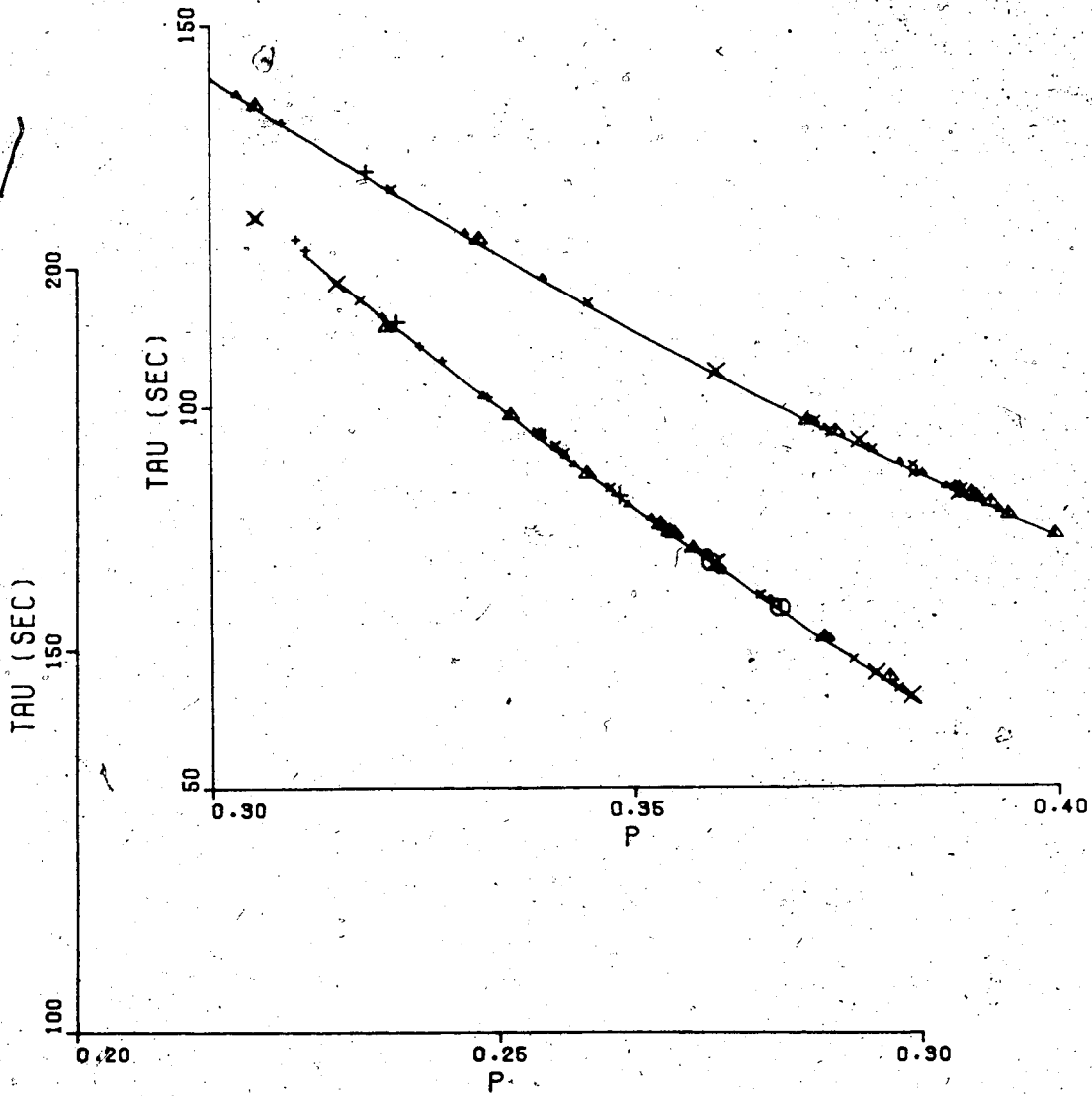
calculated  $\tau(p)$  values are decidedly lower than would be predicted by the J-B tables especially in the  $p$  region of 0.30 to 0.48 (5.50 to 8.9 sec/deg). Also the J-B curve proceeds to no lower  $p$  values than about 0.24 (or 4.4 sec/deg) whereas the observed values extend to  $p$  values less than this. This anomalous feature has been discussed in the previous sections. Now Hales et al (1968) have provided an expression between  $T$  and  $\Delta$  based on teleseismic observations. The relation which assumes a source upper mantle velocity structure associated with tectonically active regions and a receiver upper mantle structure associated with stable continental regions is,

$$T(\Delta) = 72.77 + 10.9210\Delta - 3.2087 \times 10^{-2} \Delta^2 - 2.003 \times 10^{-5} \Delta^3 \quad (2.2)$$

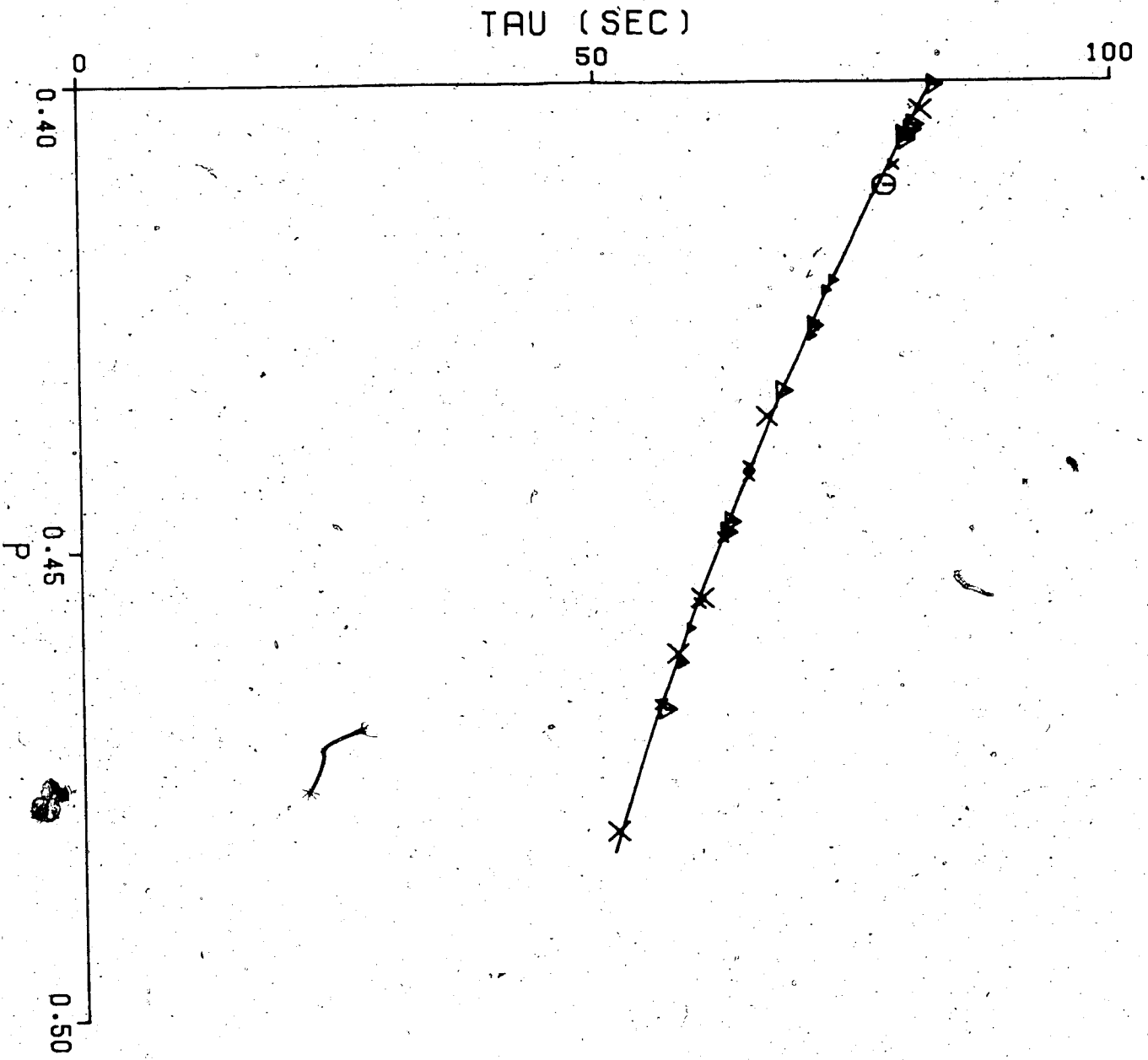
where  $\Delta > 30^\circ$  and  $T$  is given in seconds. In view of the location of events (figure 2.8) and the array used in this study it is felt that the above expression should be comparable to the 1974 VASA observations. Using the fact that  $\frac{d\tau(p)}{dp} = -\Delta(p)$  and hence that  $\tau(p)$  is a monotonically decreasing function (see Chapter 3) one can construct an empirical  $\tau(p)$  curve based upon the  $T(\Delta)$  relation above given by Hales et al (1968). Figures 2.15 a and b show the same  $\tau(p)$  observations as those in figures 2.14 a and b but the empirical curve is now

Figure 2.15 a and b

The 1974 VASA  $\tau(p)$  observations. All descriptions are the same as those for figures 2.14 a and b except that the solid empirical curve here is based upon the  $T(\Delta)$  relation (equation 2.2) of Hales et al (1968).



(a)



(b)

based upon the above  $T(\Delta)$  relation; there is a striking similarity between the observations and this empirical curve. Unlike the case for the J-B comparison, points no longer fall decidedly away from the solid line and the Hales et al. (1968)  $\tau(p)$  curve extends to a  $p$  value as low as about 0.227 (4.20 sec/deg) approaching the low values of the observations. The Hales et al. (1968) velocity depth profile is consistent with their  $T(\Delta)$  relation to within 0.01 sec. The velocities are always greater than the J-B model with a maximum deviation of about 0.1 km/sec occurring at a depth of about 1200 km and substantially smaller deviations throughout the rest of the lower mantle. Thus the 1974 VASA  $\tau(p)$  observations are in accordance with an 'overall' spherically symmetric P wave velocity profile which is slightly greater than the model of Jeffreys and Bullen. The empirical  $T(\Delta)$  relation of Hales et al. (1968) should be considered a serious candidate for a basis of comparison for future array P wave studies.

### Conclusions

The Covespa technique proved to be useful for the slowness and azimuth calculations of teleseismic P waves crossing the 1974 Variable Aperture Seismic Array. Deviations of the slowness and azimuth observations from quantities which are in accordance with a spherically

symmetrical earth for which the kinematic properties of teleseismic P waves are defined by the Jeffreys-Bullen Seismological Tables are in accordance with the existence of lateral P wave velocity inhomogeneities along the paths of rays between event locations and VASA. If lateral velocity changes in the crust and upper mantle under VASA are severe then the slowness and azimuth observations would be a poor indication of possible deep mantle anomalies. However preliminary indications are that this is not the case. If vector ray parameter deviations are associated with anomalous velocity conditions at the ray bottoming points (the region to which vector ray parameters are most sensitive) then low slowness values near  $\Delta \approx 50^\circ$  are in accordance with anomalously high velocity-depth gradients at a depth of about 1200 km, low slowness values for  $\Delta > 85^\circ$  are consistent with velocity inhomogeneities near the core-mantle boundary under some areas of the Pacific Ocean, and azimuthal deviations associated with rays passing under a region near the Caribbean point to anomalous velocity conditions predominated by lateral velocity gradients at depths between 1900 and 2600 km under that region. Also the 1974 VASA slowness observations can be expected for rays emerging from tectonically active regions, passing through an 'average' spherically symmetric lower mantle for which the P wave velocity is slightly greater than



the Jeffreys-Bullen designation, and impinging upon a seismic array in a stable continental region.

## CHAPTER 3

### INVERSION OF TRAVEL-TIME DATA USING THE TAU METHOD

#### Introduction

In past linear seismic arrays have been used widely for the investigation of crustal and upper mantle structure. Travel-time distance curves have been inverted to obtain spherically symmetrical velocity depth functions using various inversion techniques. Inversion techniques may be divided into two major categories; indirect methods (for example, Backus and Gilbert (1970)) and direct methods such as the Herglotz-Wiechert techniques. Attention here will be focused upon powerful technique of seismic travel-time inversion, the Tau method, which was developed by Bessonova et al (1974). The method makes use of the function

$$\tau(p) = T(p) - pX(p) \quad (3.1)$$

where  $p = dT/dX$  is the ray parameter,  $X$  is half the epicentral distance, and  $T$  is half the travel time from source to receiver. It was shown that it is possible to map limits of the function  $\tau(p)$  into limits for the velocity depth function  $V(y)$ . Thus with  $\tau(p)$  estimated from  $T(X)$  observations an envelope may be obtained in the  $V(y)$  plane which contains all possible velocity depth profiles that

are consistent with the data. Prior to the development of the Tau method the Herglotz-Wiechert method of inversion, which maps the function  $X(p)$  into  $V(y)$ , was widely used for direct inversion. In its classical form the Herglotz-Wiechert method was restricted to velocity-depth profiles for which there are no velocity reversals (Herglotz (1907) and Wiechert (1910)). Gerver and Markushevich (1966) overcame this serious restriction by developing a 'Herglotz-Wiechert type' expression which accounted for the presence of low velocity zones. But this inversion scheme still suffered from a serious setback since it implicitly assumed that the function  $X(p)$  was known exactly. Accordingly McMechan and Wiggins (1972) extended the Gerver-Markushevich formula to an extremal inversion scheme which mapped limits in the  $X(p)$  plane into limits in the  $V(y)$  plane. The disadvantage of this method is that it is difficult to put bounds on the function  $X(p)$  since  $X(p) \rightarrow \infty$  when a smooth velocity reversal is encountered. The function  $\tau(p)$ , on the other hand, is well behaved since it decreases monotonically and responds to a low velocity zone by exhibiting a finite discontinuity. It is expected that the Tau method of seismic inversion will become a standard tool in the interpretation of crustal, upper mantle, and teleseismic data.

In this chapter a new method for obtaining bounds

for the function  $\tau(p)$ , using data from linear arrays, is presented. For each branch of the travel-time curve,  $T$  observations are fitted to a family of second order polynomials in  $X$ . The families of curves are then mapped into the  $\tau(p)$  plane. The Tau method will be illustrated by inverting  $T(X)$  data recorded by the University of Alberta on Project Early Rise. A comparison of the results of this study with those of numerous other authors will be given. Also, it is stressed that uncertainty in velocity depth profiles is due partly to errors in the quantities  $T$ ,  $X$ , and  $p$  and it is also affected by the fact that observations of  $T$ ,  $X$ , and  $p$  are incomplete; thus the resolving power, as a function of separation of observation points, of the Tau method is examined by inverting  $\tau(p)$  envelopes calculated from exact velocity-depth functions.

#### Mapping $\tau(p)$ .Limits into Velocity-Depth Limits

The following analysis highlights the essential features of the Tau method described by Bessonova et al (1974) and also includes some interesting points which became apparent during various calculations.

It is convenient to discuss the inversion problem in terms of a flat earth model; the flat earth transformation makes this possible. Suppose we have a spherical velocity function  $v(r)$ , where 'r' is the radial coordinate

from the center of the earth, and associated body wave observations  $T(p)$ ,  $\Delta(p)$  and  $p = dT/d\Delta$  where  $T(p)$  is the half travel time and  $\Delta(p)$  is the half epicentral distance. The normalized earth flattening transformation is,

$$\begin{aligned} X &= \frac{R}{v(R)} \Delta \\ p &= \frac{dT}{dX} \\ y &= \frac{R}{v(R)} \ln \frac{R}{r} \\ u(y) &= \frac{v(R) e^{-\frac{v(R)}{R} y}}{v(R) e^{\frac{v(R)}{R} y}} \end{aligned} \quad (3.2)$$

The normalized flat earth model defined by (3.2) is characterized by horizontal distance coordinate  $X(p)$ , general depth coordinate, 'y', and slowness depth profile  $u(y)$  where  $u(0) = 1$ . Rays in this flat earth satisfy Snell's law,  $\sin \alpha(y) = pu(y)$  where  $\alpha$  is the angle between the y axis and the direction of the ray. The problem now reduces to mapping limits of the function  $\tau(p) = T(p) - pX(p)$  into upper and lower bounds for the depth,  $Y(p)$ , at which the ray with parameter  $p$  bottoms. It is extremely important to realize that the mathematical expressions required for inversion, and indeed the properties of  $T(p)$ ,  $X(p)$ ,  $\tau(p)$  and other functions related to seismic ray propagation, are based upon the following assumptions regarding the slowness-depth profile  $u(y)$  given by Gervert and

Markushevich (1972);

(a) The function  $u(y)$  is positive and scaled so that  $u(0) = 1$ . (Note that this is ensured by the transformation (3.2)).

(b) The function  $u(y)$  is everywhere twice continuously differentiable, with the exception of a finite number of points at which it or its derivatives either do not exist or are discontinuous.

(c) In every finite segment,  $u(y)$  is bounded, but on the entire semiaxis  $y \geq 0$  it is not necessarily bounded.

(d) There exists a finite number of waveguides (low velocity zones). If we define the function  $s(y)$  by  $s(y) = \sup\{u(y^0), y^0 \in [0, y]\}$  then the waveguides are intervals of the  $y$  axis that have the following properties;

(i)  $s(y)$  is constant in each of them.

(ii) Each of them contains points where  $u(y) < s(y)$ .

(iii) Outside these intervals,  $u(y) = s(y)$ .

The assumptions (a), (b), (c), and (d) above clearly do not impose any serious limitations when one is dealing with practical spherically symmetric earth models but as has been mentioned they are needed for the mathematical development of the inversion problem. Now the low velocity zones are ordered by the index "i" and are described by,

$\underline{y}_i$  = depth to the top of the  $i^{\text{th}}$  low velocity zone.

$\bar{y}_i$  = depth to the bottom of the  $i^{\text{th}}$  low velocity zone.

$q_i$  = slowness at the top of the  $i^{\text{th}}$  low velocity zone.

Notice that the functions  $Y(p)$  and  $u(y)$  are mutual inverses outside the low velocity zones; thus flat earth bounds for  $Y(p)$  may be transformed into bounds for the spherical earth velocity function  $v(r)$  outside the waveguides using (3.2). It is important to realize that it is implicitly assumed that the travel-time curve is composed of unconverted body wave phases and that if a ray is reflected then it is totally reflected. A precise mathematical statement of this assumption is,

$$Y(p) = \inf\{y, pu(y) \geq 1\}, \text{ for } p \in (0,1).$$

Now the solution of the inverse problem is (Gervert and Markushevich (1966)),

$$Y(p) = 2\pi^{-1} \int_p^1 x(q) [q^2 - p^2]^{-1/2} dq + \sum_i 2\pi^{-1} \int_{\underline{y}_i}^{\bar{y}_i} \tan^{-1}\{[u^2(y) - q_i^2]/[q_i^2 - p^2]\}^{1/2} dy. \quad (3.3)$$

The summation is taken over all low velocity zones for which  $p < q_i$ .

Let us consider the average depth of bottoming  $\tilde{Y}(m_1, m_2)$  for a package of rays  $m_1 \leq p \leq m_2$ ,

$$\tilde{Y}(m_1, m_2) = (m_2 - m_1)^{-1} \int_{m_1}^{m_2} Y(p) dp . \quad (3.4)$$

From (3.3) and (3.4),  $\tilde{Y}(m_1, m_2)$  can be written as

$$\tilde{Y}(m_1, m_2) = \phi(m_1, m_2) - \psi(m_1, m_2) . \quad (3.5)$$

The function  $\phi(m_1, m_2)$  is related to the Herglotz-Wiechert portion (first term) of the right hand side of (3.3) and it is given by

$$\begin{aligned} \phi(m_1, m_2) = 2\pi^{-1} (m_2 - m_1)^{-1} & \left\{ \int_{m_1}^{m_2} (q) m_1 q^{-1} (q^2 - m_1^2)^{-\frac{1}{2}} dq \right. \\ & \left. + \int_{m_2}^1 \tau(q) \left[ m_1 q^{-1} (q^2 - m_1^2)^{-\frac{1}{2}} - m_2 q^{-1} (q^2 - m_2^2)^{-\frac{1}{2}} \right] dq \right\} \quad (3.6) \end{aligned}$$

If no low velocity zones are present or if for every low velocity zone  $q_i < m_1$ , then  $\tilde{Y}(m_1, m_2) = \phi(m_1, m_2)$ . The term  $\psi(m_1, m_2)$  is related to the low velocity zones and is given by

$$\psi(m_1, m_2) = 2\pi^{-1} \sum_{q_i > m_1} B_i(m_1, m_2) \quad (3.7)$$

where

$$\begin{aligned} B_i(m_1, m_2) = (m_2 - m_1)^{-1} & \left[ \sigma_i \alpha(q_i; m_1, m_2) \right. \\ & \left. - \int_{m_1}^{\min(m_2, q_i)} \int_{-y_i}^y \tan^{-1} \{ [u^2(y) - q_i^2] / [q_i^2 - p^2] \}^{\frac{1}{2}} dy dp \right] \quad (3.8) \end{aligned}$$



and

$$\alpha(q_i; m_1, m_2) = \begin{cases} \arccos(m_1/q_i) & \text{if } m_1 \leq q_i \leq m_2 \\ \arccos(m_1/q_i) - \arccos(m_2/q_i) & \text{if } m_2 \leq q_i \leq 1. \end{cases} \quad (3.9)$$

The summation in (3.7) is taken over all low velocity zones for which  $q_i > m_1$ . It is possible to show that  $B_i(m_1, m_2) > 0$ . Also, when  $m_2 < q_i$ , then there exists a value  $\gamma$ ,  $m_1 < \gamma < m_2$ , such that

$$B_i(m_1, m_2) = \int_{\underline{y}_i}^{\bar{y}_i} [Q_i - \tan^{-1} Q_i] dy \quad (3.10)$$

where

$$Q_i = \{[u^2(y) - q_i^2]/[q_i^2 - \gamma^2]\}^{1/2}.$$

The expression (3.10) for  $B_i(m_1, m_2)$  is particularly useful for two reasons. In practise we do not know  $q_i$  and  $\sigma_i$  exactly. From the T(X) data however we can find limits for  $q_i$  and  $\sigma_i$  (Bessonova et al (1974)) such that

$$\underline{q}_i \leq q_i \leq \bar{q}_i$$

and

$$\underline{\sigma}_i \leq \sigma_i \leq \bar{\sigma}_i.$$

Next we assume that the slowness in the  $i^{\text{th}}$  low velocity zone is less than some given value  $\bar{u}_i$ :

$$u(y) \leq \bar{u}_i \quad \text{for} \quad \underline{y}_i \leq y \leq \bar{y}_i.$$

Using (3.10), the upper bound,  $\bar{B}_i(m_1, m_2)$ , such that  $B_i(m_1, m_2) \leq \bar{B}_i(m_1, m_2)$  is given by:

$$\bar{B}_i(m_1, m_2) = \bar{\sigma}_i [q_i^2 - \gamma^2]^{-1/2} [1 - \bar{Q}_i^{-1} \tan^{-1} \bar{Q}_i] \quad (3.11)$$

where

$$\bar{Q}_i = \{([\bar{u}_i - q_i^2] / [q_i^2 - \gamma^2])^{1/2}\}.$$

Thus  $B_i(m_1, m_2)$  is maximal when the low velocity zone is rectangular and takes on the maximum possible velocity. Furthermore, the maximum thickness,  $\bar{h}_i$ , for the  $i^{\text{th}}$  low velocity zone can be found using the induction method described by Bessonova et al (1974). The lower bound,  $\underline{B}_i(m_1, m_2)$ , such that  $B_i(m_1, m_2) \geq \underline{B}_i(m_1, m_2)$  is then given by:

$$\underline{B}_i(m_1, m_2) = \underline{\sigma}_i [q_i^2 - \gamma^2]^{-1/2} [1 - \underline{Q}_i^{-1} \tan^{-1} \underline{Q}_i] \quad (3.12)$$

where

$$\underline{Q}_i = \{([u_i^2 - q_i^2] / [q_i^2 - \gamma^2])^{1/2}\}$$

and

$$\underline{u}_i = \{\sigma_i^2 / \bar{h}_i^2 + q_i^2\}.$$

Thus,  $B_i(m_1, m_2)$  is minimal when the low velocity zone is rectangular and as thick as possible. The form (3.10) for  $B_i(m_1, m_2)$  is instrumental in the analytical determination of the upper and lower bounds, (3.11) and (3.12) respectively, for  $B_i(m_1, m_2)$ . It is also useful for computational purposes. This can be seen by examining the

expression for  $B_i(m_1, m_2)$  given by (3.8); the second term on the right hand side of the expression involves an integration, with respect to the variable 'p', which cannot be performed explicitly. The expression (3.10) for  $B_i(m_1, m_2)$  is exact for some unknown value of  $\gamma$  such that  $m_1 < \gamma < m_2$ . However, even though we do not know  $\gamma$  exactly, approximations for the right hand sides of (3.10), (3.11), and (3.12) may be made by taking  $\gamma = (m_1 + m_2)/2$ . Of course, we expect the approximation to be good if the interval  $(m_1, m_2)$  is small. I have performed several calculations comparing the 'exact' value (3.8) with the approximate value (3.10), where  $\gamma = (m_1 + m_2)/2$ , for rectangular low velocity zones. The integration with respect to 'p', in (3.8), was done numerically. In all cases it was found that results from (3.8) and (3.10) compare favourably.

We have upper and lower limits,  $\bar{B}_i(m_1, m_2)$  and  $\underline{B}_i(m_1, m_2)$  respectively, for the functions  $B_i(m_1, m_2)$ . Now suppose that we have upper and lower bounds for the function  $\tau(p)$  in the interval  $(d, 1)$  such that

$$\underline{\tau}(p) \leq \tau(p) \leq \bar{\tau}(p) \quad \text{for} \quad 0 < d \leq p \leq 1.$$

Then for  $m_1 > d$  there exist two functions,  $f(m_1, m_2)$  and  $g(m_1, m_2)$ , which bound  $\phi_1(m_1, m_2)$ :

$$f(m_1, m_2) < \phi_1(m_1, m_2) \leq g(m_1, m_2) \quad (3.13)$$

where

$$f(m_1, m_2) = 2\pi^{-1} (m_2 - m_1)^{-1} \left\{ \int_{m_1}^{m_2} \underline{\tau}(q) m_1 q^{-1} (q^2 - m_1^2)^{-1/2} dq \right. \\ \left. + \int_{m_2}^1 \bar{\tau}(q) (m_1 q^{-k} (q^2 - m_1^2)^{-1/2} - m_2 q^{-1} (q^2 - m_2^2)^{-1/2}) dq \right\} \quad (3.14)$$

and

$$g(m_1, m_2) = 2\pi^{-1} (m_2 - m_1)^{-1} \left\{ \int_{m_1}^{m_2} \bar{\tau}(q) m_1 q^{-1} (q^2 - m_1^2)^{-1/2} dq \right. \\ \left. + \int_{m_2}^1 \underline{\tau}(q) (m_1 q^{-1} (q^2 - m_1^2)^{-1/2} - m_2 q^{-1} (q^2 - m_2^2)^{-1/2}) dq \right\}. \quad (3.15)$$

Now since  $Y(p)$  is a monotonic non-decreasing function we have,

$$\left. \begin{aligned} Y(m) &\leq \tilde{Y}(m_1, m_2) && \text{for } m \geq m_2 \\ Y(m) &\geq \tilde{Y}(m_1, m_2) && \text{for } m \leq m_1 \end{aligned} \right\} \quad (3.16)$$

Using (3.5), (3.11), (3.12), (3.13), (3.14), (3.15), and (3.16) then, it is possible to find upper and lower bounds for the function  $Y(p)$  in the interval  $d < p < 1$ . We assume  $\underline{\tau}(p) \leq \tau(p) \leq \bar{\tau}(p)$  for  $d \leq p \leq 1$  and that there are 'NL' non overlapping low velocity zones defined by,

$$(\underline{q}_i, \bar{\sigma}_i, \underline{q}_i, \bar{q}_i, \underline{u}_i, \bar{u}_i) \quad i = 1, NL$$

$$\bar{q}_{i+1} < \underline{q}_i$$

For simplicity we assume that the first low velocity zone

does not commence at the surface and also that the last low velocity zone does not commence at the deepest point of the observations. Thus  $\bar{q}_1 < 1$  and  $q_{NL} > d$ .

In the absence of low velocity zones, the upper and lower estimates of  $Y(p)$ , namely  $\bar{Y}(p)$  and  $\underline{Y}(p)$ , are given by:

$$\bar{Y}(p) = \inf\{g(m_1, p) : d \leq m_1 \leq p\} \quad (3.17)$$

$$\underline{Y}(p) = \sup\{f(p, m_2) : p < m_2 \leq 1\} \quad (3.18)$$

Now, let  $r(p)$  and  $s(p)$  be defined by:

$$f(p, r(p)) = \sup\{f(p, m_2) : p < m_2 \leq 1\} \quad (3.19)$$

$$g(s(p), p) = \inf\{g(m_1, p) : d \leq m_1 < p\} \quad (3.20)$$

In general, we calculate upper and lower bounds for  $Y(p)$  for  $p$  values  $(p_j, j=1, N)$  where  $p_j > p_{j+1}$ . When low velocity zones are present, the upper and lower estimates are given by:

$$\bar{Y}(p_j) = g(s(p_j), p_j) - \sum_{q_i > p_j} B_i(s(p_j), p_j) \quad (3.21)$$

$$\underline{Y}(p_j) = f(p_j, r(p_j)) - \sum_{q_i > r(p_j)} \bar{B}_i(p_j, r(p_j)) \quad (3.22)$$

In using (3.21) and (3.22), it is important to be aware of the following guidelines. First of all, calculations using (3.21) and (3.22) are done in order of decreasing  $p$  values; that is in order of increasing "j" values. In

(3.21) the summation is taken over all low velocity zones for which  $q_i > p_j$ . Also, if the interval  $(p_j, r(p_j))$  contains a low velocity zone, [that is, if there exists a  $q_k$  such that  $q_k \leq \bar{q}_k$  and  $p_j < q_k < r(p_j)$ ], then (3.22) is replaced by  $\underline{Y}(p_j) = \underline{Y}(p_{j-1})$ . Furthermore, notice that the values  $\underline{B}_i(s(p_j), p_j)$  are a priori unknown for non zero  $q_i$  since they require, from (3.12), knowledge of undetermined values  $\bar{h}_i$ . Thus, the following induction process is performed. In general,  $\bar{h}_n$  is the supremum of the difference  $\bar{Y}(p_j) - \underline{Y}(p_j)$ , calculated for  $p_j$  in the region  $q_n \leq p_j \leq \bar{q}_n$ , where  $\bar{Y}(p_j)$  and  $\underline{Y}(p_j)$  are given by (3.21) and (3.22) with allowance for the first  $(n-1)$  low velocity zones. Thus,  $\bar{h}_1$  is determined from (3.21) and (3.22) assuming no low velocity zones. Then, in turn,  $\bar{h}_2, \bar{h}_3, \dots, \bar{h}_{NL}$  are determined. Once all of the maximum thicknesses for the low velocity zones are given,  $\bar{Y}(p_j)$  and  $\underline{Y}(p_j)$  are given unambiguously by (3.21) and (3.22).

Notice that the functions  $f(m_1, m_2)$  and  $g(m_1, m_2)$ , given by (3.14) and (3.15) respectively, play an important role in the inversion process whether low velocity zones are present or not. In general, when  $\underline{I}(p)$  and  $\bar{I}$  are given as piecewise polynomials, of up to second degree in  $p$ , then (3.14) and (3.15) may be integrated explicitly to give  $f(m_1, m_2)$  as a piecewise smooth function of  $m_2$  for fixed  $m_1$  and  $g(m_1, m_2)$  as a piecewise smooth function of  $m_1$  for fixed  $m_2$ . The problem then is to determine

$\sup(f(m_1, m_2) : m_1 < m_2 \leq 1)$  for fixed  $m_1$  and  $\inf(g(m_1, m_2) : d \leq m_1 < m_2)$  for fixed  $m_2$ . In general, this is done by sampling  $f(m_1, m_2)$  for various  $m_2$  and  $g(m_1, m_2)$  for various  $m_1$ . There is at least one situation, however, in which sampling need only be done at 'preferred' points. For example, suppose that  $\bar{\tau}(p) = \tau_U$  (a constant) and  $\underline{\tau}(p) = \tau_L$  (a constant,  $\tau_U > \tau_L$ ) for the interval  $q_1 \leq p \leq q_2$ . Then, for fixed  $m_1 < q_1$ , the maximum value of  $f(m_1, m_2)$ , for  $m_2$  restricted to the interval  $q_1 \leq m_2 \leq q_2$ , will occur at either  $m_2 = q_1$  or  $m_2 = q_2$ . This follows from the fact that, in this case for  $q_1 \leq m_2 \leq q_2$ ,  $f(m_1, m_2)$  is doubly smooth and  $\frac{\partial^2 f(m_1, m_2)}{\partial m_2^2} > 0$ . Similarly, for fixed  $m_2 > q_2$ , the minimum value of  $g(m_1, m_2)$ , for  $m_1$  restricted to the interval  $q_1 \leq m_1 \leq q_2$ , will occur at either  $m_1 = q_1$  or  $m_1 = q_2$ . Accordingly, for  $q_1 \leq m_1 \leq q_2$ ,  $g(m_1, m_2)$  is doubly smooth and  $\frac{\partial^2 g(m_1, m_2)}{\partial m_1^2} < 0$ .

### Resolving Power as a Function of Station Spacing

It has been shown, (Herglotz, 1907) and (Wiechert, 1910) that in the absence of low velocity zones if  $X(p)$  is known exactly then  $V(y)$  is unique and can be calculated. The presence of a low velocity zone introduces uncertainty in the velocity-depth function below the low velocity zone. Gerver and Markushevich (1966) have obtained a theoretical expression which permits one to compute the

uncertainty in the velocity-depth function when any number of low velocity zones are present assuming that the functions  $X(p)$  and  $T(p)$  are completely determined. In practise, however, seismic observations are taken at discrete points,  $X_i$ , along the surface of the earth. Thus, even in the absence of low velocity zones, there will be uncertainty in the velocity depth profile due to the discrete nature of the observations. Davies and Chapman (1975) have discussed the discrete inversion problem, restricted to a travel-time branch within which neither triplications due to rapid increases in velocity nor discontinuities due to low velocity zones take place, in terms of the classical Herglotz-Wiechert method.

It is possible to study the effect that discrete  $T(X)$  data has upon the resolution of the velocity depth profile using the Tau method. It is assumed that exact observations of  $T$ ,  $X$  and  $p$  are obtained from  $N$  small linear arrays of seismometers with array spacing being  $\Delta X$  and the array lengths  $\ll \Delta X$ . In general, a given array may not provide a set of observations  $(T_i, X_i, p_i, i=1, N)$  since  $X_i$  may be located within a shadow zone and also a given array may provide more than one set  $T_i, X_i, p_i$  since  $X_i$  may be located within a region of triplication. For this example the function  $\tau(p)$  will be due to the discrete nature of the  $\tau_i(p_i)$  observations. Since  $\frac{d\tau}{dp} = -X(p)$ , and hence  $\tau(p)$  is monotonic decreasing, it is possible to



find functions  $\tau_U(p)$  and  $\tau_L(p)$  from the observations  $\tau_i(p_i)$  such that  $\tau(p)$  must satisfy,  $\tau_L(p) < \tau(p) < \tau_U(p)$ . For each interval  $(p_{i+1}, p_i)$  where  $p_i > p_{i+1}$  the upper and lower Tau bounds are given by,

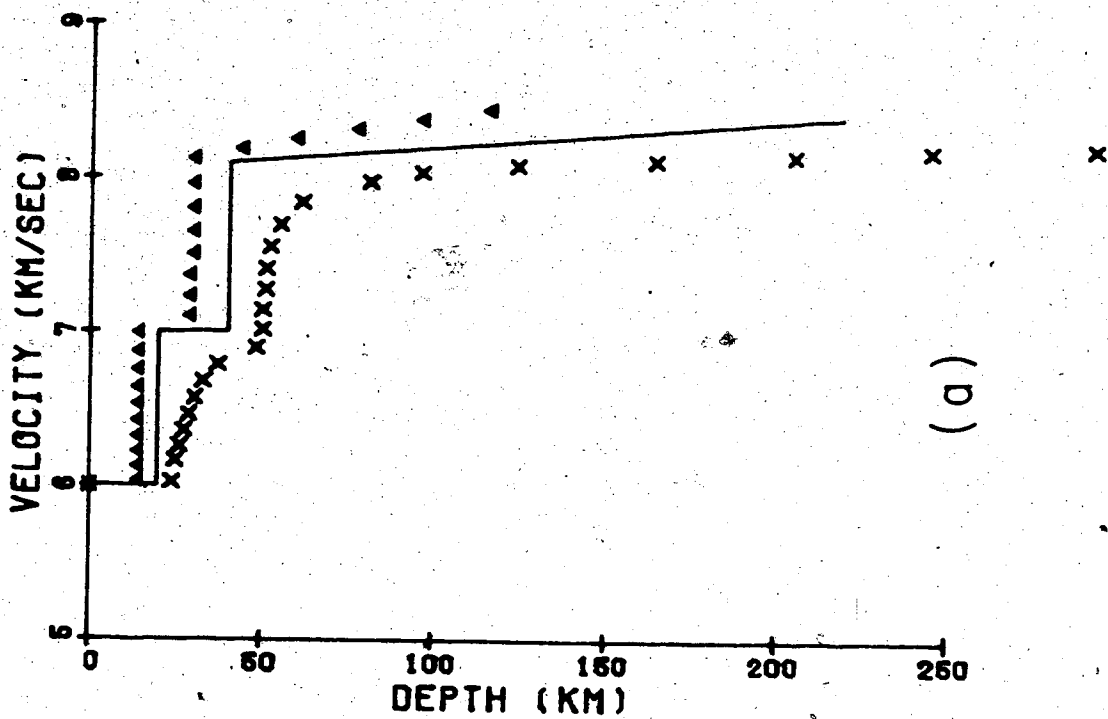
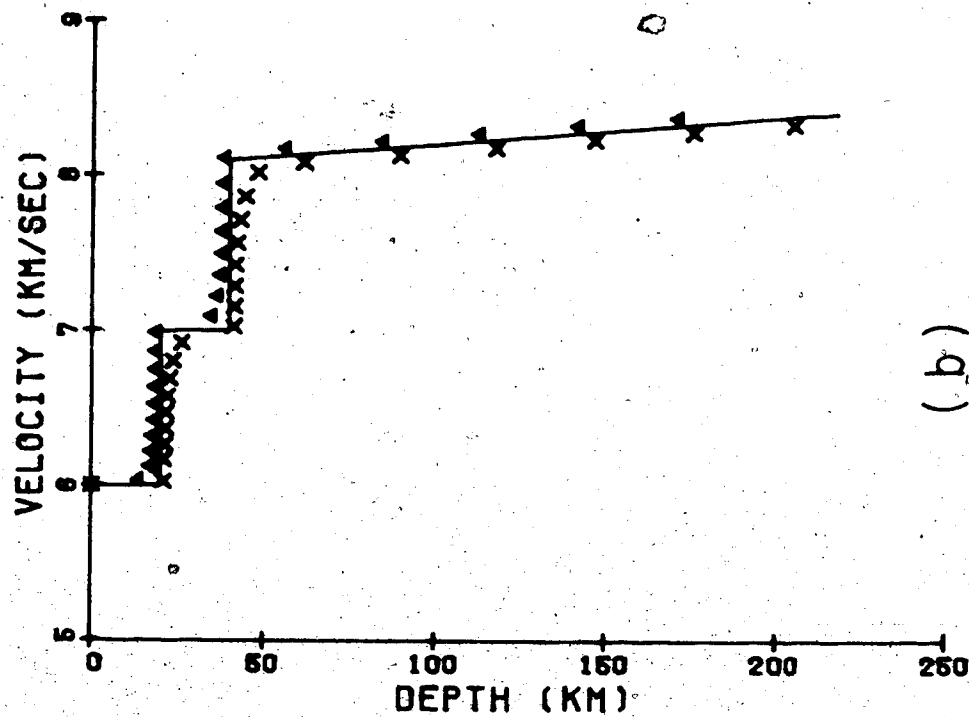
$$\tau_U(p) = \tau_{i+1}(p_{i+1})$$

$$\tau_L(p) = \tau_i(p_i)$$

Clearly a smaller station spacing  $\Delta X$  will result in a small  $\tau$  envelope defined by  $\tau_U(p)$  and  $\tau_L(p)$  since there will be more observations  $\tau_i(p_i)$ . A narrower  $\tau(p)$  envelope will in turn result in a narrower velocity envelope. An example of this is shown in figures 3.1 a and b. Figure 3.1 shows a hypothetical P wave velocity depth function. Using a direct ray program it is possible to calculate values  $T_i(p_i)$ ,  $X_i(p_i)$  and hence  $\tau_i(p_i)$  generated by such a structure using the Bullen (1963) ray integrals. Figures 3.1(a) and 3.1(b) show upper and lower velocity bounds calculated from theoretical observations based on the velocity model in figure 3.1 for station spacings of 100 km, and 25 km respectively. The inversion routine used for mapping  $\tau(p)$  limits into velocity-depth limits is after Bessonova (1974) and has been described in the preceding section. A similar analysis may be performed for any hypothetical velocity depth structure and thus aid in the determination of station spacing required for any given desired resolution.

Figure 3.1

Upper and lower velocity-depth bounds resulting from Tau inversion. In parts (a) and (b) the symbols represent the upper and lower bounds assuming exact knowledge of  $\tau(p)$  at intervals of 100 and 25 km respectively based upon the solid velocity-depth curve.



### Estimation of the Function $\tau(p)$ from Real Data

Before inverting travel-time data using the Tau. method it is necessary to find estimates for the function  $\tau(p)$  from  $T(X)$  observations. Bessonova et al (1974) formulate the problem of  $\tau(p)$  calculation using the Clairaut equation

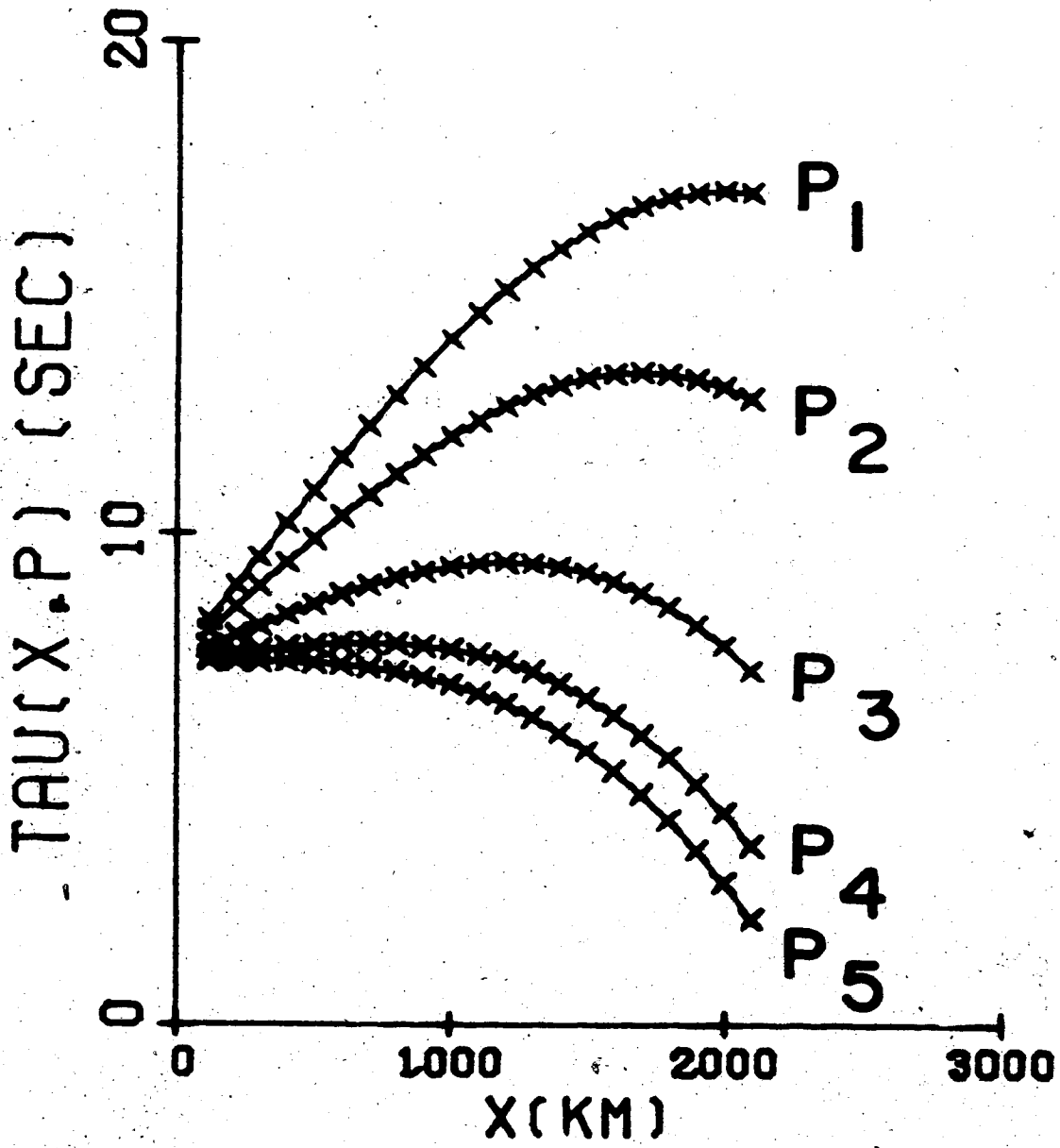
$$\tau(p) = p \frac{d\tau}{dp} + T \left( - \frac{d\tau}{dp} \right) \quad (3.23)$$

The set of particular solutions of (3.23) is given by (3.1). From the fact that  $p = \frac{dT}{dX}$ , Bessonova et al (1974) show that  $\tau(p)$  is the singular solution of (3.23); that is  $\tau(p)$  is equal to the value  $\tau(X, p)$  for which  $\frac{\partial \tau(X, p)}{\partial X} = 0$ . Thus for a generally forward branch within which the slope  $p = \frac{dT}{dX}$  is present  $\tau(p)$  will be equal to the maximum value of  $\tau(X_i, p)$  calculated for all  $X_i$ . For a generally receding branch  $\tau(p)$  will be the minimum value of  $\tau(X_i, p)$ . An example of this is shown in figure 3.2 for the forward branch consisting of rays which bottom within the first layer of the hypothetical velocity structure shown in figure 3.1. The peaks are very clear; in addition, as expected for a forward branch, the  $X$  coordinates of the peaks decrease with increasing  $p$  values. Bessonova et al (1974) use this regular behaviour of the peaks as an interpretational aid.

The method of  $\tau(p)$  calculation described above is excellent when errors in  $T(X)$  data are very small. On the

Figure 3.2

The function  $\tau(X,p)$  for the first forward travel-time branch arising from the hypothetical velocity curve of figure 3.1. The  $p$  values are such that  $p_{i+1} > p_i$ .



other hand, when even modest errors are present or when the elastic waves traverse layers with moderate heterogeneities it becomes increasingly difficult to extract  $\tau(p)$  information using "Clairaut's relation". Figure 3.3 shows the travel times and distances of the first branch from a seismic line recorded during Project Early Rise by the University of Alberta.

The graph of  $\tau(X_i, p)$  for  $p$  values  $p_1 > p_2 > p_3 > p_4 > p_5$  arising from this generally forward branch is shown in figure 3.4. Because of inhomogeneities in the layered media and possible errors in time, the regular behaviour which is exhibited by hypothetical example is not seen. In particular, for any fixed  $p$  value, there are several  $X$  positions at which  $\frac{\partial \tau(X_i, p)}{\partial X}$  is zero. The scatter in the travel-time points of figure 3.3 is typical of long range refraction surveys, and is in part due to local variations in crustal structure. Thus it is necessary to smooth  $T(X)$  in some manner in order to derive spherically symmetrical velocity depth functions. Kennett (1976) suggests that this may be done either by fitting a lightly smoothed spline to the function  $\tau(X_i, p)$  for fixed values of  $p$  or by interpolating each branch of the travel-time curve with a smoothed spline which is not required to pass precisely through the data values. For the former process errors in  $\tau(p)$  are of the same order as the errors in the  $T(X)$  values. Kennett (1976) found that values of  $\tau(p)$  obtained

Figure 3.3

Travel-time curve of first branch from the  
Yukon line of Project Early Rise.



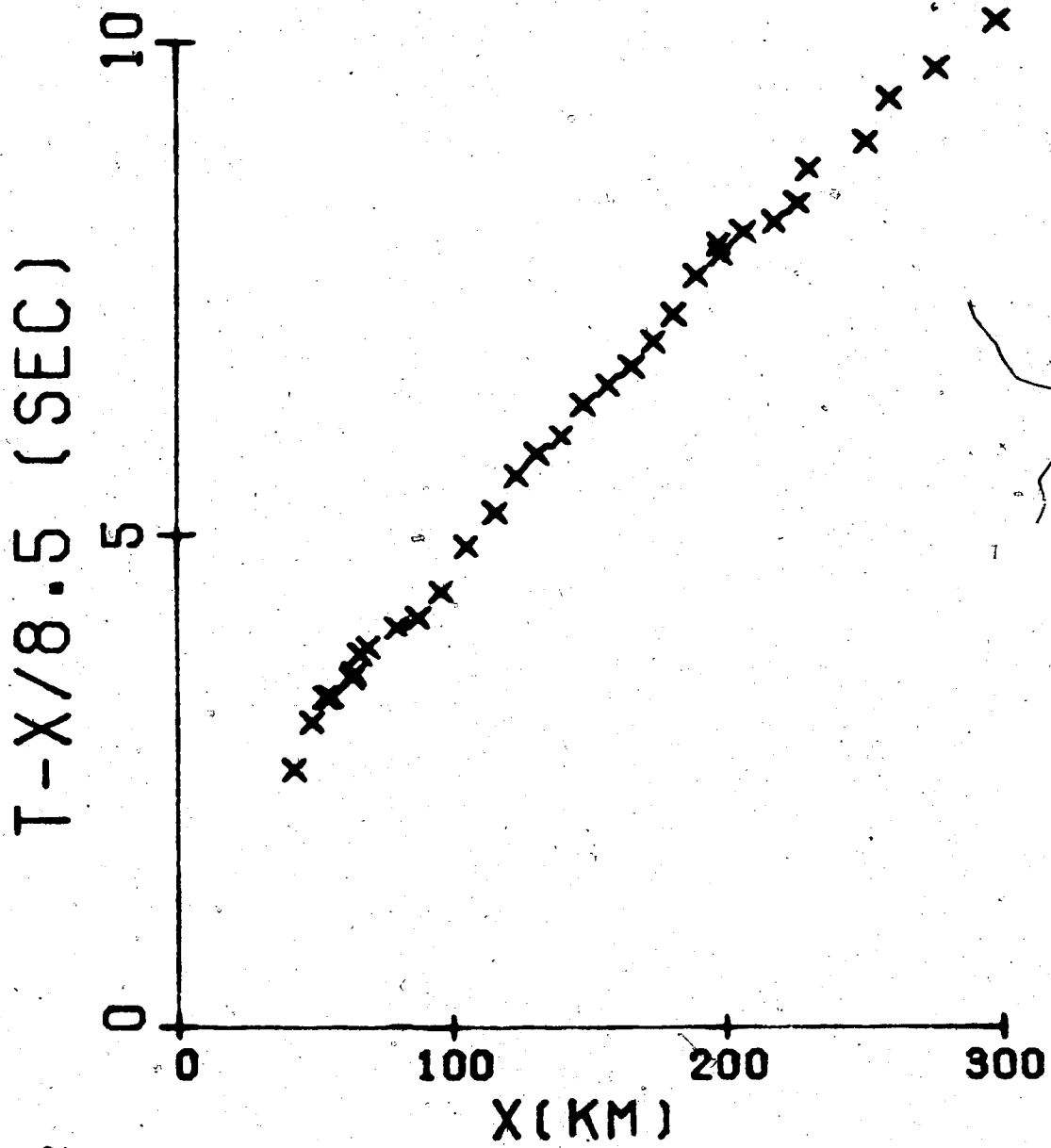
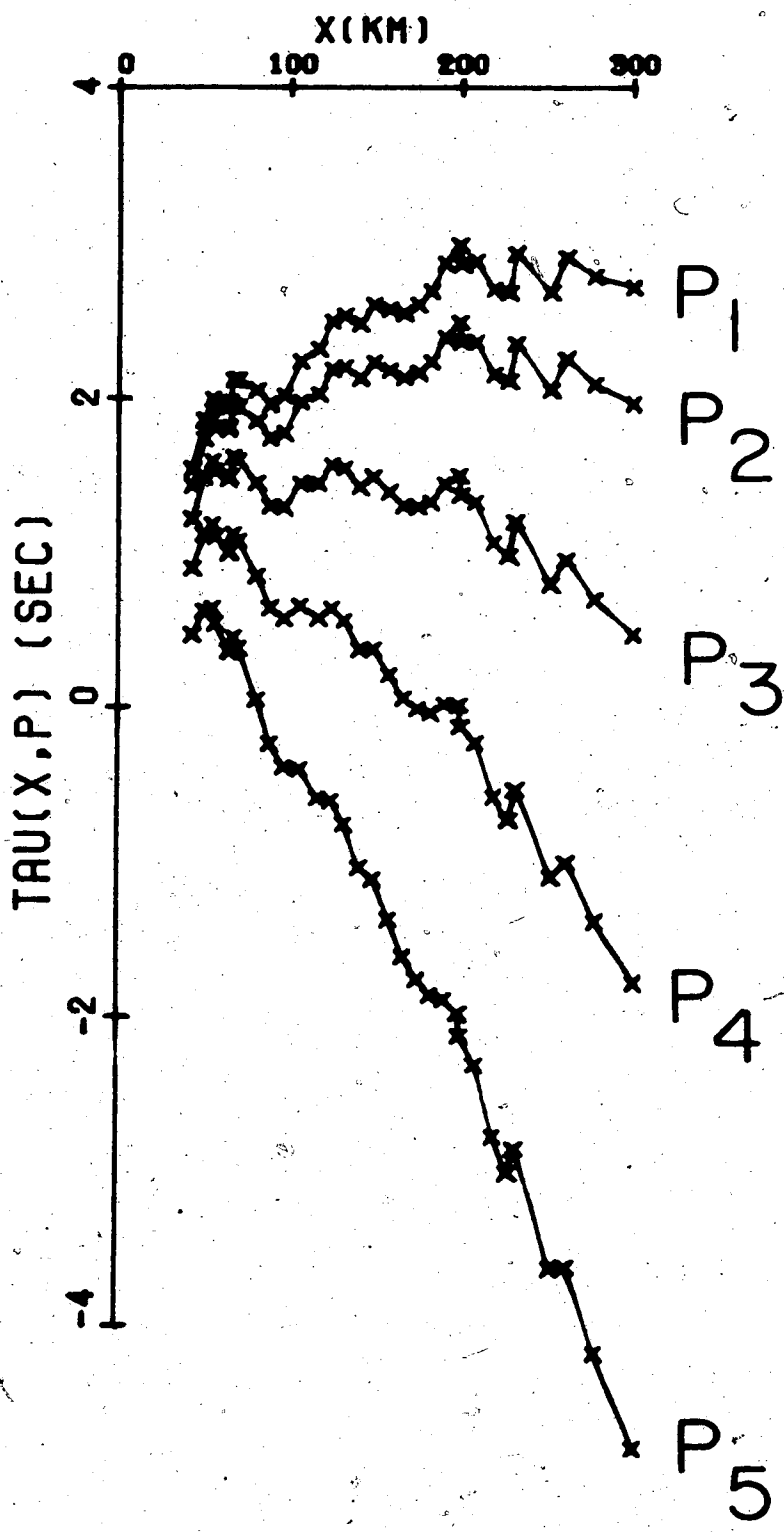


Figure 3.4

The function  $\tau(X,p)$  for the first travel-time branch from the Yukon line of Project Early Rise. The  $p$  values are such that  $p_{i+1} > p_i$ .



from the latter process were much more widely scattered than estimates using the graphical construction. Spline smoothing tends to overfit the data to a degree which is dependent upon the nature of the spline routine and I recommend an alternate procedure in which error estimates result directly from the process.

For real seismic data, travel-time branches are suitably approximated by a polynomial of the form:

$$T = a + bX + cX^2 \quad (3.24)$$

For a branch consisting of  $N$  points  $(T_i, X_i, i=1, N)$  the quality of the parameterization (3.24) is given by the root mean square error,

$$E(a, b, c) = \left\{ \left( \sum_{i=1}^N (a + bX_i + cX_i^2 - T_i)^2 \right) / N \right\}^{1/2} \quad (3.25)$$

From (3.1), (3.24) and the condition that  $\frac{\partial T}{\partial X} = 0$  the expression for the branch in the  $\tau(p)$  plane is

$$\left. \begin{aligned} \tau(p) &= a - \frac{b^2}{4c} + \frac{bp}{2c} - \frac{p^2}{4c} \\ b + 2cX_1 &\geq p \geq b + 2cX_N, \quad c < 0 \\ b + 2cX_N &\geq p \geq b + 2cX_1, \quad c > 0 \end{aligned} \right\} \quad (3.26)$$

where  $X_1$  and  $X_N$  are the smallest and largest  $X$  coordinates of the branch respectively. The best fit solution for  $T(X)$ , (3.24) and  $\tau(p)$ , (3.25) corresponds to values

$a = a_0, b = b_0, c = c_0$ , for which  $E(a,b,c)$  is a minimum.

Using  $\frac{\partial E}{\partial a} = \frac{\partial E}{\partial b} = \frac{\partial E}{\partial c} = 0$  and (3.26) the best solution is defined by

$$\begin{pmatrix} a_0 \\ b_0 \\ c_0 \end{pmatrix} = \begin{pmatrix} A_1 & A_2 & A_3 \\ A_2 & A_3 & A_4 \\ A_3 & A_4 & A_5 \end{pmatrix} \begin{pmatrix} B_1 \\ B_2 \\ B_3 \end{pmatrix}$$

$$= \begin{pmatrix} N & \Sigma X_i & \Sigma X_i^2 \\ \Sigma X_i & \Sigma X_i^2 & \Sigma X_i^3 \\ \Sigma X_i^2 & \Sigma X_i^3 & \Sigma X_i^4 \end{pmatrix} \begin{pmatrix} \Sigma T_i \\ \Sigma X_i T_i \\ \Sigma X_i^2 T_i \end{pmatrix} \quad (3.27)$$

with solutions taken over the points  $i = 1, N$  on the branch.

Now, letting  $E_0 = E(a_0, b_0, c_0)$  and  $E_\xi = \xi E_0$ , consider the set of real values  $(a, b, c)$  such that  $E(a, b, c) \leq E_\xi$ . Clearly when  $\xi < 1$ , the set is empty, and when  $\xi = 1$ , the set consists of one point in  $(a, b, c)$  space, namely  $a = a_0, b = b_0, c = c_0$ . For the case of  $\xi > 1$ , the set consists of more than one value  $(a, b, c)$  and it is possible to show that the set is of full measure. This multi-solution nature of the parameterization of  $T(X)$  data has in past caused ambiguity in the interpretation of seismic observations. Results from many long range refraction experiments have been interpreted in terms of layers of constant velocity; travel-time branches are parameterized by the simpler form  $T = a + bX$ , and the layered model is inferred

from the values of "a" and "b" from the various branches. Clearly, small errors in the values of "a" and "b" change the derived layered model making comparison of velocity models from different studies difficult.

There is no need for confusion however, since it is possible to find all values (a,b,c) which fit the T(X) data within any root mean square error  $E_\xi > E_0$ . The solution space corresponding to  $E_\xi > E_0$  is composed of all points within the ellipsoid defined by,

$$A_1 a^2 + A_3 b^2 + 2A_2 ab + 2a(cA_3 - B_1) + 2b(cA_4 - B_2) + c^2 A_5 - 2cB_3 + A_6 - (\xi E_0)^2 A_1 = 0 \quad (3.28)$$

where  $A_6 = \sum T_i^2$ . The ellipsoid is bounded by the planes  $c = c_{\min}$  and  $c = c_{\max}$ ,

$$c_{\min} = -(Q_2 + (Q_2^2 - 4Q_1 Q_3)^{1/2}) / (2Q_1) \quad (3.29)$$

$$c_{\max} = -(Q_2 - (Q_2^2 - 4Q_1 Q_3)^{1/2}) / (2Q_1)$$

where

$$Q_1 = A_1 (A_3 A_5 - A_4^2) + A_2 (2A_3 A_4 - A_2 A_5) - A_3^3$$

$$Q_2 = 2(B_1 (A_3^2 - A_2 A_4) + B_2 (A_1 A_4 - A_2 A_3) + B_3 (A_2^2 - A_1 A_3))$$

$$Q_3 = (A_6 - (\xi E_0)^2 A_1) (A_1 A_3 - A_2^2) + B_1 (2A_2 B_2 - A_3 A_1) - B_2^2 A_1$$

Thus provided  $c_{\min} \leq c \leq c_{\max}$ , the solution space in the (a,b) plane are points contained within the ellipse given

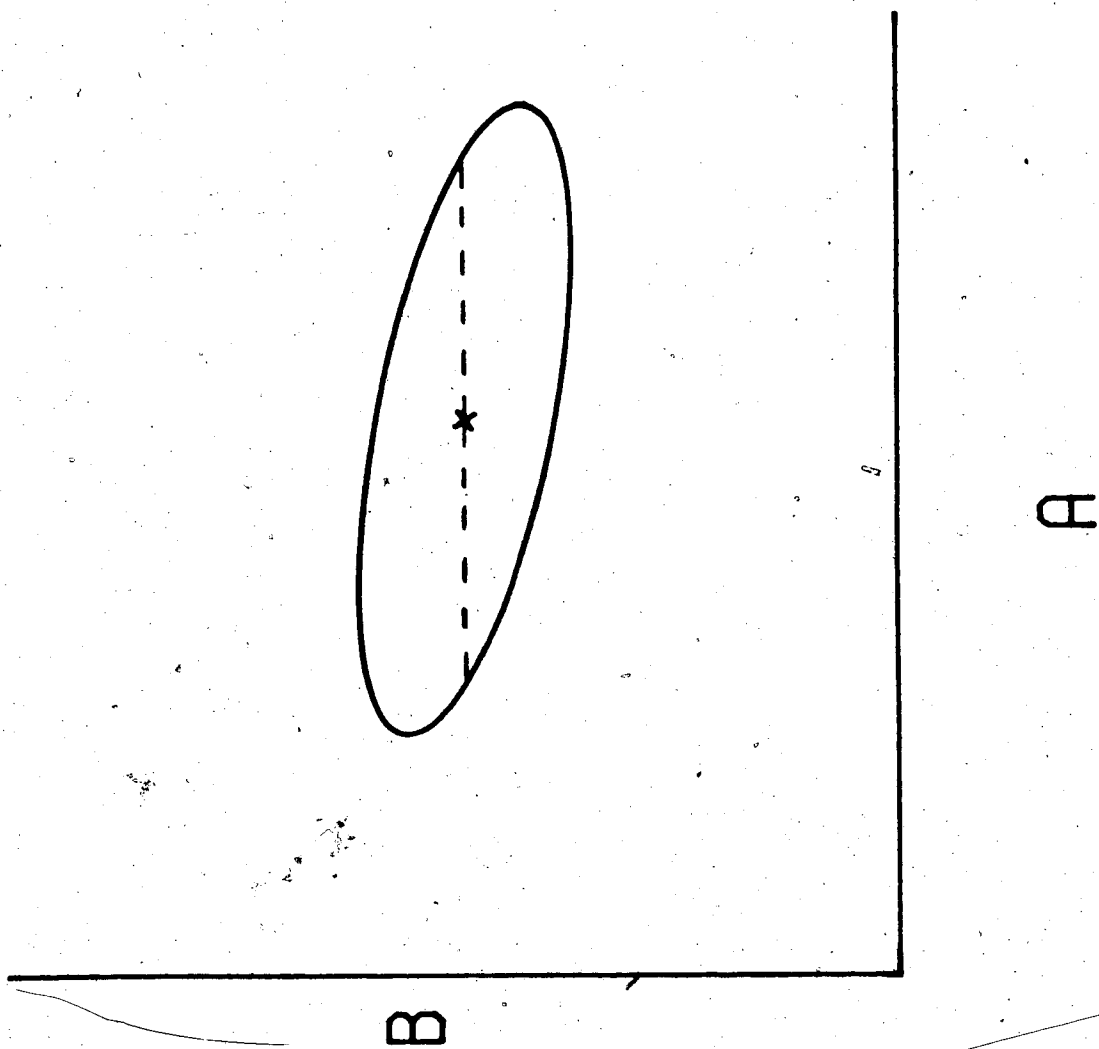
by (3.28).

In general for a fixed value of  $c$ , the ellipse in the  $(a,b)$  plane is of the form shown in figure 3.5. For typical experimental data the major axis is tilted clockwise from the "a" axis by a few degrees and the major axis is much greater than the minor axis (the ratio of the major to the minor axis is much greater than that shown by figure 3.5). The reason for this 'tilt' can be understood by considering the fact that experimental  $T(X)$  values for a given branch fall almost on a straight line with intercept  $a_0$  and slope  $b_0$ . If an attempt is made to fit the data to another straight line for which the time intercept  $a > a_0$  is fixed, the resulting value of the slope,  $b$ , will be such that  $b < b_0$ . Similarly if  $a < a_0$  then  $b > b_0$ . Also, the ellipsoid defined by (3.28) is such that when  $c$  increases the allowable values of  $b$  decrease. These properties of the solution space are not accidental; they are related to the stability of the function  $\tau(p)$ . For example, consider figure 3.5 and assume, for simplicity, that  $c = 0$ . For any  $(a,b)$  within the ellipse we have from the mean square error in (3.25) that  $\tau(p) = a$  where  $p = b$ . Because of the tilt of the major axis of the ellipse, points with higher  $b$  values have lower  $a$  values; this situation is in accordance with the monotonic decreasing behaviour of  $\tau(p)$ . Also, since the ellipsoid encompasses smaller  $b$  values for larger  $c$

Figure 3.5

Typical error ellipse in the (a,b) plane for  $T = a + bX + cX^2$  type parameterization of travel-time branches.





values, the tendency is toward preservation of the range of  $p$  defined by (3.25) when  $c$  changes.

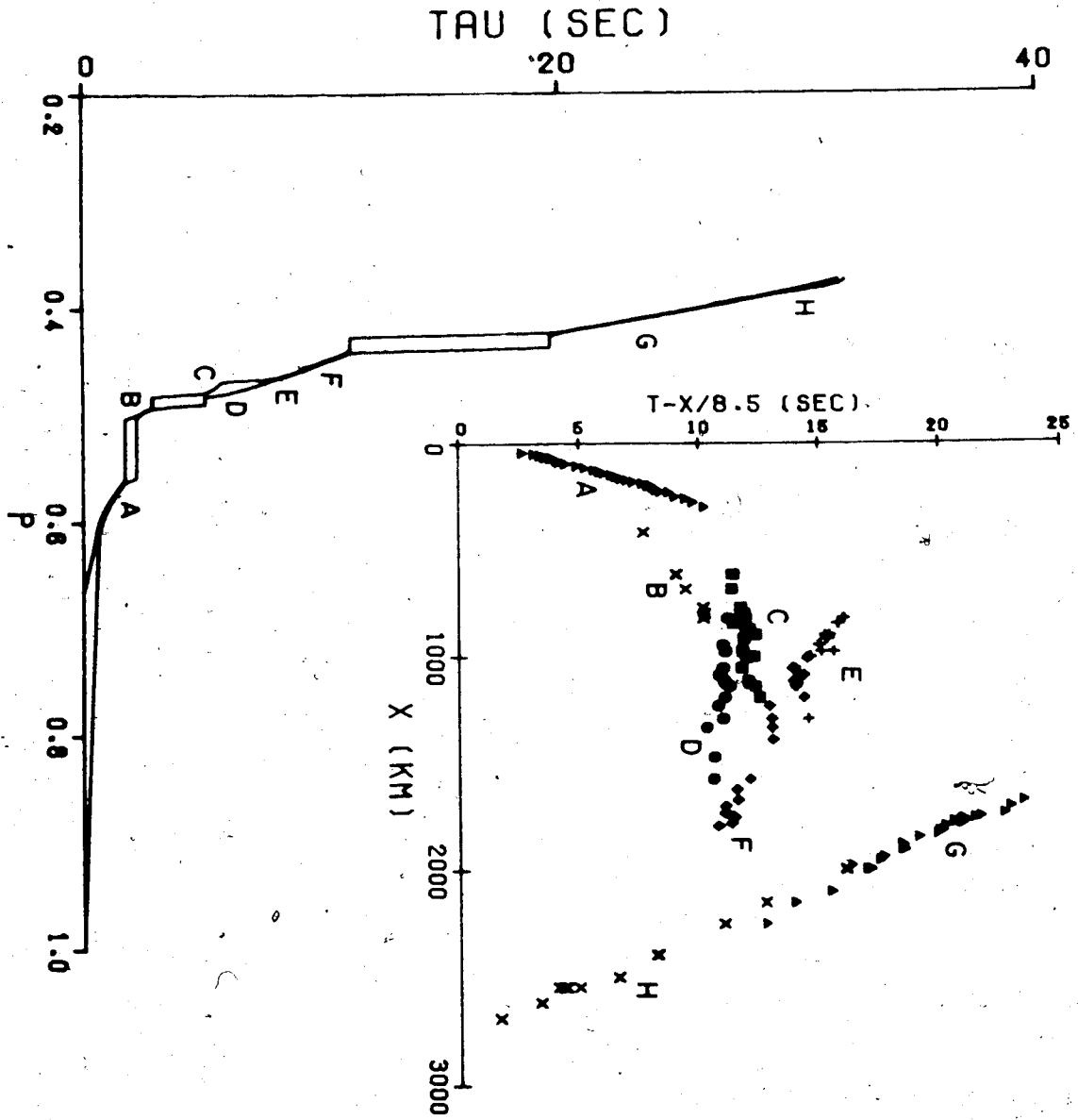
In order to find all possible expressions of the  $T(X)$  branch in the  $\tau(p)$  plane for a given error  $\xi E_0$ , we need only calculate  $\tau(p)$  from (3.25) for points  $(a, b, c)$  on the surface of the ellipsoid defined by (3.28). The image curve  $\tau(p)$  of any interior point  $(a, b, c)$  will be 'contained' by the image curves of the surface points. This fact can be seen by considering the dashed line in figure 3.5; from (3.25) the images  $\tau(p)$  of points on the dashed line have the same  $p$  range and if  $\tau_1(p)$  and  $\tau_2(p)$  result from the two endpoints then  $\tau_1(p) < \tau_{int}(p) < \tau_2(p)$  where  $\tau_{int}(p)$  is the image of any point between the endpoints. The procedure then is to calculate  $\tau(p)$  from (3.24) for discrete points on the boundary of each ellipse corresponding to discrete values of  $c$  between  $c_{min}$  and  $c_{max}$ . With the solution space defined by (3.28) we can calculate all possible  $\tau(p)$  expressions of every  $T(X)$  branch for any root mean square error. An envelope in the  $\tau(p)$  plane can be determined by examining all possible solutions. Finally this envelope may be mapped into an envelope in the  $V(Z)$  plane by using the technique described by Bessonova et al (1974).

### Results from Project Early Rise

The travel-time branches recorded in Western Canada from shots in Lake Superior along the 'Yukon' line during Project Early Rise together with the resulting  $\tau(p)$  envelope are shown in figure 3.6. The  $p$  axis of the  $\tau(p)$  plane has been normalized to a surface velocity of 4 km/sec. The letters indicate the location of branches in the  $\tau(p)$  plane. Each travel-time branch was fitted to a best fit curve of the form given by (3.24); the uncertainty ellipsoid (equation 3.28) in  $(a,b,c)$  space for each branch was then determined for a value of  $\xi = \sqrt{2}$ . The upper and lower  $\tau(p)$  bounds for each branch were determined by sampling the surface of the error ellipsoid; the  $p$  range was restricted to the region defined by the best fit curve (3.24). With the  $\tau(p)$  bounds determined for each branch in this manner it was found that the  $\tau(p)$  regions for various pairs of travel-time branches blend into one another; thus the  $\tau(p)$  images of branches C and D have a small common region along the  $p$  axis, as do the images from the pair E,F and the pair G,H. The pieces of  $\tau(p)$  envelope with common regions mentioned blend into one another quite smoothly and therefore it was not difficult to form the 'composite'  $\tau(p)$  upper and lower bounds in the intersecting  $p$  regions. This phenomenon of blending in the  $\tau(p)$  plane is not surprising in view of the fact that the travel-time branch pairs involved

Figure 3.6

The insert on the upper right-hand corner shows the travel-time branches for the Yukon line recorded during Project Early Rise. The main diagram shows the Tau envelope for this data. The letters indicate location of branches in the  $\tau(p)$  plane.



do in fact converge in the T-X plane. Now there is also a region in the  $\tau(p)$  plane for which the p regions of two branches overlap but for which the values of  $\tau$  for the overlapping p interval are offset; this jump in  $\tau(p)$  is indicative of a low velocity zone. The  $\tau(p)$  envelopes resulting from branches D and E have a common p region defined by  $0.465 \leq p \leq 0.478$ . The maximum jump in  $\tau(p)$  within this interval is defined by the maximum of the difference between the upper  $\tau(p)$  bound for branch E and the lower  $\tau(p)$  bound for branch D; the value is approximately 1.9 seconds. Similarly the minimum jump in  $\tau(p)$  in this p interval (the minimum of the difference between the lower  $\tau(p)$  bound for branch E and the upper  $\tau(p)$  bound for branch D) is approximately 1.1 seconds. Thus the parameters which define the low velocity zone kinematically are  $\underline{q}_1 = 0.465$ ,  $\bar{q}_1 = 0.478$ ,  $\underline{\sigma}_1 = 1.1$  sec, and  $\bar{\sigma}_1 = 1.9$  sec. Now the  $\tau(p)$  envelope for p regions between the images of the individual branches has been constructed using the fact that  $\tau(p)$  is a monotonic decreasing function. Notice that the  $\tau(p)$  envelope in these gap regions is responsible for the major uncertainty (that is the  $\tau(p)$  envelope is widest for p intervals between branches A and B, B and C, and F and G). Note also that, of the rays observed, those having the least depth of penetration constitute branch A. Thus  $\tau(p)$  data 'commences' at a p value of about 0.61 and there

are no observations for the range  $0.61 < p \leq 1.0$ . The extent of this interval may seem overwhelming but it is rather artificial in view of the assignment of the generous value (4.0 km/sec) for the surface velocity. The  $\tau(p)$  envelope in this region has been constructed by linear interpolation between the existing point  $\tau_U(0.61)$  and  $\tau(1.0) = 0$  for the upper bound and linear extrapolation between the existing point  $\tau_L(0.61)$  and the point  $\tau(0.66) = 0$  (note that the value of  $p = 0.66$  corresponds to a surface velocity of 6 km/sec) for the lower bound. It has been mentioned that the  $p$  range of each branch in the  $\tau(p)$  plane has been dictated by the values of  $b = b_0$  and  $c = c_0$  (that is the coefficients describing the best fit curve of the form (3.24)). It is worth noting that if any other values of 'b' and 'c' within the error ellipsoids are taken then the resulting image  $\tau(p)$  curves essentially fall within the  $\tau(p)$  envelope shown in figure 3.6; any points which fall outside the  $\tau(p)$  bounds shown are so close to the boundary that they are insignificant.

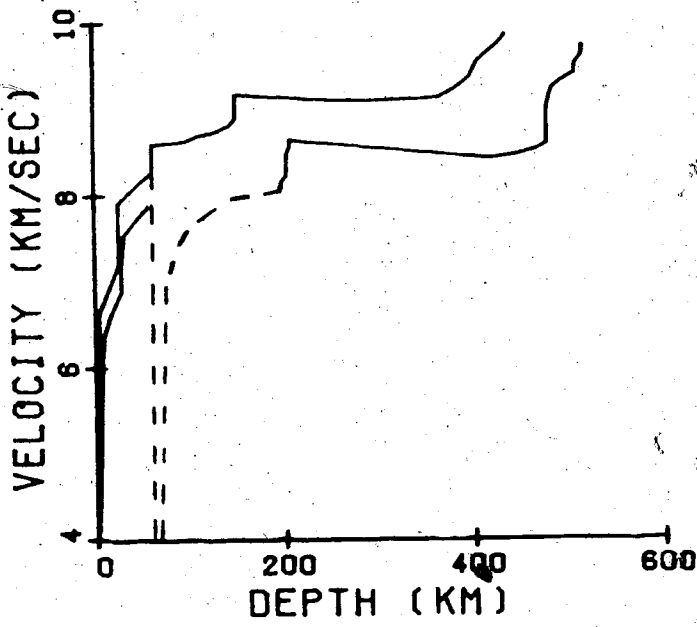
The  $\tau(p)$  envelope in figure 3.6 has been inverted using the Bessonova et al (1974) method described in the preceding section. A low velocity zone with parameters  $q_1, \bar{q}_1, \underline{q}_1$  and  $\bar{c}_1$  specified above has been assumed. The resulting velocity-depth envelope is shown in figures 3.7(a) and 3.7(b). The darkened region in figure 3.7(a)

Figure 3.7

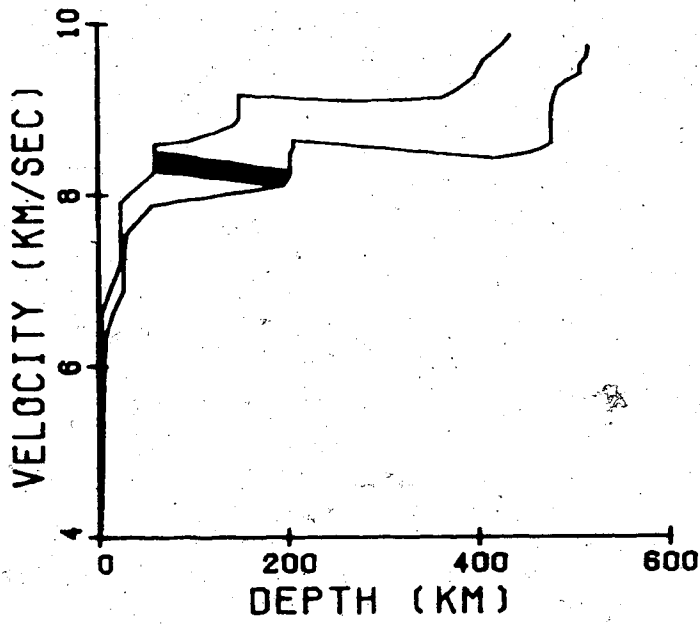
Velocity bounds for the Yukon line  $\tau(p)$  bounds.

In part (a) the darkened region is a barrier such that no velocity-depth curve may pass entirely through it without first exhibiting a low velocity zone. The dashed lines in part (b) outline possible low velocity zone configurations when the top of the low velocity zone is assumed to be at a depth of 60 km.





(b)



(a)

is a 'barrier' associated with the low velocity zone.

The darkened region has the following properties:

(i) No velocity-depth curve may pass entirely through it without first describing a low velocity zone.

(ii) The low velocity zone must commence at some 'valid' point which is contained within the darkened region. The low velocity zone has a magnitude defined by  $\sigma$ , where  $\underline{\sigma}_1 \leq \sigma \leq \bar{\sigma}_1$ . Now in the inversion it was implicitly assumed that the maximum (flat earth) slowness attained in the low velocity zone was  $p = 1.0$ . This slowness corresponds to a spherical earth velocity of approximately 4.0 km/sec for the depth shown. In view of this minimum bound (4.0 km/sec) for the velocity within the waveguide it is clear that for any allowable value of  $\sigma$  there will be points within the darkened region which are so deep that it is impossible to construct the corresponding waveguide commencing at these points. Any point within the darkened region from which it is possible to construct the low velocity zone for  $\sigma \geq \underline{\sigma}_1$  is a 'valid' point.

Figure 3.7(a) shows that the top of the low velocity zone may be as shallow as 60 km, and also that the waveguide may be as thick as about 150 km (in this case the difference between the velocity within the waveguide and the velocity at the top of the waveguide is infinitesimal). Figure 3.7(b) illustrates the low velocity zone

configuration for  $\sigma = \bar{\sigma}_1$  when the top of the waveguide is at a depth of 60 km and the velocity at the top of the waveguide is about 8.3 km/sec. The differences in depth between the upper and lower dashed lines is approximately the thickness of the low velocity zone as a function of the velocity within the zone. This relationship is true if it is assumed that the 'flat earth' waveguide is rectangular in which case the corresponding spherical earth waveguide (equation 3.2) is approximately rectangular. The low velocity zone configuration for  $\sigma = \underline{\sigma}_1$  is very close to that for  $\sigma = \bar{\sigma}_1$  and thus dashed curves similar to those in figure 3.7(b) for the case  $\sigma = \underline{\sigma}_1$  are not shown. If we consider a velocity model which lies midway between the upper and lower bounds shown in figure 3.7 then the 'form' of the bounds suggests a crustal thickness of about 30 km, a rapid increase in velocity near about 170 km depth (as the velocity curve exits the low velocity zone), and another rapid increase in velocity near about 420 km. The presence of the upper mantle structures is not a new phenomena. Indeed continental P wave studies which reveal the asthenospheric low velocity layer, a high velocity gradient immediately beneath the low velocity zone and a high velocity gradient near about 420 km depth include those of Lukk and Nersesov (1965), Niazi and Anderson (1965), Johnson (1967), Julian and Anderson (1968), Green and Hales (1968), Archambeau

et al (1969), Helmberger and Wiggins (1971), Hales (1972), McMechan and Wiggins (1972), Wiggins and Helmberger (1973), Massé (1973), and Massé and Alexander (1974).

In addition the P wave travel time data of Dowling and Nuttli (1964) and Hill (1972) indicated an asthenospheric low velocity zone; high velocity gradients near 420 km were reported by Golenetski and Medvedeva (1965), Barr (1967), Lewis and Meyer (1968) and Mereu et al (1974) on the basis of continental P wave travel times. It is of particular importance that this study has revealed a well developed low velocity zone associated with a stable platform region. The low velocity zones detected in the majority of the studies cited above are associated with tectonically active regions. Some studies, however, suggest that associated with the asthenosphere underlying the stable central and eastern United States there is a P wave low velocity zone which is albeit not as pronounced as the one underlying the tectonically active western United States. Thus Hales (1972) cites the presence of a low velocity zone of large magnitude in the western United States and one of lesser magnitude in the central and eastern United States. Also Dowling and Nuttli (1964) find differences between the low velocity zone structures in the western and eastern United States; they state that the top of the low velocity zone is at a depth of about 70 km in the west and about 125 km in the east. Massé

(1973) studied travel time data from various lines of Project Early Rise and found a low velocity zone in the depth range 94 to 107 km with an average velocity of 8 km/sec (which is about 0.4 km/sec smaller than the velocity at the top of the low velocity channel) in the central and eastern United States. The parameters (depth and magnitude) of the low velocity zone described by Massé (1973) agree very favourably with results from this study (figure 3.7). Furthermore Massé and Alexander (1974) concluded that the upper mantle P velocity beneath Scandinavia and Western Russia closely resembles the model derived by Massé (1973) for the central and eastern United States. Thus this study and other studies have revealed the presence of substantial low velocity zones associated with the asthenosphere underlying stable platform type regions. This fact lends credence to the prediction and tenets of Hales (1972) who states "... I hazard the guess that further study will show that the low-velocity zone is a general and required feature of the upper mantle... it is quite clear that the relative motions of the outer part of the earth, which may now be regarded as established beyond reasonable doubt, do not take place only in tectonically active areas."

Now it is very interesting to compare the results of this experiment with the results of various other refraction surveys conducted in North America. A comparison

of results in the velocity-depth plane could be misleading since in past various authors have used a variety of inversion techniques. It is felt that the  $\tau(p)$  plane offers the most unbiased basis for comparison of the kinematic properties of crustal and upper mantle P waves which traverse various regions of the North American continent. Iyer et al (1969) list the travel times and distances for travel-time branches from Project Early Rise refraction lines. For the purpose of comparison with this experiment, these travel-time branches were fitted to best fit curves of the form (3.24); the corresponding best fit  $\tau(p)$  curves were then determined using equation (3.26). The lines used and the approximate distance ranges of the travel-time branches considered are as follows: Chapleau, Ontario to Chibougamau, Quebec (510 to 1080 km), Chibougamau, Quebec to Glace Bay, Nova Scotia (1100 to 2040 km), Saint Cloud, Minnesota to Holyoke, Colorado (440 to 1330 km), Bemidji, Minnesota to Miles City, Montana (370 to 1280 km), Dymont, Ontario to Sheho, Saskatchewan (620 to 1110 km), Leduc, Alberta to Post 140, British Columbia (2150 to 2490 km), Fort Nelson to Post 750, British Columbia (2540 to 2680 km), Flin Flon, Manitoba to Yellowknife, Northwest Territories (1380 to 2310 km), Bear Lake, Michigan to Potters Hill, North Carolina (40 to 1680 km), Lake Superior, Michigan to Eldorado, Arkansas (440 to 1430 km), Lake Superior, Michigan to Cornstock,

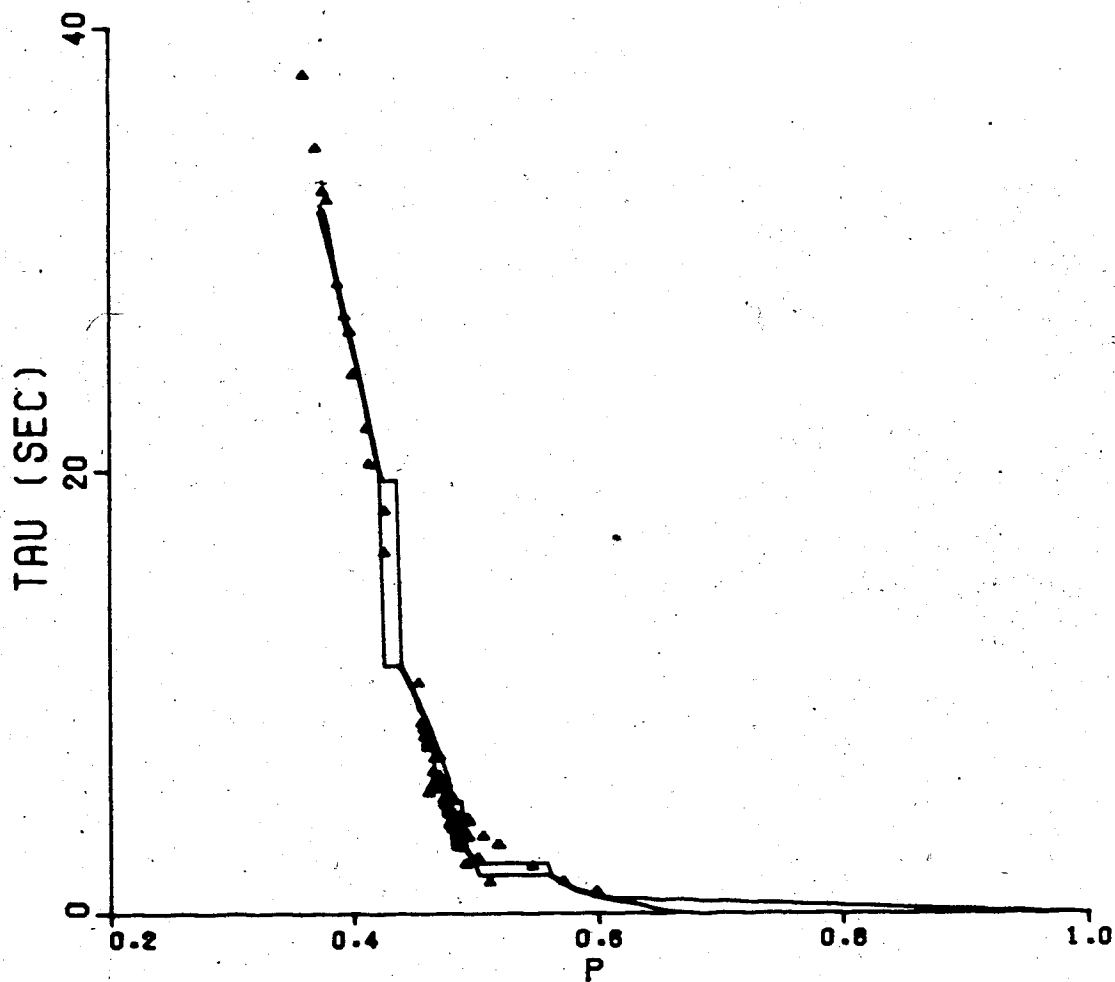
Texas (170 to 2250 km), Colorado Springs, Colorado to Charleston, West Virginia (1110 to 1620 km), Chapleau, Ontario to Chibougamau, Quebec to Schefferville, Quebec (460 to 1700 km), South Eastern Ontario (300 to 700 km), Lake Nipigon to Smooth Rock Falls, Ontario (240 to 610 km), Port Arthur, Ontario to Baralzon Lake, Manitoba (300 to 1490 km), Bemidji, Minnesota to Vancouver, British Columbia (470 to 2600 km), and from Lake Superior to the LRSM stations (500 to 3480 km). Thus the data set samples central and eastern North American regions and the distance ranges include those of this experiment. Points on the best fit  $\tau(p)$  curves for the travel-time data mentioned above are shown in figure 3.8 together with the  $\tau(p)$  envelope derived from the 'Yukon' line of this experiment. The agreement between the  $\tau(p)$  points from the various lines and the  $\tau(p)$  envelope shown is quite remarkable; with the slowness scale of figure 3.8 adjusted with  $p = 1$  corresponding to an apparent velocity of 4.0 km/sec it can be seen that the maximum departures in apparent velocity of points from the envelope boundaries are about 0.4 km/sec near 8 km/sec, 0.2 km/sec near 8.4 km/sec and about 0.2 km/sec near 9.6 km/sec.

Now let us consider North American seismic refraction data which have been interpreted by various authors; in particular we shall again examine results in the  $\tau(p)$  plane. Not all published reports list data from which

Figure 3.8

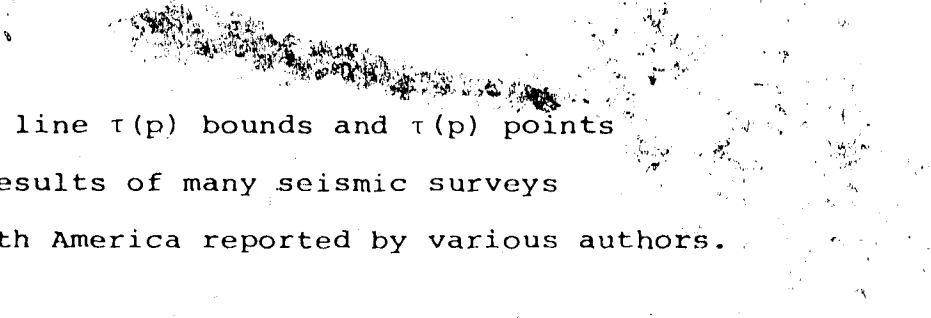
The Yukon line  $\tau(p)$  envelope with  $\tau(p)$  points based upon the Project Early Rise travel times listed by Iyer et al (1969).



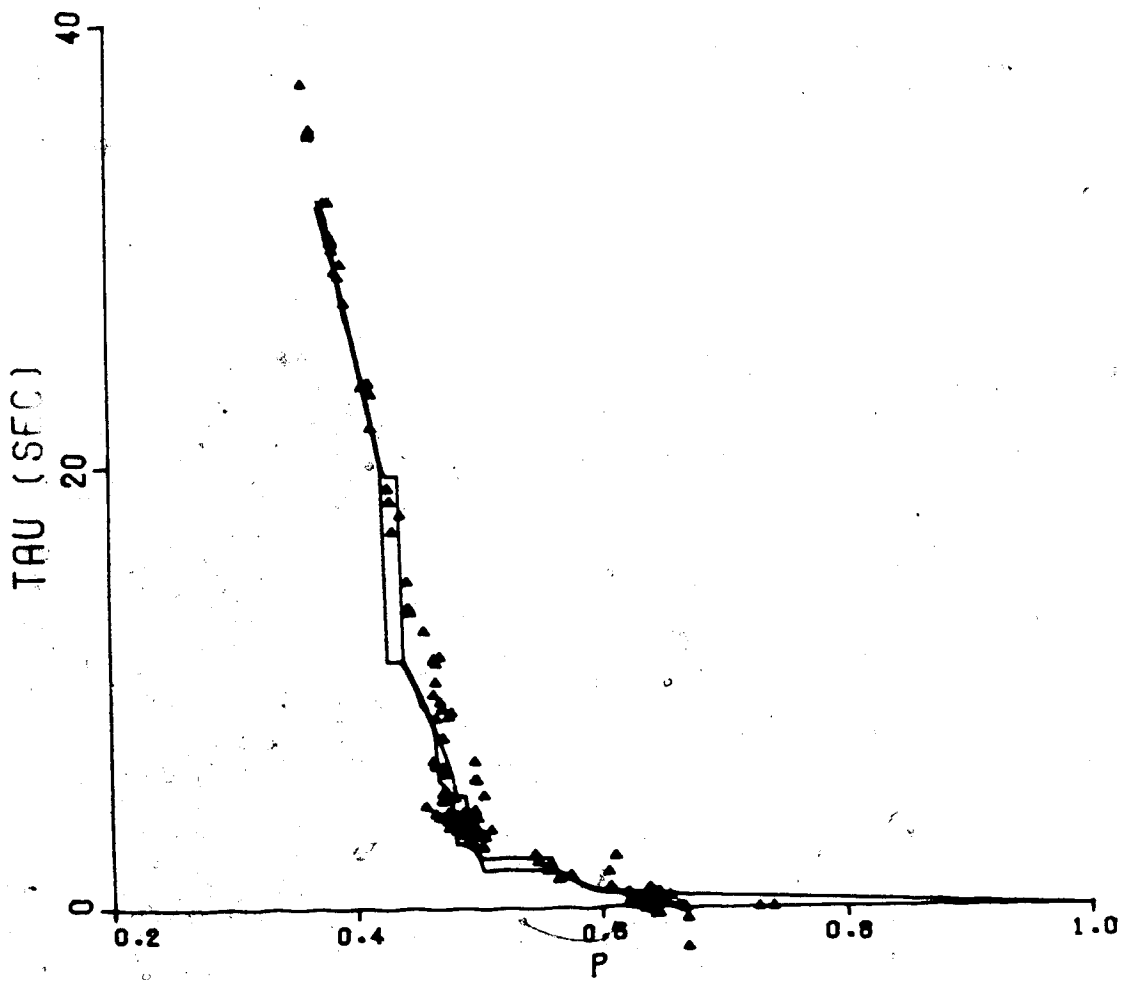


$\tau(p)$  information can be conveniently extracted but it is felt that the following studies taken collectively provide a reliable overview of interpreted North American seismic refraction surveys; the authors and the geographical areas studied are Dowling and Nuttli (1964) - eastern and western United States, Roller and Jackson (1966) - central United States, Hobson et al (1967) - Hudson Bay, Barr (1967) - Canadian Shield, Ruffman and Keen (1967) - Hudson Bay, Green and Hales (1968) - central United States, Lewis and Meyer (1968) - central United States, Gurbuz (1970) - central Canada, Mereu and Jobidon - eastern Canada, Hill (1972) - western United States, McMechan and Wiggins (1972) - western United States, Berry and Fuchs (1973) - north eastern canadian Shield, Massé (1973) - central and eastern North America, Wiggins and Helmberger (1973) - western United States, and Massé (1974) - central and eastern North America. Points in the  $\tau(p)$  plane from these studies are shown collectively in figure 3.9 together with the  $\tau(p)$  envelope from this experiment. Unlike the  $\tau(p)$  points due to the travel-time listings of Iyer et al (1969) (figure 3.8), there are several points which diverge considerably from the  $\tau(p)$  envelope in figure 3.9. There are two major reasons for this disparity. Firstly the physically 'impossible' negative values of  $\tau(p)$  in the  $p$  range of about 0. to 0.67 (apparent velocities from about 6.0 to 6.5 km/sec)

Figure 3.9



The Yukon line  $\tau(p)$  bounds and  $\tau(p)$  points based upon the results of many seismic surveys conducted in North America reported by various authors.



are a result of the Hudson Bay observations of Hobson et al (1967) and Ruffman and Keen (1967). The combined effects of a lateral inhomogeneous Hudson Bay crustal structure and inconsistent navigation can cause this discrepancy (indeed Ruffman and Keen (1967) examined the consistency of three possible navigation series). The second and more interesting reason for the disparity is that the data set shown in figure 3.9 is composite, being due not only to surveys conducted in central and eastern North America but also to studies applicable to the tectonically active western United States regions. Anomalously large  $\tau(p)$  values ('anomalous' if compared to the  $\tau(p)$  envelope) near  $p = 0.61$  (apparent velocity = 6.6 km/sec) and in the  $p$  range of about 0.46 to 0.51 (apparent velocities of about 7.8 to 8.7 km/sec) are due to the western United States investigations of McMechan and Wiggins (1972), Wiggins and Helmberger (1973), Hill (1972), and data from the western United States line studied by Dowling and Nuttli (1964) (Dowling and Nuttli (1964) also discussed results from the central, eastern, and southern United States and the  $\tau(p)$  data from these areas fall within the  $\tau(p)$  envelope or close to the boundary). The difference in kinematic properties between rays which traverse the tectonically active western United States and those which traverse the most stable regions of central and eastern North American regions is not

surprising. Although a determination of an exact velocity-depth function requires complete specification of  $\tau(p)$  it can be stated that the high  $\tau(p)$  values for the western United States in the  $p$  range of about 0.46 to 0.51 (figure 3.9) are consistent with 'overall' lower velocities in that tectonically active region as compared with the upper mantle velocity of the central and eastern portions of North America; thus rays which propagate through a higher magnitude low velocity zone and bottom just below it will suffer larger delay times and thus larger  $\tau(p)$  will result. Other points which lie far from the  $\tau(p)$  envelope in figure 3.9 are located near  $p \approx 0.47$  and  $\tau \approx 4$  sec; here the low  $p$  values as compared with the  $\tau(p)$  envelope are due to the study of Berry and Fuchs (1973) (some of their points also fall within the  $\tau(p)$  bounds). The spread in  $p$  values of the  $\tau(p)$  due to Berry and Fuchs (1973) is not surprising since the survey area included various lines crossing a large gravity anomaly associated with the Superior-Churchill province boundary in the northeastern Canadian Shield. Finally it is emphasized that the  $\tau(p)$  points in figures 3.8 and 3.9 which are applicable to central and eastern North America fall within the  $\tau(p)$  envelope or very close to the boundaries. Also deviations of the  $\tau(p)$  points from the envelope and the spread in  $p$  values of the  $\tau(p)$  points in figures 3.8 and 3.9 become less

pronounced as  $p$  decreases indicating that the upper mantle structures of the various regions sampled tend to coalesce with depth. Figures 3.8 and 3.9 also show  $\tau(p)$  points for rays which have bottomed at greater depths than those of this study. It is not intended that the comparisons discussed here constitute an exhaustive analysis of all refraction surveys ever conducted in North America but rather it is hoped that the discussion illustrates the importance of the  $\tau(p)$  plane.

A final point regarding the width of the velocity-depth envelope in figure 3.7 is worth mentioning. It can be seen from figure 3.6 that the slowness extent of the  $\tau(p)$  envelope for  $\tau(p)$  values from about 12 to 19 seconds is about  $\Delta p \approx 0.13$  which corresponds to an uncertainty in apparent velocity of about 0.4 km/sec. On the other hand the velocity envelope in figure 3.7 defines a velocity uncertainty of about 0.6 km/sec in the corresponding depth range of about 200 to 360 km. The velocity-depth boundaries shown in figure 3.7 define a rather large velocity uncertainty partly because the corresponding  $\tau(p)$  envelope bounds a finite area (we do not know  $\tau(p)$  exactly) and partly because the inversion scheme described in preceding sections does not yield greatest upper and least lower velocity depth bounds corresponding to given  $\tau(p)$  bounds. In view of the nature

5

of travel-time observations (observations are incomplete and in particular it is difficult to extract seismic signals which correspond to rays bottoming in regions of low velocity gradient from the seismogram) the inversion technique described cannot yield detailed velocity depth information. It is hoped that in future the extension of the Tau method to a Tau inversion method which incorporates partially reflected and converted phase will tend to alleviate this problem. The consideration of amplitude characteristics should also result in narrower velocity depth bounds; for example, McMechan and Wiggins (1973) used the Cagniard-de Hoop technique in conjunction with a Herglotz-Wiechert type extremal inversion scheme to construct models of the P wave structure for the upper mantle. Also Bessonova et al (1976) have described a Tau inversion method which yields more accurate velocity depth bounds than the one reported by Bessonova et al (1974). There is a further complication however - and that is the effect of lateral inhomogeneities on travel times, amplitudes, and the vector ray parameter in studies of the upper and lower mantle and the core of the earth. Possibly future two dimension array studies in conjunction with the above mentioned techniques will increase our knowledge of the detailed structure of the earth.



## Conclusions

Not only is the Tau method an objective approach to the problem of inversion of real seismic  $T(X)$  data but also it may be used to examine the variation of uncertainty of the velocity depth function due to changes in seismic array geometries. In the case of real seismic data, estimation of the function  $\tau(p)$  from  $T(X)$  can be performed satisfactorily using the 'Clairaut' approach as long as errors in  $T(X)$  are inconsequential. With realistic scatter, due to inhomogeneities or errors in measurement as is the case for long range refraction work, it becomes necessary to smooth the  $T(X)$  data in order to derive a meaningful velocity structure. An unbiased method of smoothing involves a determination of all possible curves,  $T = a + bX + cX^2$ , that fit each  $T(X)$  branch within any prescribed root mean square error. The solutions  $(a, b, c)$  are found to be contained within an ellipsoid in  $(a, b, c)$  space. The properties of the ellipsoid, for real data, reflect the inherent stability of the function  $\tau(p)$ .

Application of the Tau method of inversion to travel-time data applicable to western Canada indicates a crustal and upper mantle P wave velocity structure which consists of a crust approximately 30 km thick, a low velocity zone between depths of about 60 and 210 km, and rapid increases in velocity near 170 and 420 km.

A comparison of the  $\tau(p)$  bounds derived for western Canada with  $\tau(p)$  points associated with other regions of North America reflect crustal and upper mantle lateral inhomogeneities.

#### REFERENCES

- Adams, I.H., and Williamson, 1923. The composition of the earth's interior. *Smithsonian Rep.*, pp.241-260.
- Aki, K., Christofferson, A., and Husebye, E.S., 1976. Three-dimensional seismic structure of the lithosphere under Montana, *LASA, B.S.S.A.*, 66, pp. 501-524.
- Archambeau, C.B., Flinn, E.A., and Lambert, D.G., 1969. Fine structure of the upper mantle, *J.G.R.*, 74, pp. 5825-5865.
- Backus, G., and Gilbert, F., 1970. Uniqueness in the inversion of inaccurate gross earth data, *Phil. Trans. R. Soc. Lond.*, A266, 123-192.
- Barr, K.G., 1967. Upper mantle structure in Canada from seismic observations using chemical explosions, *C.J.E.S.*, 4, pp. 961-975.
- Berry, M.J., and Fuchs, K., 1973. Crustal structure of the Superior and Grenville Provinces of the Northeastern Canadian Shield, *B.S.S.A.*, 63, pp. 1393-1432.
- Berteussen, K.A., 1976. The origin of slowness and azimuth anomalies at large arrays, *B.S.S.A.*, 66, pp. 719-741.
- Bessonova, E.N., Fishman, V.M., Ryaboyi, V.Z., and Sitnikova, G.A., 1974. The Tau method for

- inversion of travel times - I. Deep seismic sounding data, *Geophys. J.R. astr. Soc.*, 36, pp. 377-398.
- Bessonova, E.N., Fishman, V.M., Johnson, L.R., Shnirman, M.G., and Sitnikova, G.A., 1976. The Tau method for inversion of travel times - II. Earthquake data, submitted.
- Birtill, J.W., and Whiteway, F.E., 1965. The application of phased arrays to the analysis of seismic body waves, *Phil. Trans. Roy. Soc. A.*, 258, pp. 421-492.
- Brown, R.J., 1973. Slowness and azimuth at the Uppsala array, Part 2: Structural Studies, *Pageoph.*, 109, pp. 1623-1637.
- Bugayevskii, G.N., 1964. Travel-time curve of seismic waves and structure of the mantle, *Izv. sib. Otdel. Akad. Nauk. SSSR*, 18, pp. 151-168.
- Bullen, K.E., 1963. *An Introduction to the Theory of Seismology*, Cambridge University Press, Cambridge.
- Capon, J., 1974. Characteristics of crust and upper mantle structure under LASA as a random medium, *B.S.S.A.*, 64, pp. 235-300.
- Carder, D.S., 1964. Travel times from central Pacific nuclear explosions and inferred mantle structure, *B.S.S.A.*, 54, pp. 2271-2294.

- Chinnery, M.A., and Toksoz, M.N., 1967. P-wave velocities in the mantle below 700 km, B.S.S.A., 57, pp. 119-226.
- Chinnery, M.A., 1969. Velocity anomalies in the lower mantle, Phys. Earth Planet. Interiors, 2, pp.1-10.
- Corbishley, D.J., 1970. Multiple array measurements of the P-wave travel-time derivative, Geophys. J.R. astr. Soc., 14, pp. 1-14.
- Davies, D., Kelly, E.J., and Filson, J.R., 1971. Vespa process for analysis of seismic signals, Nature, 232, pp. 8-13.
- Davies, D., and Sheppard, R.M., 1972. Lateral heterogeneity in the earth's mantle, Nature, 239, pp. 318-323.
- Davies, L.M., and Chapman, C.H., 1975. Some numerical experiments on the inversion of discrete travel-time data, B.S.S.A., 65, pp. 531-539.
- Doornbos, D.J., and Husebye, E.S., 1972. Array analysis of PKP phases and their precursors, Phys. Earth Planet. Interiors, 5, pp. 387-399.
- Dowling, J., and Nuttli, O., 1964. Travel-time curves for a low-velocity channel in the upper mantle, B.S.S.A., 54, pp. 1981-1996.
- Engdahl, E.R., and Felix, C.P., 1971. Nature of travel-time anomalies at LASA, J.G.R., 76, pp. 2706-2715
- Forsythe, G., and Moler, C.B., 1967. Computer solutions of linear algebraic equations, Prentice-Hall, Inc.,

- Englewood Cliffs, New Jersey, 148.pp.
- Franklin, J.N., 1968. Matric theory, Prentice-Hall INC., Englewood Cliffs, New Jersey 292 pp.
- Gerver, M., and Markushevitch, V., 1966. Determination of seismic wave velocity from the travel-time curve, Geophys. J.R. astro. Soc., 11, pp. 165-173.
- Gerver, M., and Markushevitch, V.M., 1972. Determining seismic-wave velocity from travel-time curves, in Computational Seismology edited by V.I. Keilis-Borok, Consultants Bureau, New York-London, pp. 123-147.
- Golenetskii, S.I., and Medvedeva, G.Ya., 1965. On discontinuities of the first kind in the earth's upper mantle, Izv. Earth Phys. Ser. No. 5, pp. 57-62.
- Golub, G., and Kahan, W., 1964. Calculating the singular values and pseudo-inverse of a matrix, Technical Report CS8, Computer Science Division, School of Humanities and Sciences, Stanford University.
- Gopalakrishnan, B.S., 1969. P wave velocities in the mantle below 700 kilometers, Geophys. J., 17, pp. 405-413.
- Green, A.G., 1975. On the postulated Hawaiian plume with emphasis on the limitations of seismic arrays for detecting deep mantle structure, J.G.R., 80, pp. 4028-2036.

- Green, R.W.E., and Hales, A.L., 1968. The travel-time of P waves to 30° in the central United States and upper mantle structure, B.S.S.A., 58, pp. 267-289.
- Gurbuz, M.B., 1970. A study of the earth's crust and upper mantle using travel times and spectrum characteristics of body waves, B.S.S.A., 60, pp. 1921-1935.
- Gutenberg, B., 1958. Velocity of seismic waves in the earth's mantle, Trans. Am. Geophys. Union, 39, pp. 486-489.
- Gutowski, P.R., 1974. Seismic array investigations of the upper and lower mantle, Ph.D. thesis, University of Alberta.
- Haddon, R.A.W., and Bullen, K.E., 1969. An earth model incorporating free earth oscillation data, Phys. Earth Planet. Interiors, 2, pp. 35-49.
- Hales, A.L., Cleary, J., and Roberts, J., 1968. Velocity distributions in the lower mantle, B.S.S.A., 58, pp. 1975-1989.
- Hales, A.L., 1972. The travel times of P seismic waves and their relevance to the upper mantle velocity distribution. In: A.R. Ritsema (Editor), The Upper Mantle, Tectonophysics, 13, pp. 447-482.
- Hales, A.L., and Herrin, E., 1972. Travel times of seismic waves, in The Nature of the Solid Earth, edited by E.C. Robertson, McGraw-Hill, pp.172-215.

- Helmberger, D., and Wiggins, R.A., 1971. Upper mantle structure of midwestern United States, J.G.R., 76, pp. 3229-3245.
- Herglotz, G., 1907. Über das benndorfsche problem der fortflanzungsgeshwindigkeit der erdbebenstrahlin, Phys. Z., 8, pp. 145-147.
- Hill, D.P., 1972. Crustal and upper mantle structure of the Columbia Plateau from long range seismic-refraction measurements, Geol. Soc. Am. Bull., 83, pp. 1639-1648.
- Hobson, G.D., Overton, A., Clay, D.N., and Thatcher, W., 1967. Crustal structure under Hudson Bay, C.J.E.S., 4, pp. 929-947.
- Iyer, H.M., Pakiser, L.C., Stuart, D.J., and Warren, D.H., 1969. Project Early Rise: Seismic probing of the upper mantle, J.G.R., 74, pp. 4409-4441.
- Iyer, H.M., 1971. Variations of apparent velocity of teleseismic P waves across the large-aperture seismic array, Montana, J.G.R., 76, pp.8554-8567.
- Johnson, L.R., 1967: Array measurements of P velocities in the upper mantle, J.G.R., 72, pp.6309-6325.
- Johnson, L.R., 1969. Array measurements of P velocities in the lower mantle, B.S.S.A., 59, pp. 973-1008.
- Jordan, T.H., and Lynn, W.S., 1974. A velocity anomaly in the lower mantle, J.G.R., 79, pp. 2679-2685.
- Julian, B.R., and Anderson, D.L., 1968. Travel-times, apparent velocities, and amplitudes of body waves, B.S.S.A., 58, pp. 339-366.



- B.S.S.A., 58, pp. 339-366.
- Julian, B.R., and Sengupta, M.K., 1973. Seismic travel time evidence for lateral inhomogeneity in the deep mantle, *Nature*, 242, pp. 443-447.
- Kanamori, H., 1967. Upper mantle structure from apparent velocities of P waves recorded at Wakayama micro-earthquake observatory, *Bull. Earthquake Res. Inst.* 45, pp. 657-678.
- Kanasewich, E.R., Siewert, W.P., Burke, M.D., McCloughan, C.H., and Ramsdell, L., 1974. Gain-ranging analog or digital seismic system, *B.S.S.A.*, 64, pp.103-113.
- Kanasewich, E.R., Ellis, R.M., Chapman, C.H., and Gutowski, P.R., 1973. Seismic array evidence of a core boundary source for the Hawaiian linear volcanic chain, *J.G.R.*, 78, pp. 1361-1371.
- Kanasewich, E.R., and Gutowski, P.R., 1975. Detailed seismic analysis of a lateral mantle inhomogeneity, *Earth and Planet. Sci. Letters*, 25, pp. 379-384.
- Kanasewich, E.R., 1975. *Time Sequence Analysis in Geophysics*, second edition, University of Alberta Press.
- Kennett, B.L.N., 1976. A comparison of travel-time inversions, *Geophys. J.R. astr. Soc.*, 44, pp. 517-536.
- Kulháněk, B., and Brown, R.J., 1974. P wave velocity anomalies in the earth's mantle from the Uppsala array observations, *Pageph*, 112, pp. 597-617.

- Lewis, B.T.R., and Meyer, R.P., 1968. A seismic investigation of the upper mantle to the west of Lake Superior, B.S.S.A., 58, pp. 565-596.
- Lukk, A.A., and Nersesov, I.L., 1965. Structure of the upper mantle as shown by observations of earthquakes of intermediate focal depth, Doklady Akad. Nauk., SSSR, Earth Sciences Section, 162, pp. 14-16.
- Mandee, E.B., and Weichert, D.H., 1968. Epicentral uncertainties and detection probabilities from the Yellowknife seismic array data, B.S.S.A., 58, pp. 1359-1377.
- Massé, R.P., 1973. Compressional velocity distribution beneath central and eastern North America, B.S.S.A., 63, pp. 911-935.
- Massé, R.P., and Alexander, S.S., 1974. Compressional velocity distribution beneath Scandinavia and western Russia, Geophys. J.R. astr. Soc., 39, pp. 587-602.
- Massé, R.P., 1974. Compressional velocity distribution beneath central and eastern North America in the depth range 450-800 km, Geophys. J.R. astr. Soc., 36, pp. 705-716.
- McMechan, G.A., and Wiggins, R.A., 1972. Depth limits in body wave inversion, Geophys. J.R. astro. Soc., 28, pp. 459-473.

Mereu, R.F., and Jobidon, G., 1971. A seismic investigation of the crust and Moho on a line perpendicular to the Grenville front, C.J.E.S., 8, pp. 1554-1583.

Mereu, R.F., Simpson, D.W., and King, D.W., 1974. Q and its effect on the observation of upper mantle travel-time branches, Earth and Planet. Sci. Letters, 21, pp. 439-447.

Naponen, J., 1974. Seismic ray direction anomalies caused by deep structure in Fennoscandia, B.S.S.A., 64, pp. 1931-1941.

Niazi, M., and Anderson, D.L., 1965. Upper mantle structure of western North America from apparent velocities of P waves, J.G.R., 70, pp. 4633-4640.

Niazi, M., 1966. Corrections to apparent azimuths and travel-time gradients for a dipping Mohorovicic discontinuity, B.S.S.A., 56, pp. 491-509.

Okal, E., and Kuster, G., 1975. A teleseismic array study in French Polynesia; Implications for distant and local structure, Geophys. Res. Letters, 2, pp. 5-8.

Otsuka, M., 1966. Azimuth and slowness anomalies of seismic waves measured on the Central California Seismographic Array, Part I. Observations, B.S.S.A., 56, pp. 223-239.

- Otsuka, M., 1966a. Azimuth and slowness anomalies of seismic waves measured on the central California seismographic array, Part II. Interpretation, B.S.S.A., 56, pp. 655-675.
- Powell, C., 1975. Evidence for mantle heterogeneity from two large seismic arrays, *Nature*, 254, pp. 40-42.
- Roller, J.C., and Jackson, W.H., 1966. Seismic wave propagation in the upper mantle: Lake Superior, Wisconsin to Central Arizona, *J.G.R.*, 71, pp. 5933-5941.
- Ruffman, A., and Keen, M.J., 1967. A time-term analysis of the first arrival data from the seismic experiment in Hudson Bay, *C.J.E.S.*, 4, pp. 901-928.
- Schneider, W.A., and Backus, M.M., 1968. Dynamic correlation analysis, *Geophysics*, 33, pp. 105-126.
- Sengupta, M.K., and Toksoz, M.N., 1976. Three dimensional model of seismic velocity variation in the earth's mantle, *Geophys. Res. Letters*, 3, pp. 84-86.
- Taner, M.T., and Koehler, F., 1969. Velocity spectral-digital computer derivation and application of velocity functions, *Geophysics*, 34, pp. 859-881.
- Toksoz, M.N., Chinnery, M.A., and Anderson, D.L., 1967. Inhomogeneities in the earth's mantle, *Geophys. J.R. astr. Soc.*, 13, pp. 31-59.

- Vinnik, L.P., Lukk, A.A., and Nikolaev, A.V., 1972. Inhomogeneities in the lower mantle, *Phys. Earth and Planet. Interiors*, 5, pp. 328-331.
- Vvedenskaya, A.V., and Balakina, L.M., 1959. Double refraction in the earth's mantle, *Izvestia Akad. Nauk SSSR, Geophys. Ser.*, 7, pp. 1138-1146.
- Weichert, D.H., Manchee, E.B., and Whitham, K., 1967. Digital experiments at twice real time speed on the capabilities of the Yellowknife seismic array, *Geophys. J.R. astr. Soc.*, 13, pp. 277-295.
- Weichert, D.H., 1972. Anomalous azimuths of P: Evidence for lateral variations in the deep mantle, *Earth and Planet. Sci. Letters*, 17, pp. 181-188.
- Wiechert, E., 1910. Bestimmung des weges der erdbebenwellen im erdinnern, I. Theoretisches Phys. Z., 11, pp. 294-304.
- Wiggins, R.A., and Helmberger, D.V., 1973. Upper mantle structure of the western United States, *J.G.R.*, 78, pp. 1870-1880.
- Wiggins, R.A., McMechan, G.A., and Toksoz, M.N., 1973. Range of earth structure nonuniqueness implied by body wave observations, *Revs. Geophys. and Space Phys.*, 11, pp. 87-113.
- Wilkinson, J.H., 1965, *The algebraic eigenvalue problem*: Oxford, Clarendon Press, pp. 662. |

- Wolfe, J.G., 1969.  $dT/d\Delta$  measurement of short period P waves in the upper mantle for western North America using LASA, M.S. thesis, 73 pp., Dept. of Earth Planet. Sci., Mass. Inst. of Technol., Cambridge.
- Wright, C., 1970. P wave travel time gradient measurements and lower mantle structure, Earth Planet. Sci. Letters, 8, pp. 41-44.
- Wright, C., and Cleary, J.R., 1972. P-wave travel-time gradient measurements for the Warramunga seismic array and lower mantle structure, Phys. Earth Planet. Interiors, 5, pp. 213-230.
- Wright, C., Cleary, J.R., and Muirhead, K.J., 1974. The effects of local structure and the adjacent upper mantle on short period P wave arrivals recorded at the Warramunga seismic array, Geophys. J., 295, pp. 295-319.
- Wright, C., and Lyons, J.A., 1975. Seismology,  $dT/d\Delta$ , and deep mantle convection, Geophys. J.R. astr. Soc., 40, pp. 115-138.
- Wu, F.T., and Allen, R.P., 1972. Research Note,  $dT/d\Delta$  measurements at Wesson Observatory, U.S.A., Geophys. J.R. astr. Soc., 26, pp. 537-543.
- Zengeni, T.G., 1970. A Note on an azimuthal correction for  $dT/d\Delta$  for a single dipping interface, B.S.S.A., 60, pp. 299-306.

## Appendix 1

A vector norm is a measure of the size, in some sense, of a vector. If  $\underline{x}$  is a vector then the most common vector norm is the Euclidean norm, giving the length of the vector,

$$||\underline{x}|| = \sqrt{\underline{x}^T \underline{x}}$$

Any vector norm has the following properties:

- (i)  $||c\underline{x}|| = |c| \cdot ||\underline{x}||$  for all real  $c$ .
- (ii)  $||\underline{x}|| > 0$  if  $\underline{x}$  is not a null vector.
- (iii)  $||\underline{x} + \underline{y}|| \leq ||\underline{x}|| + ||\underline{y}||$  for all vectors  $\underline{x}$  and  $\underline{y}$ .

The induced matrix norm,  $||A||$  of an  $n \times n$  matrix,  $A$ , is given by

$$||A|| = \max ||A\underline{x}|| \quad \text{where} \quad ||\underline{x}|| = 1,$$

In this equation  $\underline{x}$  has been normalized and for the Euclidean vector norm,  $||A||$  is called the 'spectral' matrix norm and is equal to the length of the longest vector in the image set  $\{A\underline{x}\}$  under the transformation  $\underline{x} \rightarrow A\underline{x}$ . Matrix norms satisfy the properties (i) to (iii) above. It is possible to show that the spectral norm  $||A||$  is equal to the maximum singular value of  $A$  (equivalently  $||A||^2$  is equal to the spectral radius,  $\rho(A^T A)$ , of the matrix  $A^T A$  which is the non-negative square root of the necessarily non-negative largest

eigenvalue of the matrix  $A^T A$ ). Another useful vector norm is the 'norm-infinity' vector norm defined by

$$\|\underline{x}\|_{\infty} = \max_{1 \leq i \leq N} |x_i|$$

where

$$\underline{x} = (x_1, x_2, \dots, x_N)^T.$$

The induced norm-infinity matrix norm is

$$\|A\|_{\infty} = \max_{1 \leq i \leq N} \sum_{j=1}^N |a_{ij}|$$

where

$$A = \{a_{ij}\}, \quad i, j = 1, \dots, N.$$

The 'condition number',  $\kappa(A)$ , of square non-singular matrix  $A$  is defined by  $\kappa(A) = \|A\| \cdot \|A^{-1}\|$ . Clearly the condition number depends upon the matrix norm which is chosen. Regardless of the matrix norm, however, it can be shown that  $\|I\| \leq \kappa(A) < \infty$ . For the spectral norm  $\kappa(A) = \mu_L / \mu_S$  where  $\mu_L$  and  $\mu_S$  are respectively the largest and smallest, necessarily positive, eigenvalues of the matrix  $AA^T$ . In general  $\kappa(A)$  is a measure of the stability of the inverse problem given by equation (1.2). Unstable systems are associated with large condition numbers and are termed 'ill-conditioned'.

A final point worth mentioning is that if  $\underline{y} = A\underline{x}$  then for any vector norm and associated induced matrix norm,

$$\|\underline{y}\| \leq \|A\| \|\underline{x}\|.$$



## Appendix 2

The analysis of diagonal matrix form under orthogonal equivalence is based upon the following theorem and discussion. If  $A$  is a real  $n \times n$  matrix then there exist two real  $n \times n$  orthogonal matrices  $U, V$  so that  $U^T A V$  is a diagonal matrix  $D$ ; furthermore we may choose  $U$  and  $V$  so that the diagonal elements of  $D$  are

$$\mu_1 \geq \mu_2 \geq \dots \geq \mu_r > \mu_{r+1} = \dots = \mu_n = 0,$$

where  $r$  is the rank of  $A$  and the numbers  $\mu_1, \dots, \mu_n$  are the singular values of  $A$ . Now consider  $A$  as representing a linear transformation of one  $n$ -dimensional space  $G$  into a second such space  $H$ . Thus  $\underline{h} = A\underline{g}$  is in  $H$  for any  $\underline{g}$  in  $G$ . Now effect an orthogonal change of coordinates in space  $G$  and a different orthogonal change in space  $H$  such that we have the new representations  $\underline{g} = V\underline{g}'$  and  $\underline{h} = U\underline{h}'$ . As a result of the changes of bases in  $G$  and  $H$  the transformation  $A$  obtains the simple representation of the matrix  $D$ . Thus we have  $\underline{h}' = D\underline{g}'$ . The transformation now simply maps the first coordinate axis of  $G$  onto the first coordinate axis of  $H$  with a magnification factor  $\mu_1 > 0$ . It does the same for the 2<sup>nd</sup>, 3<sup>rd</sup>, ...  $r$ <sup>th</sup> coordinate axes with magnification factors  $\mu_2, \dots, \mu_r$ . The  $(r+1)$ -th, ...,  $n$ -th coordinate axes of  $G$  are mapped onto the zero vector of  $H$ . The most important result for the purpose of applications to seismic arrays is that  $D$  maps

the unit hypersphere  $S = \{g' : \|g'\| = 1\}$  into an  $r$ -dimensional hyperellipsoid  $E = DS$  of vectors  $\underline{h}'$  such that

$$\frac{(h'_1)^2}{\mu_1} + \dots + \frac{(h'_r)^2}{\mu_r} \leq 1$$

### Appendix 3

#### Tau Inversion Program

The following computer program calculates velocity-depth limits for given  $\tau(p)$  limits using the algorithm given by Bessonova et al (1974). It is assumed that the  $\tau(p)$  limits are calculated from the normalized travel time,  $T'$ , and distance observations,  $X'$ , that is

$$T' = T/2$$

$$X' = X/2 \text{ VSUR}$$

where  $T(\text{sec})$  and  $X(\text{km})$  are the actual travel times and distances and  $\text{VSUR}(\text{km/sec})$  is the velocity at the surface of the earth. Thus

$$\tau(p) = T' - pX'$$

and

$$p = dT'/dX'$$

The upper and lower bounds  $\tau_U(p)$  and  $\tau_L(p)$  for the function  $\tau(p)$  are given in terms of piecewise second order polynomials in  $p$  and

MU = number of polynomials defining  $\tau_U(p)$

ML = number of polynomials defining  $\tau_L(p)$ .

For the function  $\tau_U(p)$ , the  $p$  axis is segmented by the values

$$PU(I), I = 1, NU$$

where

$$NU = MU + 1, \quad PU(1) = 1.0$$

and

$$PU(I+1) < PU(I) \quad \text{for all } I.$$

The function  $\tau_U(p)$  is then defined by,

$$\tau_U(p) = AU(I) + BU(I)p + CU(I)p^2 \quad \text{for } PU(I+1) \leq p \leq PU(I).$$

Similarly for the function  $\tau_L(p)$  the p axis is segmented by the values,

$$PL(I), I = 1, NL$$

where

$$NL = ML + 1, \quad PL(1) = 1.0$$

and

$$PL(I+1) < PL(I) \quad \text{for all } I.$$

The function  $\tau_L(p)$  is then defined by

$$\tau_L(p) = AL(I) + BL(I)p + CL(I)p^2 \quad \text{for } PL(I+1) \leq p \leq PL(I).$$

It is assumed that  $PU(NU) = PL(NL)$ . Now  $NLVZS$  is equal to the number of low velocity zones under consideration. The quantities  $QU(J)$  and  $QL(J)$ ,  $J = 1, \dots, NLVZS$  define the region of uncertainty along the p axis for which  $\tau(p)$  may exhibit a 'jump' corresponding to the Jth low velocity zone. Thus for the Jth low velocity zone the jump may take place at a slowness value q for which

$$QL(J) \leq q \leq QU(J)$$

It is assumed that

$$QU(J+1) < QL(J)$$

and

$$QU(1) < 1.0$$

The quantities SIGU(J) and SIGL(J) define the uncertainty of the jump in  $\tau(p)$  associated with the Jth low velocity zone. Thus if  $\Delta\tau$  is the jump in  $\tau(p)$  associated with the Jth low velocity zone then,

$$SIGL(J) \leq \Delta\tau \leq SIGU(J)$$

The quantity UMAX(J) is the maximum slowness which can be attained within the Jth low velocity zone.

The values SAM and NDIV define coarse and fine sampling parameters respectively used in the search for upper and lower velocity bounds. SAM is a slowness sampling

used to determine a rough estimate of the location along the p axis for which upper and lower bounds are attained; a more precise estimate is then attained with a search conducted in the region of the rough estimate with a slowness sampling interval of SAM/NDIV.

### Input

The input must be in the following order and format.

1. NU, NL           FORMAT (2I5)
2. PU(I), I = 1, NU    FORMAT (2F15.3)
3. PL(I), I = 1, NL    FORMAT (2F15.3)
4. (AU(I),BU(I),CU(I)), I = 1, MU    FORMAT (3F20.0)
5. (AL(I),BL(I),CL(I)), I = 1, ML    FORMAT (3F20.0)
6. ILU(I), I = 1, MU    FORMAT (10I5)  
     If CU(I) = 0 then ILU(I) = 1, and otherwise  
     ILU(I) = 0.
7. ILL(I), I = 1, ML    FORMAT (10I5)  
     If CL(I) = 0 then ILL(I) = 1, otherwise  
     ILL(I) = 0.
8. SAM            FORMAT (F15.3)
9. NDIV           FORMAT (I5)
10. VSUR           FORMAT (F15.3)  
     VSUR is the actual velocity at the surface of  
     the earth in km/sec.
11. NREGS         FORMAT (I5)  
     NREGS is related to the number of low velocity  
     zones; NLVZS . If QL(NLVZS) > PU(NU) then NREGS =  
     2 NLVZS + 1. If QL(NLVZS) = PU(NU) then NREGS =  
     2 NLVZS.
12. NVELS(K), K = 1, NREGS    FORMAT (10I5)

This quantity gives the number of slowness values for which upper and lower depth bounds are acquired within certain regions of the slowness axis. For this purpose the 1st region of the slowness axis is given by  $QU(1) \leq p \leq 1$ . The Kth region for  $K > 1$  and  $K$  even is given by  $QL(K/2) \leq p \leq QU(K/2)$ . The Kth region for  $K > 1$  and  $K$  odd is given by

$$QU((K+1)/2) \leq p \leq QL((K+1)/2 - 1)$$

If there are no low velocity zones then there is only one region, namely  $PU(NU) \leq p \leq 1$ . Upper and lower depth bounds are calculated for equi-spaced slowness values within the regions.

13. NLVZS           FORMAT (I5)

14. (SIGU(J), SIGL(J), QU(J), QL(J), UMAX(J), MUST(J)), J=1, NLVZS.

FORMAT (5F15.5, I5)

The previously undefined quantity MUST(J) refers to the Jth low velocity zone. If MUST(J) = 1 then a low velocity zone must occur and if MUST(J) = 0 then a low velocity zone may occur. Notice that MUST(J) = 0 if and only if SIGL(J) = 0.0.

### Output

For each low velocity zone the following quantities are given,

(i) the maximum slowness of the zone assuming the maximum thickness and  $\tau(p)$  jumps of SIGL(J) and SIGU(J).

(ii) the maximum thickness of the zone assuming the maximum possible slowness and  $\tau(p)$  jumps of SIGL(J) and SIGU(J).

The above results are given in terms of the 'flat earth' velocity depth bounds associated with the normalized  $\tau(p)$  envelope.

Upper and lower depth bounds for velocity are given in terms of an actual spherical earth; depths are given in km and velocities in km/sec.

#### Operational Procedure

The calculation of the upper depth limit is done in SUBROUTINE UPPLIM which in turn calls SUBROUTINE ULIM. Similarly lower limit calculations are performed by SUBROUTINE LOWLIM which calls SUBROUTINE LLIM. Low velocity zone calculations are done within the main program. At present the program is set up such that it can handle up to 5 low velocity zones, 209 piecewise polynomial descriptions of the upper and lower  $\tau(p)$  bounds, and give 500 estimates of upper and lower depth bounds. If more of the above parameters are required then a simple change of the dimension statements would be necessary.



```

DOUBLE PRECISION SIGU(5), SIGL(5), QU(5), QL(5)
DOUBLE PRECISION HMAX(5), HMIN(5), UMAX(5), UMIN(5)
DOUBLE PRECISION A(500), B(500), ABEST(500), BBEST(500)
DOUBLE PRECISION VA(500), VB(500), SAVE(5,50)
DIMENSION MUST(5), NVELS(11)
DOUBLE PRECISION SKE, TH, THM, SLOW, PD, ARG1, ARG2
DOUBLE PRECISION PU(210), PL(210)
DOUBLE PRECISION AU(210), BU(210), CU(210)
DOUBLE PRECISION AL(210), BL(210), CL(210)
DIMENSION ILU(210), ILL(210)
DOUBLE PRECISION DIV, SAM, VEL, DEP, R, VSUR, FACT
COMMON PL, PU
COMMON AU, BU, CU, AL, BL, CL
COMMON SAM
COMMON NDIV, NL, NU
COMMON ILL, ILU
37  FORMAT(1H, 'THE MINIMUM POSSIBLE SLOWNESS IS'
1, F15.10)
38  FORMAT(1H,
1'MAX SLOWNESS FOR MAX THICKNESS AND MIN SIGL='
1, F15.10)
39  FORMAT(1H,
1'MAX THICKNESS FOR MAX SLOWNESS AND MIN SIGL='
1, F15.5)
41  FORMAT(1H, 'MAX THICKNESS OF LVL', I5, '=', F15.5)
42  FORMAT(1H, 'MAXIMUM THICKNESS FOR MAX SLOWNESS IS'
1, F15.5)
43  FORMAT(1H, 'MAX SLOWNESS FOR MAX THICKNESS=', F15.10)
100  FORMAT(10I5)
101  FORMAT(2F15.3)
102  FORMAT(3F20.0)
2222  FORMAT(1H, 2F10.3, /)
2223  FORMAT(2F10.3)
4343  FORMAT(1H, 'NU, NL, PU, PL, AU, BU, CU, AL, BL, CL, SAM, NDIV
1, VSUR, ILU, ILL, NREGS, NVELS, NLVZS, SIGU, SIGL, QU, QL
1, UMAX, MUST')
4345  FORMAT(1H, 3D20.10)
4346  FORMAT(1H, 5D20.10, I5)
7000  FORMAT(5F15.5, I5)
      R=6371.0D0
      READ(5,100) NU, NL
      READ(5,101) (PU(I), I=1, NU)
      READ(5,101) (PL(I), I=1, NL)
      NU=NU-1
      NL=NL-1
      READ(5,102) ((AU(I), BU(I), CU(I)), I=1, NU)
      READ(5,102) ((AL(I), BL(I), CL(I)), I=1, NL)
      READ(5,100) (ILU(I), I=1, NU)
      READ(5,100) (ILL(I), I=1, NL)
      DO 2228 JV=1, NU
      PU(JV)=PL(JV)
      AU(JV)=AL(JV+1)
2228  CONTINUE
      DO 2229 JV=1, NJ

```

```

ILU(JV)=1
ILL(JV)=1
BU(JV)=0.0
BL(JV)=0.0
CU(JV)=0.0
CL(JV)=0.0
2229 CONTINUE
READ(5,101) SAM
READ(5,100) NDI
READ(5,101) VSUR
READ(5,100) NREGS
READ(5,100) (NVELS(I),I=1,NREGS)
READ(5,100) NLVZS
IF(NLVZS.EQ.0) GO TO 448
READ(5,7000) ((SIGU(I),SIGL(I),QU(I),QL(I),UMAX(I)
1,MUST(I)),I=1,NLVZS)
448 CONTINUE
PD=PL(NL)
WRITE(6,4343)
WRITE(6,100) NU,NL
WRITE(6,4344) (PU(I),I=1,NU)
WRITE(6,4344) (PL(I),I=1,NL)
4344 FORMAT(1H,5D20.9)
WRITE(6,4345) (AU(I),BU(I),CU(I),I=1,MU)
WRITE(6,4345) (AL(I),BL(I),CL(I),I=1,ML)
WRITE(6,4345) SAM
WRITE(6,100) NDI
WRITE(6,4345) VSUR
WRITE(6,100) (ILU(I),I=1,MU)
WRITE(6,100) (ILL(I),I=1,ML)
WRITE(6,100) NREGS,NVELS,NLVZS
WRITE(6,4346) (SIGU(I),SIGL(I),QU(I),QL(I),UMAX(I)
1,MUST(I)),I=1,NLVZS)
IF(NLVZS.EQ.0) QU(1)=PL(NL)
DIV=(1.0D0-QU(1))/(NVELS(1)+1)
MMH=NVELS(1)
DO 10 J=1,MMH
A(J)=1.0D0-DIV*J
B(J)=A(J)
10 CONTINUE
NV=NVELS(1)
IF(NLVZS.EQ.0) GO TO 40
II=0
IF(NREGS.EQ.2) GO TO 30
IJK=NREGS-1
DO 20 I=2,IJK
IF(II.EQ.1) GO TO 60
DIV=(QU(I/2-QL(I/2)))/(NVELS(I-1))
MMN=NVELS(I)
DO 70 J=1,MMN
A(J+NV)=QU(I/2-(J-1)*DIV
70 B(J+NV)=A(J+NV)
A(1+NV)=QU(I/2)
B(1+NV)=QU(I/2)

```

```

A (NVELS (I) + NV) = QL (I/2)
B (NVELS (I) + NV) = QL (I/2)
GO TO 19
60 DIV = (QL ((I-1)/2 - QU ((I-1)/2 + 1)) / (NVELS (I) + 1)
MNN = NVELS (I)
DO 80 J=1, MNN
A (J+NV) = QL ((I-1)/2 - J*DIV)
80 B (J+NV) = A (J+NV)
19 NV = NV + NVELS (I)
II = II - 1
IF (II .EQ. -1) II = 1
20 CONTINUE
30 CONTINUE
IF (II .EQ. 0) GO TO 90
DIV = (QL ((NREGS-1)/2 - PD) / (NVELS (NREGS) + 1)
IXX = NVELS (NREGS)
DO 92 J=1, IXX
A (J+NV) = QL ((NREGS-1)/2 - J*DIV)
92 B (J+NV) = A (J+NV)
NV = NV + NVELS (NREGS)
GO TO 40
90 CONTINUE
DIV = (QU (NREGS/2 - PD) / (NVELS (NREGS)))
IXX = NVELS (NREGS)
DO 93 J=1, IXX
A (J+NV) = QU (NREGS/2 - (J-1) * DIV)
93 B (J+NV) = A (J+NV)
NV = NV + NVELS (NREGS)
40 CONTINUE
CALL LOWLIM (A (J), VA (J), BBEST (J))
CALL UPPLIM (B (J), VB (J), ABEST (J))
2000 CONTINUE
IF (NREGS .EQ. 1) GO TO 4000
NV1 = NVELS (1) + 1
NV2 = NVELS (1) + NVELS (2)
NV1 = 2
NV2 = NVELS (1) + NVELS (2)
DO 800 K=1, NLVZS
DO 79 J=NV1, NV2
79 IF (VA (J) .LT. VA (J-1)) VA (J) = VA (J-1)
JJ = 0
DO 78 J=NV1, NV2
JJ = JJ + 1
78 SAVE (K, JJ) = VA (J)
DO 77 J=NV1, NV2
77 VA (J) = VA (NV1)
IF (II .EQ. 0 .AND. K .EQ. NLVZS) GO TO 800
IF (II .EQ. 1 .AND. K .EQ. NLVZS) GO TO 3000
LV1 = NV2 + 1
LV2 = NV2 + NVELS (2*K+1) + NVELS (2*K+2)
DO 76 J=LV1, LV2
IF (BBEST (J) .GT. QL (K)) GO TO 75
SKE = (A (J) + BBEST (J)) / 2.0D0
DO 55 KV=1, K

```

```

ARG1=DSQRT (UMAX (KV) *UMAX (KV-QL (KV) *QL (KV) )
ARG2=DSQRT (QL (KV) *QL (KV-SKE*SKE)
VA (J) =VA (J- (SIGU (KV) * (1.0D0- (ARG2/ARG1) *DATAN2 (ARG1
1, ARG2) ) ) *2.0D0/(3.14159265358979D0*ARG2)
55 CONTINUE
GO TO 76
75 VA (J) =VA (J-1)
76 CONTINUE
GO TO 799
3000 CONTINUE
LV1=NV2+1
LV2=NV2+NVELS (2*K+1)
DO 74 J=LV1, LV2
IF (BBEST (J) .GT. QL (K) ) GO TO 73
SKE=(A (J) +BBEST (J) )/2.0D0
DO 99 KV=1, K
ARG1=DSQRT (UMAX (KV) *UMAX (KV-QL (KV) *QL (KV) )
ARG2=DSQRT (QL (KV) *QL (KV-SKE*SKE)
VA (J) =VA (J- (SIGU (KV) * (1.0D0- (ARG2/ARG1) *DATAN2 (ARG1, A
1RG2) ) ) *2.0D0/(3.14159265358979D0*ARG2)
99 CONTINUE
GO TO 74
73 VA (J) =VA (J-1)
74 CONTINUE
DO 34 J=LV1, LV2
34 IF (VA (J) .LT. VA (J-1) ) VA (J) =VA (J-1)
GO TO 800
799 CONTINUE
IF (K.EQ. NLVZS) GO TO 800
HV1=HV2+NVELS (2*K+1) +1
HV2=HV2+NVELS (2*K+1) +NVELS (2*K+2)
NV1=NV2+1
NV2=NV2+NVELS (2*K+1) +NVELS (2*K+2)
800 CONTINUE
HV1=NVELS (1) +1
HV2=NVELS (1) +NVELS (2)
NV1=NV2+1
DO 900 K=1, NLVZS
HMAX (K) =0.0D0
JJ=0
DO 5005 J=HV1, HV2
JJ=JJ+1
TH=VB (J-SAVE (K, JJ)
IF (TH.GT. HMAX (K) ) HMAX (K) =TH
5005 CONTINUE
WRITE (6, 41) K, HMAX (K)
THM=SIGU (K) /DSQRT (UMAX (K) *UMAX (K-QU (K) *QU (K) )
SLOW=DSQRT ( (SIGU (K) *SIGU (K) ) / (HMAX (K) *HMAX (K) )
1+QU (K) *QU (K) )
WRITE (6, 42) THM
WRITE (6, 43) SLOW
IF (MUST (K) .EQ. 0) GO TO 54
THM=SIGL (K) /DSQRT (UMAX (K) *UMAX (K-QU (K) *QU (K) )
SLOW=DSQRT ( (SIGL (K) *SIGL (K) ) / (HMAX (K) *HMAX (K) )

```

```

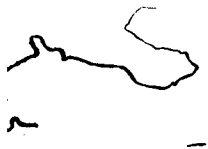
1+QU(K)*QU(K)
10(K)
WRITE(6,39) THH
WRITE(6,38) SLOW
UMIN(K)=DSQRT((SIGL(K)*SIGL(K))/(HMAX(K)*HMAX(K)))
1+QU(K)*QU(K)
WRITE(6,37) UMIN(K)
IF(II.EQ.0.AND.K.EQ.NLVZS) GO TO 900
DO 88 J=NV1,NV
SKE=(ABEST(J)+B(J))/2.0D0
ARG1=DSQRT(UMIN(K)*UMIN(K-QU(K)*QU(K)))
ARG2=DSQRT(QU(K)*QU(K-SKE*SKE))
VB(J)=VB(J-(SIGL(K)*(1.0D0-(ARG2/ARG1)*DATAN2(ARG1,ARG2)
1G2)))*2.0D0/(3.14159265358979*ARG2)
88 CONTINUE
IF(II.EQ.1.AND.K.EQ.NLVZS) GO TO 900
54 CONTINUE
NV1=NV2+NVELS(2*K+1)+1
NV2=NV2+NVELS(2*K+1)+NVELS(2*K+2)
NV1=NV2+1
900 CONTINUE
4000 CONTINUE
DO 3333 J=2,NV
IF(VA(J).LT.VA(J-1)) VA(J)=VA(J-1)
3333 CONTINUE
K=NV
J2=NV-1
DO 3334 J=1,J2
K=K-1
3334 IF(VB(K).GT.VB(K+1)) VB(K)=VB(K+1)
DO 3335 J=1,NV
FACT=DEXP(-VSUR*VA(J)/R)
VEL=VSUR*FACT/A(J)
DEP=R*(1.0D0-FACT)
WRITE(6,2222) VEL,DEP
WRITE(7,2223) VEL,DEP
FACT=DEXP(-VSUR*VB(J)/R)
VEL=VSUR*FACT/B(J)
DEP=R*(1.0D0-FACT)
WRITE(6,2222) VEL,DEP
WRITE(7,2223) VEL,DEP
3335 CONTINUE
CALL EXIT
END

```

```

SUBROUTINE LOWLIN(A,VBEST,BBEST)
DOUBLE PRECISION A,VBEST,BBEST,SAMP,SAM,B1,B2
DOUBLE PRECISION VAL1,VAL2,BOLD,OLD,SDIV,B,VAL
DOUBLE PRECISION PU(210),PL(210)
DOUBLE PRECISION AU(210),BU(210),CU(210)
DOUBLE PRECISION AL(210),BL(210),CL(210)
DIMENSION ILL(210),ILU(210)
COMMON PL,PU
COMMON AU,BU,CU,AL,BL,CL
COMMON SAM
COMMON NDIV,NL,NU
COMMON ILL,ILU
1000 FORMAT(1H,3F15.5)
DO 10 II=2,NL
II7=II
IF(A.GE.PL(II)) GO TO 11
10 CONTINUE
11 NRLA=II7-1
SAMP=SAM
1 B1=A+SAMP
B2=A+2.0D0*SAMP
IF(B2.LE.1.0D0) GO TO 2
3 SAMP=SAMP/2.0D0
GO TO 1
2 CALL LLIN(A,NRLA,B1,VAL1)
CALL LLIN(A,NRLA,B2,VAL2)
IF(VAL2.GT.VAL1) GO TO 4
GO TO 3
4 BOLD=B1
OLD=VAL1
VAL1=VAL2
B1=B2
B2=B2+SAMP
IF(B2.LT.1.0D0) GO TO 5
B2=1.0D0
CALL LLIN(A,NRLA,B2,VAL2)
IF(VAL2.LE.VAL1) GO TO 6
BBEST=B2
VBEST=VAL2
GO TO 7
5 CALL LLIN(A,NRLA,B2,VAL2)
IF(VAL2.GT.VAL1) GO TO 4
6 VBEST=VAL1
BBEST=B1
SDIV=(B2-BOLD)/(NDIV+1)
DO 90 K=1,NDIV
B=BOLD+K*SDIV
CALL LLIN(A,NRLA,B,VAL)
IF(VAL.GT.VBEST) BBEST=B
IF(VAL.GT.VBEST) VBEST=VAL
90 CONTINUE
7 CONTINUE
WRITE(6,1000) A,VBEST,BBEST
RETURN

```



END

```

SUBROUTINE LLIN(A,NRLA,B,V)
DOUBLE PRECISION A,B,V,P1,P2,P3,P4,R1,R2,R3,R4
DOUBLE PRECISION Q1,Q2,Q3,Q4,T3,T4,Z3,Z4,V1,V2
DOUBLE PRECISION SAM
DOUBLE PRECISION PU(210),PL(210)
DOUBLE PRECISION AU(210),BU(210),CU(210)
DOUBLE PRECISION AL(210),BL(210),CL(210)
DIMENSION ILL(210),ILU(210)
COMMON PL,PU
COMMON AU,BU,CU,AL,BL,CL
COMMON SAM
COMMON NDIV,NL,NU
COMMON ILL,ILU
DO 10 I=2,NL
I7=I
IF(B.GT.PL(I)) GO TO 11
10 CONTINUE
11 NRBF=I7-1
DO 20 I=2,NU
I7=I
IF(B.GE.PU(I)) GO TO 21
20 CONTINUE
21 NRBS=I7-1
IR=NRLA-NRBF
P2=B
IF(IR.GT.0) P2=PL(NRLA)
R2=A/P2
Q2=P2*P2-A*A
V1=AL(NRLA)*DARCOS(R2)+A*BL(NRLA)*(DLOG(P2+DSQRT(Q2))
1-DLOG(A))
IF(ILL(NRLA).EQ.1) GO TO 110
V1=V1+A*CL(NRLA)*DSQRT(Q2)
110 CONTINUE
IF(IR.EQ.0) GO TO 40
P1=PL(NRBF+1)
P2=B
R2=A/P2
Q2=P2*P2-A*A
Q1=P1*P1-A*A
R1=A/P1
V1=V1+AL(NRBF)*(DARCOS(R2-DARCOS(R1))+A*BL(NRBF)*DLOG
1((P2+DSQRT(Q2))/(P1+DSQRT(Q1))))
IF(ILL(NRBF).EQ.1) GO TO 111
V1=V1+A*CL(NRBF)*(DSQRT(Q2-DSQRT(Q1)))
111 CONTINUE
IF(IR.EQ.1) GO TO 40
NT=IR-1
DO 50 J=1,NT
P1=PL(NRLA-J+1)
P2=PL(NRLA-J)
R1=A/P1
R2=A/P2
Q1=P1*P1-A*A
Q2=P2*P2-A*A

```



```

V1=V1+AL (NRLA-J) * (DARCOS (R2-DARCOS (R1)) +A*BL (NRLA-J) *
1DLOG ((P2+DSQRT (Q2)) / (P1+DSQRT (Q1)))
IF (ILL (NRLA-J) .EQ. 1) GO TO 112
V1=V1+A*CL (NRLA-J) * (DSQRT (Q2-DSQRT (Q1)))
112 CONTINUE
50 CONTINUE
40 CONTINUE
V2=0.0D0
IF (B.EQ.1.0D0) GO TO 60
P3=B
P4=PU (NRBS)
R4=A/P4
R3=A/P3
Q3=P3*P3-A*A
Q4=P4*P4-A*A
T4=B/P4
Z4=P4*P4-B*B
V2=AU (NRBS) * (DARCOS (R4-DARCOS (R3-DARCOS (T4))) +BU (NRBS
1) * (A* (DLOG (P4+DSQRT (Q4)) -DLOG (P3+DSQRT (Q3))) +B* (DLOG (P
13-DLOG (P4+DSQRT (Z4))))
IF (ILU (NRBS) .EQ. 1) GO TO 113
V2=V2+CU (NRBS) * (A* (DSQRT (Q4-DSQRT (Q3)) -B*DSQRT (Z4))
113 CONTINUE
IF (NRBS.EQ.1) GO TO 60
NT=NRBS-1
DO 70 J=1,NT
P3=PU (NRBS+1-J)
P4=PU (NRBS-J)
R4=A/P4
R3=A/P3
T3=B/P3
T4=B/P4
Q4=P4*P4-A*A
Q3=P3*P3-A*A
Z3=P3*P3-B*B
Z4=P4*P4-B*B
V2=V2+AU (NRBS-J) * (DARCOS (R4-DARCOS (R3-DARCOS (T4)) +DAR
1COS (T3)) +BU (NRBS-J) * (A* (DLOG (P4+DSQRT (Q4)) -DLOG (P3+DSQ
1RT (Q3))) +B* (DLOG (P3+DSQRT (Z3)) -DLOG (P4+DSQRT (Z4))))
IF (ILU (NRBS-J) .EQ. 1) GO TO 114
V2=V2+CU (NRBS-J) * (A* (DSQRT (Q4-DSQRT (Q3)) -B* (DSQRT (Z4)
1-DSQRT (Z3)))
114 CONTINUE
70 CONTINUE
60 CONTINUE
V=(V1+V2)*2.0D0/(B-A)
V=V/3.14159265358979D0
RETURN
END

```

```

SUBROUTINE UPPLIM(B,VBEST,ABEST)
DOUBLE PRECISION B,VBEST,ABEST,SAMP,SAM,A1,A2,PD
DOUBLE PRECISION VAL1,VAL2,AOLD,OLD,SDIV,A,VAL
DOUBLE PRECISION PU(210),PL(210)
DOUBLE PRECISION AU(210),BU(210),CU(210)
DOUBLE PRECISION AL(210),BL(210),CL(210)
DIMENSION ILL(210),ILU(210)
COMMON PL,PU
COMMON AU,BU,CU,AL,BL,CL
COMMON SAM
COMMON NDIV,NL,NU
COMMON ILL,ILU
1000 FORMAT(1H,3F15.5)
PD=PU(NU)
DO 10 II=2,NU
II7=II
IF(B.GT.PU(II)) GO TO 11
10 CONTINUE
11 NRUBF=II7-1
DO 20 JJ=2,NL
JJ7=JJ
IF(B.GE.PL(JJ)) GO TO 21
20 CONTINUE
21 NRUBS=JJ7-1
SAMP=SAM
1 A1=B-SAMP
A2=B-2.0D0*SAMP
IF(A2.GE.PD) GO TO 2
3 SAMP=SAMP/2.0D0
GO TO 1
2 CALL ULM(B,NRUBF,NRUBS,A1,VAL1)
CALL ULM(B,NRUBF,NRUBS,A2,VAL2)
IF(VAL1.GT.VAL2) GO TO 4
GO TO 3
4 AOLD=A1
OLD=VAL1
VAL1=VAL2
A1=A2
A2=A2-SAMP
IF(A2.GT.PD) GO TO 5
A2=PD
CALL ULM(B,NRUBF,NRUBS,A2,VAL2)
IF(VAL2.GE.VAL1) GO TO 6
ABEST=PD
VBEST=VAL2
GO TO 7
5 CALL ULM(B,NRUBF,NRUBS,A2,VAL2)
IF(VAL2.LT.VAL1) GO TO 4
6 VBEST=VAL1
ABEST=A1
SDIV=(AOLD-A2)/(NDIV+1)
DO 90 K=1,NDIV
A=AOLD-K*SDIV
CALL ULM(B,NRUBF,NRUBS,A,VAL)

```

```
90 IF (VAL.LT.VBEST) ABEST=A  
7 IF (VAL.LT.VBEST) VBEST=VAL  
CONTINUE  
CONTINUE  
WRITE (6,1000) B,VBEST,ABEST  
RETURN  
END
```

```

SUBROUTINE ULM(B, NRUBF, NRUBS, A, V)
DOUBLE PRECISION B, A, V, P1, P2, P3, P4, R1, R2, R3, R4
DOUBLE PRECISION Q1, Q2, Q3, Q4, T3, T4, Z3, Z4
DOUBLE PRECISION V1, V2
DOUBLE PRECISION SAM
DOUBLE PRECISION PU(210), PL(210)
DOUBLE PRECISION AU(210), BU(210), CU(210)
DOUBLE PRECISION AL(210), BL(210), CL(210)
DIMENSION ILL(210), ILU(210)
COMMON PL, PU
COMMON AU, BU, CU, AL, BL, CL
COMMON SAM
COMMON NDIV, NL, NU
COMMON ILL, ILU
DO 10 I=2, NU
I7=I
IF(A.GE.PU(I)) GO TO 11
10 CONTINUE
11 NRA=I7-1
IR=NRA-NRUBF
P2=B
IF(IR.GT.0) P2=PU(NRA)
R2=A/P2
Q2=P2*P2-A*A
V1=AU(NRA)*DARCOS(R2)+A*BU(NRA)*(DLOG(P2+DSQRT(Q2))-DL
LOG(A))
IF(ILU(NRA).EQ.1) GO TO 110
V1=V1+A*CU(NRA)*DSQRT(Q2)
110 CONTINUE
IF(IR.EQ.0) GO TO 40
P1=PU(NRUBF+1)
P2=B
R1=A/P1
R2=A/P2
Q2=P2*P2-A*A
Q1=P1*P1-A*A
V1=V1+AU(NRUBF)*(DARCOS(R2-DARCOS(R1))+A*BU(NRUBF)*DL
LOG((P2+DSQRT(Q2))/(P1+DSQRT(Q1))))
IF(ILU(NRUBF).EQ.1) GO TO 111
V1=V1+A*CU(NRUBF)*(DSQRT(Q2-DSQRT(Q1)))
111 CONTINUE
IF(IR.EQ.1) GO TO 40
NT=IR-1
DO 50 J=1, NT
P1=PU(NRA-J+1)
P2=PU(NRA-J)
R1=A/P1
R2=A/P2
Q1=P1*P1-A*A
Q2=P2*P2-A*A
V1=V1+AU(NRA-J)*(DARCOS(R2-DARCOS(R1))+A*BU(NRA-J)*DL
LOG((P2+DSQRT(Q2))/(P1+DSQRT(Q1))))
IF(ILU(NRA-J).EQ.1) GO TO 112
V1=V1+A*CU(NRA-J)*(DSQRT(Q2-DSQRT(Q1)))

```

```

112 CONTINUE
50 CONTINUE
40 CONTINUE
V2=0.000
IF (B.EQ.1.000) GO TO 60
P3=B
P4=PL (NRUBS)
R3=A/P3
R4=A/P4
T4=B/P4
Q3=P3*P3-A*A
Q4=P4*P4-A*A
Z4=P4*P4-B*B
V2=AL (NRUBS) * (DARCOS (R4-DARCOS (R3-DARCOS (T4))) + BL (NRU
1BS) * (A * (DLOG (P4+DSQRT (Q4)) - DLOG (P3+DSQRT (Q3))) + B * (DLOG
1 (P3-DLOG (P4+DSQRT (Z4))))))
IF (ILL (NRUBS).EQ.1) GO TO 113
V2=V2+CL (NRUBS) * (A * (DSQRT (Q4-DSQRT (Q3)) - B * DSQRT (Z4))
113 CONTINUE
IF (NRUBS.EQ.1) GO TO 60
MT=NRUBS-1
DO 70 J=1,MT
P3=PL (NRUBS+1-J)
P4=PL (NRUBS-J)
R4=A/P4
R3=A/P3
T3=B/P3
T4=B/P4
Q3=P3*P3-A*A
Q4=P4*P4-A*A
Z3=P3*P3-B*B
Z4=P4*P4-B*B
V2=V2+AL (NRUBS-J) * (DARCOS (R4-DARCOS (R3-DARCOS (T4)) + DA
1RCOS (T3)) + BL (NRUBS-J) * (A * (DLOG (P4+DSQRT (Q4)) - DLOG (P3+
1DSQRT (Q3))) + B * (DLOG (P3+DSQRT (Z3)) - DLOG (P4+DSQRT (Z4))))))
IF (ILL (NRUBS-J).EQ.1) GO TO 114
V2=V2+CL (NRUBS-J) * (A * (DSQRT (Q4-DSQRT (Q3)) - B * (DSQRT (Z4
1-DSQRT (Z3))))
114 CONTINUE
70 CONTINUE
60 CONTINUE
V=(V1+V2)*2.000/(B-A)
V=V/3.14159265358979D0
RETURN
END

```